

Data-physics Driven Reduced Order Homogenization

Yang Yu

Submitted in partial fulfillment of the
requirements for the degree of
Doctor of Philosophy
under the Executive Committee
of the Graduate School of Arts and Sciences

COLUMBIA UNIVERSITY

2023

© 2023

Yang Yu

All Rights Reserve

Abstract

Data-physics Driven Reduced Order Homogenization

Yang Yu

A hybrid data-physics driven reduced-order homogenization (dpROH) approach aimed at improving the accuracy of the physics-based reduced order homogenization (pROH), but retain its unique characteristics, such as interpretability and extrapolation, has been developed. The salient feature of the dpROH is that the data generated by a high-fidelity model based on the direct numerical simulations with periodic boundary conditions improve markedly the accuracy of the physic-based model reduction. The dpROH consist of the offline and online stages. In the offline stage, dpROH utilized surrogate-based Bayesian Inference to extract crucial information at the representative volume element (RVE) level. With the inferred data, online predictions are performed using a data-enhanced reduced order homogenization. The proposed method combines the benefits of the physics-based reduced order homogenization and data-driven surrogate modeling, striking a balance between accuracy, computational efficiency, and physical interpretability. The dpROH method, as suggested, has the versatility to be utilized across different RVE geometries (including fibrous and woven structures) and various constitutive models, including elasto-plasticity and continuum damage models. Through numerical examples that involve comparisons between different variants of dpROH, pROH, and the reference solution, the method showcases enhanced accuracy and efficiency, validating its effectiveness for a wide range of applications.

A novel pseudo-nonlocal eight-node fully integrated linear hexahedral element, PN3D8, has been developed to accelerate the computational efficiency of multiscale modeling for complex material systems. This element is specifically designed to facilitate finite element analysis of computationally demanding material models, enabling faster and more efficient simulations within the scope of multiscale modeling. The salient feature of the PN3D8 is that it employs reduced integration for stress updates but full integration for element matrices (residual and its consistent tangent stiffness). This is accomplished by defining pseudo-nonlocal and local stress measures. Only the pseudo-nonlocal stress is updated for a given value of mean strain or mean deformation measure for large deformation problems. The local stress is then post processed at full integration points for evaluation of the internal force and consistent tangent stiffness matrices. The resulting tangent stiffness matrix has a symmetric canonical structure with an identical instantaneous constitutive matrix at all quadrature points of an element. For linear elasticity problems, the formulation of the PN3D8 finite element coincides with the classical eight-node fully integrated linear hexahedral element. The procedure is illustrated for small and large deformation two-scale quasistatic problems.

Contents

List of Figures.....	iv
List of Tables	vii
Acknowledgments	viii
Chapter 1 Introduction	1
<i>1.1 Overview</i>	<i>1</i>
<i>1.2 Dissertation outline.....</i>	<i>2</i>
Chapter 2 A Pseudo-Nonlocal Finite Element for Efficient Solution of Computationally Demanding Material Models	4
<i>2.1 Introduction.....</i>	<i>4</i>
<i>2.2 Formulation for Small Deformation Problems</i>	<i>7</i>
<i>2.2.1 Definitions.....</i>	<i>7</i>
<i>2.2.2 The strong form.....</i>	<i>8</i>
<i>2.2.3 The weak form and the finite element discretization</i>	<i>9</i>
<i>2.3 Extension to two-scale material models undergoing large strains.....</i>	<i>11</i>
<i>2.4 Numerical examples</i>	<i>13</i>
<i>2.5 Conclusion</i>	<i>23</i>
Chapter 3: Data-Physics Driven Reduced Order Homogenization	26
<i>3.1 Introduction.....</i>	<i>26</i>
<i>3.2 Identifying shortcomings of physics-based reduced order homogenization.....</i>	<i>31</i>
<i>3.2.1 Review of Physics-Based Reduced Order Homogenization.....</i>	<i>31</i>

3.2.2 Locking of one-partition-per-phase model	34
3.3 Data-physics driven reduced order homogenization (dpROH)	36
3.3.1 The data-driven surrogate-based Bayesian Inverse (BI) framework	37
3.3.2 Revised eigenstrain transformation tensor for the matrix dominated mode.....	40
3.4 Numerical examples.....	43
3.4.1 Setting the bounds on model parameters	44
3.4.2 Fibrous composite.....	45
3.4.3 Woven composite	54
3.4.4 Computational time.....	60
3.5 Conclusion	61
Chapter 4 Data-Physics Driven Reduced Order Homogenization for Continuum Damage	
Mechanics at Multiple Scales	64
4.1 Introduction.....	64
4.2 Methodology	66
4.2.1 Review of the physics driven reduced order homogenization (pROH).....	67
4.2.2 Nonlocal continuum damage mechanics model.....	68
4.3 dpROH framework for continuum damage mechanics.....	70
4.3.1 Reference and training dataset generation.....	70
4.3.2 Surrogate-based Bayesian Inference on softening material behavior.....	71
4.3.3 Framework summary	73
4.4 Numerical Examples	74

4.4.1 Reference solution based on nonlocal DNS model	74
4.4.2 Validation for mixed mode cyclic loading	78
4.4.3 A perforated Plate validation problem	79
4.5 Conclusion	82
Chapter 5 Conclusions.....	83
5.1 Contributions	83
5.2 Future perspective	84
References	86
Appendix A Components of the data-driven surrogate-based Bayesian inverse modeling.	95
A.1 Bayesian Inference	95
A.2 The Gated Recurrent Unit (GRU) based surrogate model.....	98

List of Figures

Figure 2.1. Fibrous unit cell configuration	14
Figure 2.2. A single macroscopic 8-node hexahedral element configuration, its boundary conditions, applied tractions on various element faces, and fibrous unit cell orientation.	16
Figure 2.3. The mean element stress, σ_{yy}^e , versus mean element strain, ϵ_{yy}^e for various element formulations in one-element elastoplastic composite subjected to nonuniform monotonic tensile loading.....	17
Figure 2.4. The mean element stress, σ_{yy}^e , versus mean element strain, ϵ_{yy}^e for various element formulations in one-element elastoplastic composite subjected to nonuniform cyclic tensile loading.....	18
Figure 2.5. Plate with a hole configuration including boundary conditions, applied traction, unit cell orientation, location of the critical element for which the results are postprocessed, distribution of L2 norm of the mean element strain	19
Figure 2.6. Elasto-plastic composite plate with a hole in tension: (a) The L2 norm of the mean element stress, $\ \sigma^e\ _{\Omega_e}$, versus L2 norm of the mean element strain, $\ \epsilon^e\ _{\Omega_e}$ in the critical element as obtained by ROH; (b) The L2 norm of the mean element stress, $\ \sigma^e\ _{\Omega_e}$, versus L2 norm of the mean element strain, $\ \epsilon^e\ _{\Omega_e}$ in the critical element obtained by FOCH; (c) Speedups of various element formulations obtained by ROH; (d) Speedups of various element formulations as obtained by FOCH	20
Figure 2.7. A single macroscopic 8-node hexahedral element configuration, its boundary conditions, direction of nonzero prescribed displacements \bar{u}_{abcd} , and fibrous unit cell orientation	21
Figure 2.8. L_2 norm of the mean second Piola Kirchhoff element stress, $\ S^e\ _{\Omega_e}$, versus L_2 norm of the mean Green-Lagrange element strain, $\ E^e\ _{\Omega_e}$ in one-element hyperelastic composite.....	22
Figure 2.9. Hyperelastic composite plate with a hole in tension: (a) L2 norm of the mean second Piola Kirchhoff element stress, $\ S^e\ _{\Omega_e}$, versus L2 norm of the mean Green-Lagrange element strain, $\ E^e\ _{\Omega_e}$, in the critical element (see Figure 2.5), (b) speedups as obtained by various element formulations	23

Figure 3.1. Inclusion locking in the matrix-dominated mode of deformation and uniform eigenstrain discretization with one partition per phase; fiber is oriented in x_3 direction	35
Figure 3.2. Flowchart of the data-physics driven reduced order homogenization.....	39
Figure 3.3. Representative volume elements and material coordinate system considered in the present study. (a) fibrous composite RVE, (b) woven composite RVE (only tows are shown)...	43
Figure 3.4. Comparison of ROH variants to the reference macroscopic stress-strain solution for (a) fiber dominated tension - 33 (b) transverse tension - 22 (c) in plane shear - 12 (d) transverse shear - 23.....	48
Figure 3.5. The probability density functions of four material parameters $[Y_0^{(1)}, \delta^{(1)}, Y_0^{(2)}, \delta^{(2)}]$ as obtained by Bayesian inference for $\text{dpROH}(\theta^{MCM})$; The trace plots are shown as subplots.	49
Figure 3.6. Mixed mode uniform field cyclic loading (a) Force-displacement relation (b) Transverse shear macroscopic stress-strain relation.	50
Figure 3.7. FOCH solution for the von Mises stress distribution in the quasi-isotropic plate (fibrous composite microstructure) subjected to axial tension. Boundary conditions, laminate orientations, and location of the critical element are shown.....	51
Figure 3.8. FOCH solution for the von Mises stress distribution in the quasi-isotropic plate (fibrous composite microstructure) subjected to in plane shear. Boundary conditions, laminate orientations, and location of the critical element are shown.....	52
Figure 3.9. FOCH solution for the von Mises stress distribution in the quasi-isotropic plate (fibrous composite microstructure) subjected to three-point bending. Boundary conditions, laminate orientations, and location of the critical element are shown.....	53
Figure 3.10. Comparison of ROH variants to the reference macroscopic stress-strain solution for (a) in plane (tow dominated) tension - 11 (b) transverse shear – 23 (c) in plane shear – 12.....	56
Figure 3.11. Mixed mode uniform field cyclic loading - (a) force-displacement relation, (b) macroscopic transverse shear stress-strain relation.	57
Figure 3.12: FOCH solution for the von Mises stress distribution in the quasi-isotropic plate (woven composite microstructure) subjected to in axial tension. Boundary conditions, laminate orientations, and location of the critical element are shown.....	58
Figure 3.13: FOCH solution for the von Mises stress distribution in the quasi-isotropic plate (woven composite microstructure) subjected to in plane shear. Boundary conditions, laminate orientations, and location of the critical element are shown.....	59

Figure 3.14: FOCH solution for the von Mises stress distribution in the quasi-isotropic plate (woven composite microstructure) subjected to three-point bending. Boundary conditions, laminate orientations, and location of the critical element are shown.	60
Figure 4.1. Dataset generation configuration with pROH	71
Figure 4.2 Architecture of the GRU in the dpROH. X_t and Y_t represent inputs and outputs at a pseudo time step t respectively	73
Figure 4.3. Flowchart of the dpROH for multiscale damage modeling.....	74
Figure 4.4. Fibrous RVE and material coordinate system considered in the present study.	77
Figure 4.5. Bayesian Inference results (a) The first row represents the probability density functions of three damage parameters in dpROH v1. The second row refers to the corresponding MCMC trace plots. (b) probability density functions of α and β in dpROH v2.	77
Figure 4.6. (a) mesh independent nonlocal DNS results, (b) transverse tension test mode 22, (c) simple shear mode 12 (d) simple shear 23. Results generated by pROH (red lines). Results generated by dpROH (dashed lines).	78
Figure 4.7 22-component stress-strain of single element subjected to 22-23 mix-mode cyclic tensile loading	79
Figure 4.8. The finite element discretization of the perforated plate with fibrous microstructures. (a) Direct numerical simulation model consisting of 384,989 four-node tetrahedra elements. (b) dpROH model employing 324 eight-noded hexahedra elements for the macroscale domain (c) dpROH model with 616 eight-noded hexahedra elements for the macroscale domain.....	80
Figure 4.9. Force-displacement curves for the DNS, pROH, local dpROH (coarse mesh), nonlocal dpROH (finer mesh).....	81
Figure 4.10. Damage plots for the DNS, local dpROH (coarse mesh), nonlocal dpROH (finer mesh).....	81

List of Tables

Table 2.1: Unit cell material properties for small deformation problems.....	14
Table 3.1. Definition of rescaling parameters.....	43
Table 3.2. Definition of independent rescaling parameters; remaining parameters computed from (3.8).....	43
Table 3.3. Bounds on θ^{MCM} for the fibrous composite RVE	45
Table 3.4. Bounds on rescaling parameters for the fibrous composite RVE.....	45
Table 3.5 Bounds on θ^{MCM} for the woven composite RVE.....	45
Table 3.6. Bounds on rescaling parameters for the woven composite RVE.....	45
Table 3.7. Reference material properties of fibrous composite RVE	46
Table 3.8. Inferred mean values of model parameters ($\bar{\theta}^{ETT}$, $\bar{\theta}^{MCM}$) for various dpROH.....	47
Table 3.9. Critical element error. Fibrous composite. Axial tension test	52
Table 3.10. Critical element error. Fibrous composite. In plane shear test	53
Table 3.11. Critical element error. Fibrous composite. Three-point bending test.....	54
Table 3.12. Reference material properties of the woven composite RVE.....	54
Table 3.13. Inferred mean values of model parameters ($\bar{\theta}^{ETT}$, $\bar{\theta}^{MCM}$) for various dpROH.....	56
Table 3.14. Critical element error. Woven composite. Axial tension test.....	58
Table 3.15. Critical element error. Woven composite. In plane shear test	59
Table 3.16. Critical element error. Fibrous composite. Three-point bending test.....	60
Table 3.17. Computational time for the FOCH and various ROH variants.....	61
Table 4.1. Reference material properties	75
Table 4.2. microstructural damage parameters range for fibrous RVE	75
Table 4.3. Independent terms $P_{ij}^{kl(\beta\alpha)}$ for fibrous RVE.....	76

Acknowledgments

I would like to extend my sincere appreciation to Professor Jacob Fish, my advisor, for his unwavering support, invaluable guidance, and profound wisdom throughout my four-year journey. His unwavering dedication to research has consistently served as a source of inspiration for me. Under his advising, I have not only acquired knowledge but also developed a positive attitude towards life and work.

Furthermore, I would like to express my gratitude to the members of my thesis defense committee: Professors Haim Waisman, Waiching Sun, Marco Giometto, and Marianna Maiaru. Their participation in my Ph.D. defense committee and their invaluable suggestions are deeply appreciated. I am truly grateful for the time they dedicated to reviewing this thesis and attending my defense.

I am also indebted to my friends, including Yang Jiao, Andrea La Spina, Timothy Artz, Andrew Christian Beel, Lechen Li, Zeyu Xiong, and numerous others, for their consistent encouragement and support throughout this arduous journey. Their presence has been instrumental in helping me overcome challenging moments over the years.

Finally, I would like to express my heartfelt gratitude to my mother, Yi Xiang, whose unwavering belief in my studies and decisions has been a constant source of strength. Her encouragement during moments of despair has allowed me to remain focused on my research without any disruptions.

To all the individuals I have encountered along the way, I extend my sincere thanks. I would also like to acknowledge the companionship provided by my beloved cats, Reno and Nano, throughout these years.

Chapter 1

Introduction

1.1 Overview

The multiscale nature of many heterogeneous materials poses significant challenges for computational modeling. Traditional direct numerical simulations often require a high computational cost to resolve all scales accurately, making them infeasible for practical applications. To alleviate the problem, various computational homogenization methods are carried out. The fundamental concept in computational homogenization involves acquiring the numerical representation of constitutive relations for the macroscopic problem by consistently resolving a microstructural problem. Though its implementation is straight forward, the computational cost is still extensive.

Reduced order homogenization modeling provides an alternative approach that aims to overcome the aforementioned challenges by capturing the essential features of the microstructures while significantly reducing the computational complexity. Nevertheless, the potential presence of errors arising from diverse model reduction techniques poses an accuracy challenge, particularly when dealing with more intricate material constitutive models, microstructures, and deformation states. The mathematical assumptions inherent in most model reduction methods unavoidably lead to inaccuracies in the numerical outcomes.

Emerging data-driven multiscale methodologies strive to improve the computational efficiency of online predictions for a Representative Volume Element (RVE) by training a surrogate model. This involves utilizing a training dataset that encompasses material parameters and deformation paths. While these data-driven models exhibit notable computational efficiency during online

predictions, their offline computational time increases significantly when dealing with three-dimensions RVEs featuring path-dependent material models. Additionally, the physical interpretation of the data obtained through interpolation and extrapolation remains ambiguous.

To address the aforementioned concerns, a data enhanced reduced order homogenization approach has been developed. This approach maintains the fundamental physical framework of reduced order models while achieving higher computational accuracy with the aid of limited data.

The utilization of a data-physics driven framework allows for a reduction in computational expenses related to equilibrium problems within the Representative Volume Element (RVE). Furthermore, we have recognized the computational costs associated with the integration stage of macroscopic matrices. In order to address the demand for improved efficiency in this time-intensive stage across various homogenization-like multiscale methods, a pseudo-nonlocal finite element method formulation has been developed. This approach seeks to accelerate the computational process and alleviate the overall computational workload while maintaining accuracy comparable to the conventional full integration scheme.

1.2 Dissertation outline

The dissertation is structured as follows.

Chapter 2 focuses on presenting the formulation of the pseudo-nonlocal finite element method, which is designed to provide an efficient solution for computationally demanding material models. This method is introduced early in the dissertation as it can be utilized in subsequent numerical examples in chapters 3 and 4 to improve computational efficiency.

Chapter 3 provides a comprehensive framework for data-physics driven reduced order homogenization. This framework is applied to fibrous and woven Representative Volume

Elements (RVEs), combined with the classical J2 plasticity material model. The chapter highlights the integration of data-driven approaches with physical principles and demonstrates their effectiveness in capturing the behavior of complex structures.

In Chapter 4, the theory presented in Chapter 3 is extended to include continuum damage mechanics at multiple scales. This chapter explores the application of the data-physics driven reduced order homogenization framework to accurately model and predict the softening behavior of materials at both macroscopic and microscopic scale.

Chapter 5 presents the conclusions and summary of the key findings and contributions of the dissertation. Additionally, it outlines potential future directions for further research.

Chapter 2

A Pseudo-Nonlocal Finite Element for Efficient Solution of Computationally Demanding Material Models

2.1 Introduction

An implicit finite element simulation typically involves three main phases: (i) model development, which primarily focuses on geometry and meshing, (ii) element-level computations (iii) system-level computations. In practice, phase 1 tends to be the most computationally demanding, but for the purposes of this discussion, we will not delve into it as it heavily relies on software, hardware, and human factors.

The distribution of computational costs between the remaining two phases depends on factors such as the nature of the problem, its size, and the computing platform. For inelastic materials undergoing large deformation, the cost of element-level computations is primarily dominated by the stress update (integration) algorithms. However, in certain cases, the cost of system-level computations may be comparable or even higher. However, this scenario often differs when dealing with complex material systems that involve multiple scales, whether computationally resolved or not. In such cases, the cost distribution between element-level computations and system-level computations can vary significantly.

The computational cost associated with the phenomenological simulation of complex materials using multi-surface plasticity models is significant due to the requirement of computing multiple consistency parameters. For example, when modeling wood [1], four surfaces are utilized to represent different failure modes, including tensile fiber failure, mixed-mode radial tension-shear failure, and parallel and transverse compression failures. Similarly, in concrete modeling [2],

multiple surfaces are often employed to capture the inelastic behavior of the material under tension, compression, and shear. Porous materials [3] utilize multi-surfaces to account for diffuse and localized yielding of coalescing bands, while ductile crystals [4] employ them to describe the yield function on various slip systems. In multi-physics applications [5], multi-surfaces are used to characterize the coupled multi-physics response.

The computational cost of explicitly considering multiple scales in simulations is considerably higher compared to phenomenological material models. Depending on the chosen upscaling (homogenization) method, it may even dominate the overall analysis cost. This is particularly true when employing first [6-15] or second-order [16] computational homogenization methods. However, the computational cost can be significantly reduced by utilizing various reduced order models, such as the Voronoi cell method [17, 18], fast Fourier transforms [19, 20], mesh-free reproducing kernel particle method [21], methods of cells [22, 23], wavelet-based reduced order models [24, 25], data-driven based reduced order methods [26-29], reduced order homogenization methods [30-35], and nonuniform transformation field methods [36, 37]. For a recent review of multiscale methods, refer to [38, 39]. For applications of multiscale modeling in biology and engineering, refer to [40]. Furthermore, leading commercial software vendors such as ALTAIR, SIEMENS, SIMULIA, MSC, and NASA Glenn offer multiscale capabilities, as discussed in articles [41-46] published in the special issue of the International Journal for Multiscale Computational Engineering.

To optimize computational efficiency at an elemental level, one effective strategy involves reducing the number of macroscopic integration points. While the traditional use of under-integration aimed to mitigate artificial stiffening resulting from volumetric locking or shear locking, the current focus, given the computational demands of material models, is primarily on

reducing computational costs. A recent advancement in this regard is the adoption of a reduced integration approach [47] in micro-morphic computational homogenization. This approach utilizes a one-point integration quadrilateral element along with a standard hourglass stabilization procedure. For a detailed historical account of the development and implementation of one-point integration and hourglass stabilization, we recommend referring to the [48].

The widely recognized limitation of hourglass control lies in the selection of the control parameter, commonly referred to as either artificial viscosity or stiffness, which has historically been determined through numerical experiments. One way to overcome the reliance on artificial parameters [49] is by combining hourglass control with a selectively reduced integration scheme (SRI). However, implementing SRI does not enhance the computational efficiency of computationally intensive material models, as both full and reduced integration must be applied to different terms within the models. Although it might be theoretically possible to develop a reduced integration approach that dynamically constructs a stabilization matrix by continuously assessing the rank deficiency of the tangent stiffness matrix, as far as our knowledge extends, such an approach does not currently exist for complex material systems characterized by rapidly evolving deformation-dependent anisotropy.

The main focus of this chapter is to propose a comprehensive integration scheme that combines full integration with reduced stress updates. To achieve this, the concept of pseudo-nonlocal and local stress measures is introduced. Specifically, only the pseudo-nonlocal stress is updated based on a given value of the mean strain or mean deformation measure. Subsequently, the local stress is computed at full integration points to determine the internal force and tangent stiffness matrices. The effectiveness of this procedure is demonstrated through examples involving both small and large deformation problems.

The subsequent sections of this chapter are structured as follows. Detailed explanations of the formulation are presented for small deformation problems in Section 2.2 and for large deformation problems in Section 2.3. In Section 2.4, we carry out numerical experiments involving quasistatic small deformation plasticity and large deformation hyper-elasticity. Specifically, we investigate both the first-order computational homogenization and reduced-order homogenization models. The conclusion and future research directions are given in Section 2.5.

Throughout this chapter, a matrix notation [50] is utilized, with bold letters used to represent matrices. Stress and strain measures are represented by $N \times 1$ matrices, except in cases involving natural boundary conditions, where the stress is expressed as a 3×3 matrix. The instantaneous constitutive tensor is denoted by an $N \times N$ matrix. In the case of symmetric stress-strain measures, N is equal to 6, while for non-symmetric pairs, N is equal to 9.

2.2 Formulation for Small Deformation Problems

2.2.1 Definitions

We define a pseudo-nonlocal stress, $\boldsymbol{\sigma}^{PN} = \boldsymbol{\sigma}(\bar{\boldsymbol{\varepsilon}}, \boldsymbol{\alpha})$, as a stress computed from the mean strain, $\bar{\boldsymbol{\varepsilon}}$, defined over a characteristic volume $\bar{\Omega}$ as

$$\bar{\boldsymbol{\varepsilon}} = \frac{1}{|\bar{\Omega}|} \int_{\bar{\Omega}} \boldsymbol{\varepsilon} d\bar{\Omega} \quad (2.1)$$

Given the constitutive equation $\boldsymbol{\sigma}(\bar{\boldsymbol{\varepsilon}}, \boldsymbol{\alpha})$ where $\boldsymbol{\alpha}$ denotes the states variables. The term pseudo-nonlocal stress is selected to reflect the fact that the characteristic volume $\bar{\Omega}$ is chosen to coincide with the finite element domain, i.e., $\bar{\Omega} = \Omega_e$, rather than with a characteristic material length.

Given the definition of the pseudo-nonlocal stress, the local stress $\boldsymbol{\sigma}^L$ is defined as

$$\boldsymbol{\sigma}^L \doteq \boldsymbol{\sigma}^{PN} + \frac{\partial \boldsymbol{\sigma}^{PN}}{\partial \bar{\boldsymbol{\varepsilon}}} (\boldsymbol{\varepsilon} - \bar{\boldsymbol{\varepsilon}}) = \boldsymbol{\sigma}^{PN} + \bar{\mathbf{L}} (\boldsymbol{\varepsilon} - \bar{\boldsymbol{\varepsilon}}) \quad (2.2)$$

where $\bar{\mathbf{L}} = \frac{\partial \boldsymbol{\sigma}^{PN}}{\partial \bar{\boldsymbol{\varepsilon}}}$ denotes the instantaneous constitutive matrix.

Remark 1: In the case of an inelastic material, the local stress obtained via eq. (2.2) approximates the classical local formulation. For linear elasticity, $\bar{\mathbf{L}} = \mathbf{L}$, $\boldsymbol{\sigma}^{NL} = \mathbf{L}\bar{\boldsymbol{\varepsilon}}$, yielding $\boldsymbol{\sigma}^L = \mathbf{L}\boldsymbol{\varepsilon}$. This means that the proposed formulation herein coincides with the classical local formulation for linear elasticity. Moreover, since the full integration Gauss quadrature is employed (see Section 2.2.3) the resulting finite element formulation for linear elasticity coincides with the classical full integration elements.

2.2.2 The strong form

The governing quasistatic equations consist of equilibrium, kinematic and constitutive equations together with appropriate boundary conditions:

$$\begin{aligned} \text{Equilibrium:} \quad & \nabla_s^T \boldsymbol{\sigma}^L + \mathbf{b} = \mathbf{0} \text{ on } \Omega \\ \text{Constitutive eq.:} \quad & \boldsymbol{\sigma}^{PN} = \boldsymbol{\sigma}(\bar{\boldsymbol{\varepsilon}}, \boldsymbol{\alpha}) \text{ on } \Omega \\ \text{Kinematic eq.:} \quad & \boldsymbol{\varepsilon} = \nabla_s \mathbf{u} \text{ on } \Omega \\ \text{Natural BC:} \quad & \underline{\boldsymbol{\sigma}}^L \mathbf{n} = \bar{\mathbf{t}} \text{ on } \partial\Omega_t \\ \text{Essential BC:} \quad & \mathbf{u} = \bar{\mathbf{u}} \text{ on } \partial\Omega_u \end{aligned} \quad (2.3)$$

where Ω , $\partial\Omega_t$, $\partial\Omega_u$ denote the problem domain and its natural and essential boundaries, respectively, such that $\partial\Omega_t \cup \partial\Omega_u = \partial\Omega$ and $\partial\Omega_t \cap \partial\Omega_u = \emptyset$; \mathbf{u} denotes displacements; ∇_s symmetric gradient; and $\bar{\mathbf{u}}$, $\bar{\mathbf{t}}$ prescribed displacements and tractions, respectively; superscript T denotes the transpose of a matrix. The underbar appearing in $\underline{\boldsymbol{\sigma}}^L$ denotes the 3×3 matrix of stress.

***Remark 2:** The local stress $\boldsymbol{\sigma}^L$ may not satisfy consistency conditions, such as stress being on the yield surface in the plastic process. On the other hand, given the mean strain, $\bar{\boldsymbol{\varepsilon}}$, and the constitutive equation, $\boldsymbol{\sigma}(\bar{\boldsymbol{\varepsilon}}, \boldsymbol{\alpha})$, the pseudo-nonlocal stress, $\boldsymbol{\sigma}^{PN}$, and its consistent tangent, $\bar{\mathbf{L}}$, can be calculated using standard stress update (integration) procedures. For two-scale material models undergoing small deformations, $\boldsymbol{\sigma}^{PN}$ and $\bar{\mathbf{L}}$, can be computed using first order homogenization or reduced order methods.*

2.2.3 The weak form and the finite element discretization

Herein, we consider lower-order iso-parametric finite elements, such as four-node quadrilateral elements and eight-node hexahedral elements. The discretized test \boldsymbol{w} and trial \boldsymbol{u} functions are given by:

$$\begin{aligned} \boldsymbol{u} &= \boldsymbol{N} \boldsymbol{d} \\ \boldsymbol{w} &= \boldsymbol{N} \boldsymbol{c} \end{aligned} \tag{2.4}$$

where \boldsymbol{N} denotes the global shape functions; \boldsymbol{d} and \boldsymbol{c} are global nodal values of trial and test functions, respectively. The discretized strains are given by:

$$\begin{aligned} \boldsymbol{\varepsilon} &= \boldsymbol{B} \boldsymbol{d} \\ \bar{\boldsymbol{\varepsilon}} &= \bar{\boldsymbol{B}} \boldsymbol{d} \end{aligned} \tag{2.5}$$

where $\boldsymbol{B} = \nabla_s \boldsymbol{N}$ and

$$\bar{\boldsymbol{B}} = \frac{1}{|\Omega_e|} \int_{\Omega_e} \boldsymbol{B} d\Omega \quad \forall e \tag{2.6}$$

In some cases, the mean strain can be approximated (or even coincide) with the strain at an element centroid, \boldsymbol{x}_0 , in which case

$$\boldsymbol{B}_0 \equiv \boldsymbol{B}(\boldsymbol{x}_0) \tag{2.7}$$

would replace $\bar{\boldsymbol{B}}$ in eq. (2.5).

Writing the weak form for (2.3) and subsequently discretizing it yields the residual equation:

$$\mathbf{r} = \mathbf{f}^{int}(\mathbf{d}) - \mathbf{f}^{ext} = \mathbf{0} \quad (2.8)$$

where the internal and external force matrices are given by

$$\begin{aligned} \mathbf{f}^{int}(\mathbf{d}) &= \int_{\Omega} \mathbf{B}^T \boldsymbol{\sigma}^L d\Omega = \int_{\Omega} \mathbf{B}^T \left(\boldsymbol{\sigma}^{PN} + \bar{\mathbf{L}}(\boldsymbol{\varepsilon} - \bar{\boldsymbol{\varepsilon}}) \right) d\Omega \\ \mathbf{f}^{ext} &= \int_{\Omega} \mathbf{N}^T \mathbf{b} d\Omega + \int_{\partial\Omega_t} \mathbf{N}^T \bar{\mathbf{t}} d\Gamma \end{aligned} \quad (2.9)$$

The tangent stiffness matrix is obtained by consistent linearization of the internal force:

$$\mathbf{K}^{tan} = \frac{\partial \mathbf{f}^{int}}{\partial \mathbf{d}} = \int_{\Omega} \mathbf{B}^T \left(\frac{\partial \boldsymbol{\sigma}^{PN}}{\partial \bar{\boldsymbol{\varepsilon}}} \frac{\partial \bar{\boldsymbol{\varepsilon}}}{\partial \mathbf{d}} + \bar{\mathbf{L}} \left(\frac{\partial \boldsymbol{\varepsilon}}{\partial \mathbf{d}} - \frac{\partial \bar{\boldsymbol{\varepsilon}}}{\partial \mathbf{d}} \right) \right) d\Omega = \int_{\Omega} \mathbf{B}^T \bar{\mathbf{L}} \mathbf{B} d\Omega \quad (2.10)$$

The stiffness matrix and the internal force are evaluated using full integration Gauss quadrature. Hereafter, we will refer to the eight-node fully integrated (2x2x2 integration points) linear hexahedral element based on the above formulation as PN3D8 where PN stands for Pseudo-Nonlocal.

***Remark 3:** For each finite element, given the mean element strain $\bar{\boldsymbol{\varepsilon}}$, a single stress update is carried out to calculate $\boldsymbol{\sigma}^{PN}$. The local stress $\boldsymbol{\sigma}^L$ is then calculated at full quadrature points using eq. (2.2) followed by the evaluation of the internal force matrix in eq. (2.9a) using standard Gauss quadrature. Likewise, for each finite element, the instantaneous constitutive matrix $\bar{\mathbf{L}}$ is calculated only once, and then reused it all full Gauss quadrature points for the evaluation of the tangent stiffness matrix (2.10). In fact, the resulting symmetric canonical structure of the tangent stiffness matrix in eq. (2.10) was one of the prime motivations for the definition of local stress in eq. (2.2).*

2.3 Extension to two-scale material models undergoing large strains

For two-scale materials undergoing large strains, it is convenient to select the first Piola-Kirchhoff stress \mathbf{P} and its conjugate deformation measure, deformation gradient, \mathbf{F} . In addition to conjugacy, the coarse-scale quantities can be directly computed by averaging the corresponding fine-scale quantities, \mathbf{P}^f and \mathbf{F}^f , over the undeformed unit cell domain Θ

$$\begin{aligned}\mathbf{P} &= \frac{1}{|\Theta|} \int_{\Theta} \mathbf{P}^f d\Theta \\ \mathbf{F} &= \frac{1}{|\Theta|} \int_{\Theta} \mathbf{F}^f d\Theta\end{aligned}\tag{2.11}$$

Similarly to Eqs. (2.1), (2.2), we define the pseudo-nonlocal first Piola Kirchhoff stress, $\mathbf{P}^{PN} = \mathbf{P}(\bar{\mathbf{F}}, \boldsymbol{\alpha})$, as the stress computed from the mean deformation gradient $\bar{\mathbf{F}}$ defined over an element domain Ω_e

$$\bar{\mathbf{F}} = \frac{1}{|\Omega_e|} \int_{\Omega_e} \mathbf{F} d\Omega\tag{2.12}$$

The local first Piola Kirchhoff stress \mathbf{P}^L is then defined as:

$$\mathbf{P}^L \doteq \mathbf{P}^{PN} + \frac{\partial \mathbf{P}^{PN}}{\partial \bar{\mathbf{F}}} (\mathbf{F} - \bar{\mathbf{F}}) = \mathbf{P}^{PN} + \bar{\mathbf{L}}_{p-F} (\mathbf{F} - \bar{\mathbf{F}})\tag{2.13}$$

For two-scale material models, the instantaneous constitutive matrix $\bar{\mathbf{L}}_{p-F}$ can be computed by either forward difference approximation [34, 51] or by condensation of the constrained degrees-of-freedom corresponding to coarse-scale deformation of the representative volume element (RVE) [16, 52].

The quasistatic governing equations defined on the undeformed configuration Ω_X are given by

$$\begin{aligned}
\text{Equilibrium:} \quad & \nabla_X \mathbf{P}^L + \mathbf{b}_X = \mathbf{0} \text{ on } \Omega_X \\
\text{Constitutive eq.:} \quad & \mathbf{P}^{PN} = \mathbf{P}(\bar{\mathbf{F}}, \boldsymbol{\alpha}) \text{ on } \Omega_X \\
\text{Kinematic eq.:} \quad & \mathbf{F} = \mathbf{I} + \nabla_X \mathbf{u} \text{ on } \Omega_X \\
\text{Natural BC:} \quad & \underline{\mathbf{P}}^L \mathbf{n}_X = \bar{\mathbf{t}}_X \text{ on } \partial\Omega_{Xt} \\
\text{Essential BC:} \quad & \mathbf{u} = \bar{\mathbf{u}} \text{ on } \partial\Omega_{Xu}
\end{aligned} \tag{2.14}$$

where subscript X denotes the undeformed configuration. Equation (2.14) together with (2.12), and (2.13) complete the definition of the strong form. The underbar appearing in $\underline{\mathbf{P}}^L$ denotes the 3×3 matrix.

Considering iso-parametric discretization (2.4), the deformation gradient and the gradient of the test function is given by

$$\begin{aligned}
\mathbf{F} - \mathbf{I} &= \nabla_X \mathbf{N} \mathbf{d} \\
\bar{\mathbf{F}} - \mathbf{I} &= \overline{\nabla_X \mathbf{N}} \mathbf{d} \\
\nabla_X \mathbf{w} &= \nabla_X \mathbf{N} \mathbf{c}
\end{aligned} \tag{2.15}$$

where

$$\overline{\nabla_X \mathbf{N}} = \frac{1}{|\Omega_{Xe}|} \int_{\Omega_{Xe}} \nabla_X \mathbf{N} d\Omega_X \quad \forall e \tag{2.16}$$

The residual equation (2.8) with the following internal and external force vectors based on the PN3D8 element formulation are given by

$$\begin{aligned}
\mathbf{f}^{int}(\mathbf{d}) &= \int_{\Omega_X} \nabla_X \mathbf{N}^T \mathbf{P}^L d\Omega = \int_{\Omega_X} \nabla_X \mathbf{N}^T \left(\mathbf{P}^{PN} + \bar{\mathbf{L}}_{P-F} (\mathbf{F} - \bar{\mathbf{F}}) \right) d\Omega \\
\mathbf{f}^{ext} &= \int_{\Omega_X} \mathbf{N}^T \mathbf{b}_X d\Omega + \int_{\partial\Omega_{Xt}} \mathbf{N}^T \bar{\mathbf{t}}_X d\Gamma
\end{aligned} \tag{2.17}$$

The resulting tangent stiffness matrix is given by

$$\mathbf{K}^{tan} = \frac{\partial \mathbf{f}^{int}}{\partial \mathbf{d}} = \int_{\Omega_X} \nabla_X \mathbf{N}^T \left(\frac{\partial \mathbf{P}^{PN}}{\partial \bar{\mathbf{F}}} \frac{\partial \bar{\mathbf{F}}}{\partial \mathbf{d}} + \bar{\mathbf{L}}_{P-F} \left(\frac{\partial \mathbf{F}}{\partial \mathbf{d}} - \frac{\partial \bar{\mathbf{F}}}{\partial \mathbf{d}} \right) \right) d\Omega = \int_{\Omega_X} \nabla_X \mathbf{N}^T \bar{\mathbf{L}}_{P-F} \nabla_X \mathbf{N} d\Omega \tag{2.18}$$

Remark 4: The structure of the discrete equations (2.17) and (2.18) expressed in terms of the conjugate $\mathbf{P} - \mathbf{F}$ pair is very similar to the corresponding small deformation problem. However, $\bar{\mathbf{L}}_{\mathbf{P}-\mathbf{F}}$ is 9×9 matrix requiring nine perturbations of the deformation gradient as opposed to just six in the case of symmetric stress and deformation measures. For details of how to reformulate the problem (2.14) in terms of symmetric Lagrangian (Second Piola Kirchhoff stress - right Cauchy-Green deformation) and Eulerian (Kirchhoff stress - right Cauchy-Green deformation) measures we refer to Miehe [47].

2.4 Numerical examples

In this section, our focus is on evaluating the performance of the PN3D8 element in handling small and large deformation two-scale problems. Specifically, we will examine two variants of the PN3D8 element: one based on the mean strain (denoted as PN3D8) and the other based on the mid-point strain (denoted as PN3D8v). To assess their effectiveness, we will compare their performance against two other elements: the C3D8, an 8-node fully integrated linear hexahedral element with $2 \times 2 \times 2$ integration points, and the C3D8R, an 8-node linear hexahedral element with 1-point integration and hourglass control.

It's important to note that the main objective is not to focus on an element's ability to alleviate locking, but rather to investigate whether the accuracy of the PN3D8 variants is maintained when compared to the fully integrated C3D8 element, while also considering the computational cost in comparison to the 1-point integrated element, C3D8R. The scope of our study will primarily revolve around examining the computational performance of PN3D8 and PN3D8v within the context of two-scale materials, utilizing both the first-order computational homogenization (FOCH) and reduced-order homogenization (ROH) approaches. However, it is important to clarify

that this study does not delve into the potential benefits of reducing mesh size dependence in failure simulations due to the nonlocal character of the PN3D8 element. This aspect will not be explored in the present investigation.

For all numerical examples considered herein, the geometry of the unit cell is depicted in Figure 2.1.

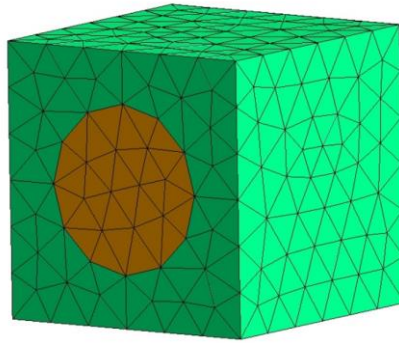


Figure 2.1. Fibrous unit cell configuration

This unit cell consisting of two phases is discretized with 1558 eight-node hexahedral elements. For small deformation problems, the “matrix” phase is modeled using J2 plasticity whereas the “inclusion” or “fiber” phase remains linear elastic. The material constants are summarized in Table 2.1.

Table 2.1. Unit cell material properties for small deformation problems

	Matrix (J2 plasticity)	Inclusion or fiber (elasticity)
Young’s Modulus	3800 Mpa	252000 Mpa
Poisson’s ratio	0.32	0.02
Yield strength	28.0 Mpa	N/A
Exponent for the evolution law	1.0	N/A
Linear term for hardening law	38.0 Mpa	N/A

For large deformation problems, we consider a compressible Neo-Hookean material model for both phases defined as

$$\boldsymbol{\tau} = G \operatorname{dev}(\mathbf{B}_{iso}) + K \ln(J) \mathbf{I} \quad (2.19)$$

where $\operatorname{dev}(\)$ denotes the deviatoric part; \mathbf{B}_{iso} denotes the isochoric left Cauchy-Green (Finger) deformation matrix. G is the shear modulus and K is the bulk modulus. The shear moduli are 1.0 Mpa and 1.5 Mpa for the two phases, respectively, and the corresponding bulk moduli are 20 Mpa and 30 Mpa.

We will conduct a comparative analysis of various element formulations by examining the mean values and their respective L2 norms of stress and strain components. Let's denote the matrix of stresses or strains as \mathbf{s} , with dimensions $N \times 1$. The L2 norm of the mean element value over the element domain Ω_e can be defined as follows:

$$\|\mathbf{s}\|_{\Omega_e} = \frac{1}{|\Omega_e|} \int_{\Omega_e} \sqrt{\mathbf{s}^T \mathbf{s}} \, d\Omega \quad (2.20)$$

For comparison of individual components, say s_i , the mean element value is defined as

$$s_i^e = \frac{1}{|\Omega_e|} \int_{\Omega_e} s_i \, d\Omega \quad (2.21)$$

For simulations involving more than one element we will compare speedups of various element formulations in comparison to C3D8. let denote the C3D8R, PN3D8, and PN3D8v elements.

We define the speedup in the quantity of interest f denoted spd_{\square}^f as

$$spd_{\square}^f = \frac{CPU_{C3D8}^f}{CPU_{\square}^f} \quad (2.22)$$

where CPU_{\square}^f and CPU_{C3D8}^f denote the CPU time of corresponding element formulations in the quantity of interest f .

Figure 2.2 provides an illustration of the 8-node hexahedral element's configuration, encompassing its boundary conditions, tractions applied to various element faces, as well as the orientation of the unit cell. The surfaces $efgh$ and $adbc$ are fixed in the x -direction, while the surface $aehb$ is fixed in the y -direction, and the surface $hgcb$ is fixed in the z -direction. Nonzero tractions denoted \bar{t}_{degf} , \bar{t}_{abcd} , \bar{t}_{adfe} are applied in the y -direction, which is orthogonal to the fiber axis. The prescribed values for these tractions are 70 Mpa, 50 Mpa, and 30 Mpa, respectively.

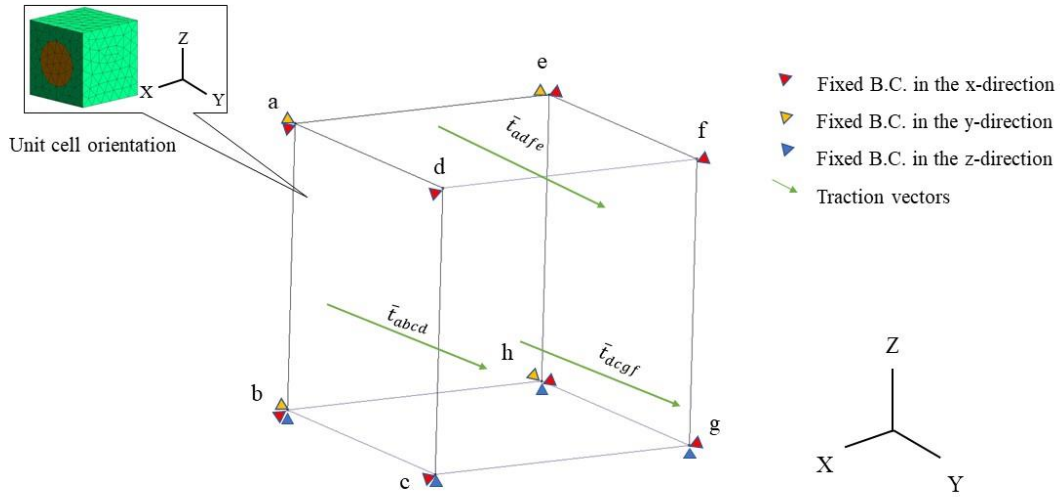


Figure 2.2. A single macroscopic 8-node hexahedral element configuration, its boundary conditions, applied tractions on various element faces, and fibrous unit cell orientation.

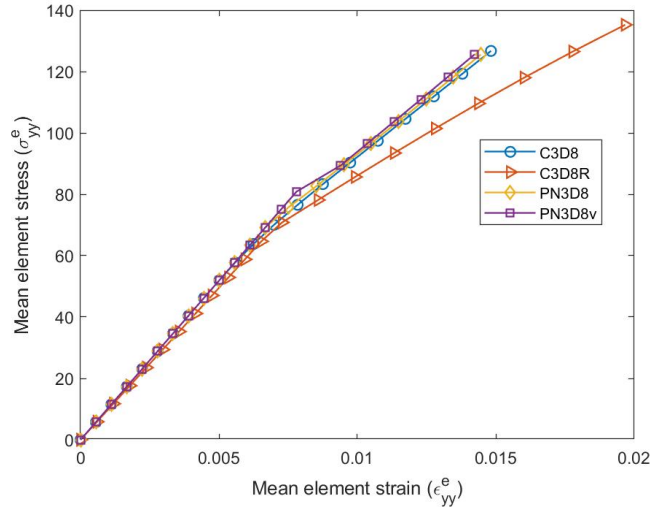


Figure 2.3. The mean element stress, σ_{yy}^e , versus mean element strain, ϵ_{yy}^e for various element formulations in one-element elastoplastic composite subjected to nonuniform monotonic tensile loading

The problem is analyzed using reduced order homogenization (ROH) approach. The mean element stress, σ_{yy}^e , versus mean element strain, ϵ_{yy}^e for various element formulations in one-element elastoplastic composite subjected to nonuniform monotonic tensile loading are depicted in Figure 2.3. Due to nonuniformity of applied tractions the C3D8R gives rise to a bit softer response than the C3D8 especially in the post yield regime. In the pre-yield regime, the responses PN3D8 and PN3D8v elements coincide as eluded in the Remark 1.

Next, we consider a loading-unloading test on the same one-element configuration depicted in Figure 2.2. The nonzero tractions \bar{t}_{dcgf} , \bar{t}_{abcd} , \bar{t}_{adfe} in y direction are monotonically increased to 100 Mpa, 50 Mpa, and 50 Mpa, respectively, and subsequently unloaded to 0. The mean element stress, σ_{yy}^e , versus mean element strain, ϵ_{yy}^e for various element formulations in one-element elastoplastic composite subjected to nonuniform cyclic tensile loading are shown in Figure 2.4.

In the loading and unloading test, the C3D8R element still exhibits a softer behavior compared to all variants of the pseudo-nonlocal finite element. This observation suggests that the pseudo-nonlocal finite element methods demonstrate improved performance in accurately capturing the mechanical response during the loading and unloading process. The enhanced performance can be attributed to the incorporation of nonlocal effects, which effectively address issues related to element softening. This finding further supports the suitability and effectiveness of the pseudo-nonlocal finite element methods for simulating and analyzing material behavior under various loading conditions.

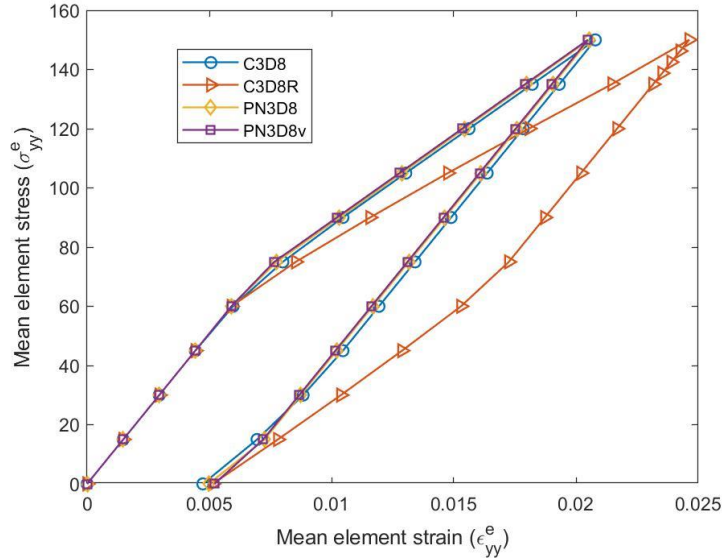


Figure 2.4. The mean element stress, σ_{yy}^e , versus mean element strain, ϵ_{yy}^e for various element formulations in one-element elastoplastic composite subjected to nonuniform cyclic tensile loading

We will now examine a plate featuring a hole that is subjected to tensile loading, as illustrated in Figure 2.5. Considering the symmetrical nature of the plate, only one-eighth of it is modeled. The plate's dimensions are specified as follows: thickness = 0.136 mm, width = 24 mm, length = 48 mm, and the hole has a radius of 4 mm. The boundary conditions are depicted in Figure 2.5 for

reference. A tensile traction of 18.38 MPa is applied, oriented perpendicular to the fiber axis. The critical element, whose results are subjected to further analysis, is also indicated in Figure 2.5. The plate undergoes analysis utilizing both the FOCH and ROH models.

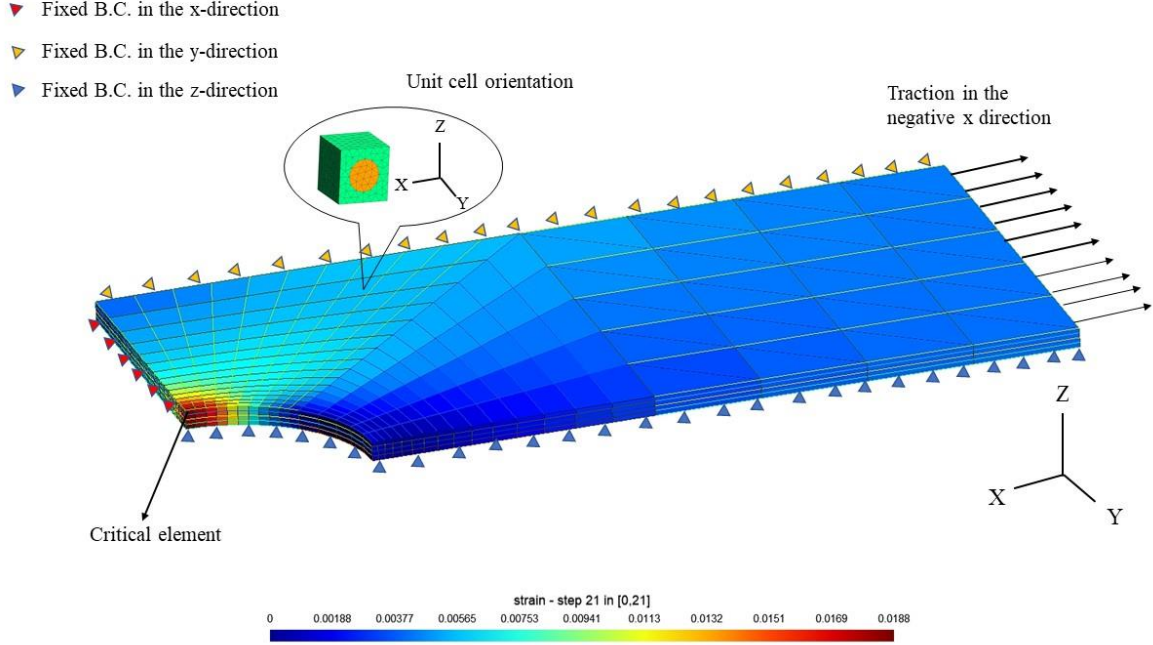


Figure 2.5. Plate with a hole configuration including boundary conditions, applied traction, unit cell orientation, location of the critical element for which the results are postprocessed, distribution of L2 norm of the mean element strain

Figures 2.6 (a) and (b) depict the L2 norm of the mean element stress, $\|\sigma^e\|_{\Omega_e}$, versus L2 norm of the mean element strain, $\|\epsilon^e\|_{\Omega_e}$ in the critical element (depicted in Figure 2.5) as obtained by ROH and FOCH, respectively. Note that the results obtained by FOCH and ROH are not identical since the reduced order model was not calibrated. Figures 2.6 (c) and (d) depict the speedups of various element formulations as obtained by ROH and FOCH, respectively. In this numerical example, the critical element experiences a relatively uniform field, resulting in nearly identical stress-strain plots at the critical element across different methods. However, despite the similar stress-strain

behavior, we can still observe the computational efficiency advantage of the PNC3D8 and PNC3D8v variants in this particular case.

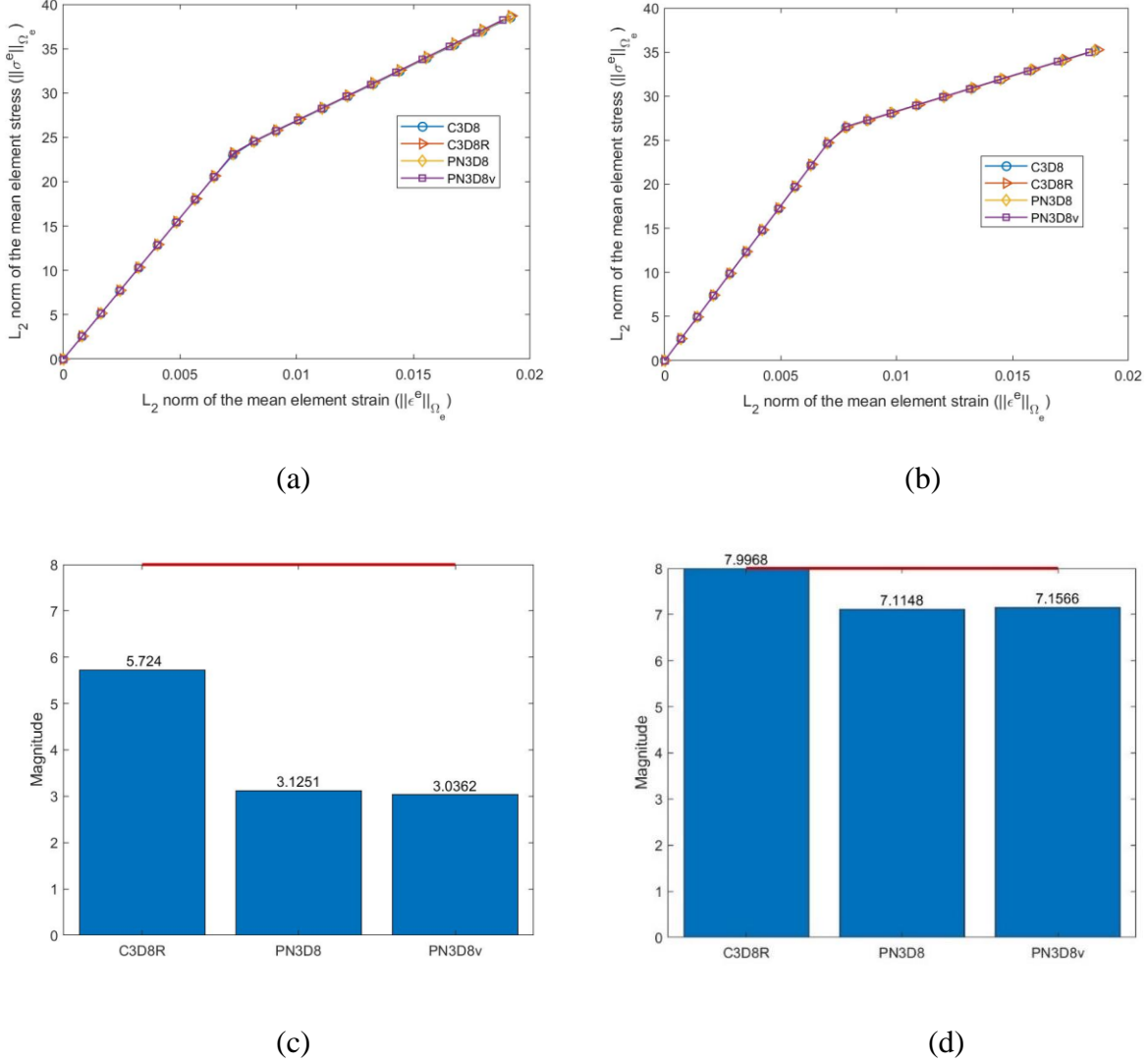


Figure 2.6. Elasto-plastic composite plate with a hole in tension: (a) The L2 norm of the mean element stress, $\|\sigma^e\|_{\Omega_e}$, versus L2 norm of the mean element strain, $\|\epsilon^e\|_{\Omega_e}$ in the critical element as obtained by ROH; (b) The L2 norm of the mean element stress, $\|\sigma^e\|_{\Omega_e}$, versus L2 norm of the mean element strain, $\|\epsilon^e\|_{\Omega_e}$ in the critical element obtained by FOCH; (c) Speedups of various element formulations obtained by ROH; (d) Speedups of various element formulations as obtained by FOCH

We are now addressing a large deformation two-scale problem, where both phases involved adhere to Neo-Hookean material behavior. In Figure 2.7, there is an illustration of a single macroscopic 8-node hexahedral element alongside the orientations of fibrous unit cells. The prescribed displacements are uniform in the z-direction on the surface abcd. Surfaces efgh and aehb are fixed in the x- and y-directions, respectively. Additionally, nodes h and g are constrained in the z-direction.

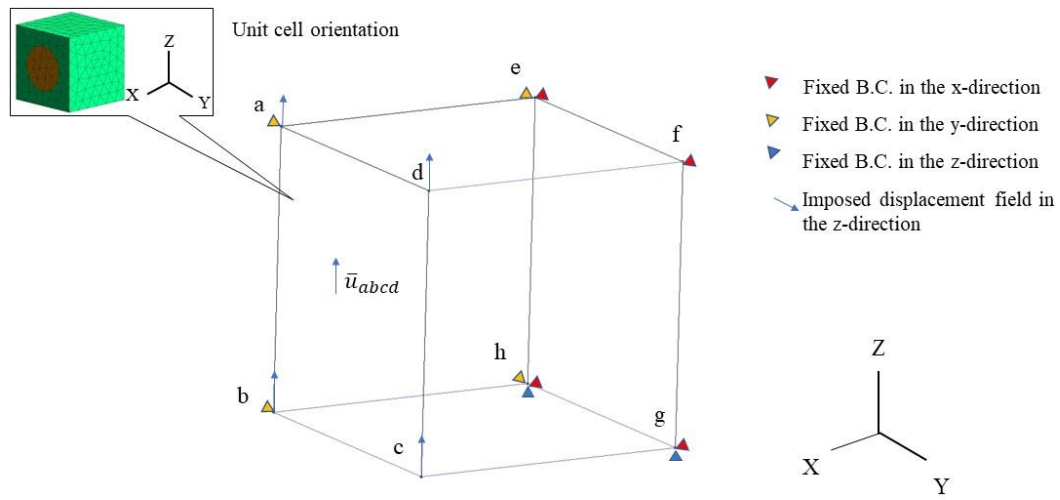


Figure 2.7. A single macroscopic 8-node hexahedral element configuration, its boundary conditions, direction of nonzero prescribed displacements \bar{u}_{abcd} , and fibrous unit cell orientation

It can be observed that the C3D8R element exhibits relatively softer behavior compared to the C3D8 element. On the other hand, the PN3D8 element maintains an acceptable level of accuracy.

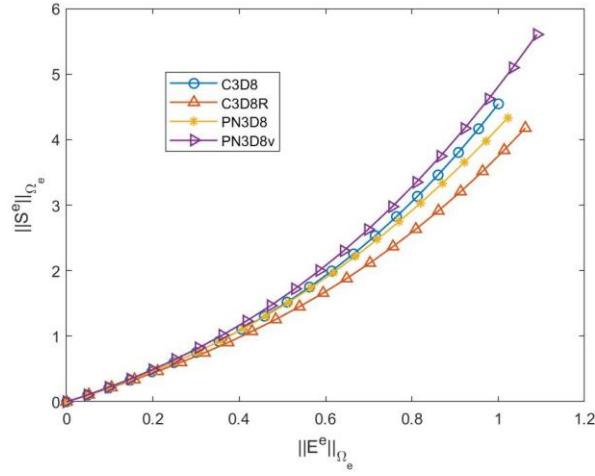


Figure 2.8. L_2 norm of the mean second Piola Kirchhoff element stress, $\|S^e\|_{\Omega_e}$, versus L_2 norm of the mean Green-Lagrange element strain, $\|E^e\|_{\Omega_e}$ in one-element hyper-elastic composite.

In our final study, we investigate a plate with a hole problem, as shown in Figure 2.5. Both phases involved in the problem follow Neo-Hookean material behavior. We impose a prescribed displacement \bar{u}_x in the negative x-direction, while keeping the remaining boundary conditions and the location of the critical element unchanged.

In Figure 2.9(a), we present the L_2 norm of the mean second Piola Kirchhoff element stress, denoted as $\|S^e\|_{\Omega_e}$, plotted against the L_2 norm of the mean Green-Lagrange element strain, denoted as $\|E^e\|_{\Omega_e}$. These results are obtained using the FOCH model. Figure 2.9(b) illustrates the speedups achieved by various element formulations used in the analysis. Despite the small discrepancies observed among different methods in this particular case, we can still observe the advantages of PN3D8 and PN3D8v over C3D8 in this numerical example. These advantages could include improved accuracy, enhanced stability, or better convergence properties. The specific benefits may vary depending on the particular characteristics of the problem being analyzed.

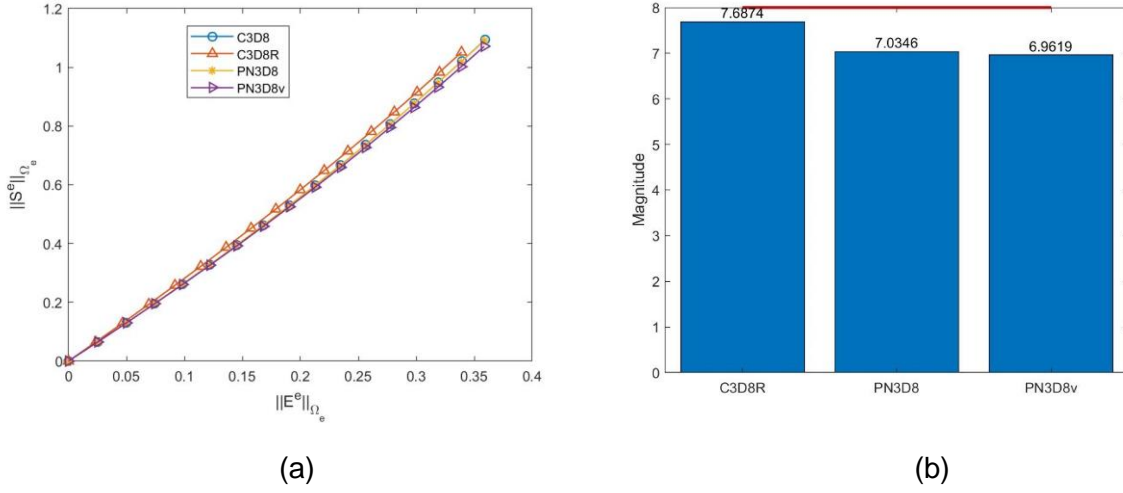


Figure 2.9. Hyperelastic composite plate with a hole in tension: (a) L2 norm of the mean second Piola Kirchhoff element stress, $\|S^e\|_{\Omega_e}$, versus L2 norm of the mean Green-Lagrange element strain, $\|E^e\|_{\Omega_e}$, in the critical element (see Figure 2.5), (b) speedups as obtained by various element formulations

2.5 Conclusion

The main objective of this chapter was to develop an efficient finite element formulation suitable for computationally demanding material models commonly encountered in mesoscale and multiscale applications. To achieve this objective, we introduced a new element called the 8-node fully integrated linear hexahedral element (PN3D8). This element utilizes a $2 \times 2 \times 2$ integration scheme, ensuring computational efficiency while still maintaining a full rank of element matrices. A notable feature of the PN3D8 element is its use of one-point integration for stress updates, which allows for efficient computations without sacrificing the accuracy of the results. The resulting consistent tangent stiffness matrix exhibits a symmetric canonical structure, with the same instantaneous constitutive matrix appearing at all quadrature points within an element. For linear elastic materials, the formulation of the PN3D8 element coincides with that of the classical 8-node fully integrated linear hexahedral element (C3D8). This allows for a seamless transition when

working with linear elastic materials. The advantages and benefits of the PN3D8 element were demonstrated through the illustration of its application in quasistatic problems. By utilizing this element, computationally demanding simulations can be performed efficiently while maintaining accuracy, making it a valuable tool for mesoscale and multiscale applications.

The PN3D8 element was found to exhibit accuracy very close to that of the standard C3D8 element, both of which were stiffer compared to the C3D8R element with one-point integration and hourglass control. The PN3D8v variant, which utilizes mid-point strain for stress updates, behaves similarly to PN3D8. However, in one example, a noticeable delay in capturing the yield stress was observed with PN3D8v. For two-scale material models based on FOCH, the speedup achieved by PN3D8 over C3D8 was approximately 7 for both small and large deformation problems studied. This speedup was slightly lower than the speedup provided by the one-point integration element, C3D8R. The computational cost of PN3D8 is comparable to its variant PN3D8v, but PN3D8 seems to capture the overall behavior of the element more accurately, especially in cases of highly nonuniform deformation fields (as depicted in Figures 2.3 and 2.4). The effect of the macroscopic problem size was not studied, as the speedup depends on various factors such as the size of the fine-scale problem and the solver employed on both scales.

For two-scale material models based on ROH, the speedup offered by PN3D8 and PN3D8v was slightly higher than 3. However, the speedup provided by C3D8R was almost twice as high. This discrepancy arises because the evaluation cost of element matrices in fully integrated elements (excluding stress updates) is comparable to the cost of stress updates. On the other hand, the evaluation cost of element matrices in one-point integrated elements (excluding stress updates) is significantly lower than the cost of stress updates. It is important to note that the study only considered a single phase (matrix) as inelastic, which requires solving six nonlinear equations for

the six unknown eigenstrain components at each macroscopic quadrature point. With the addition of additional inelastic phases, the number of unknowns increases by six, and the speed factor provided by C3D8R and PN3D8 is expected to become more similar.

The current study was limited to an 8-node linear hexahedral element, but the methodology can be extended to encompass higher-order hexahedral elements. This extension can be achieved by leveraging the knowledge of a function (stress) and its derivative (constitutive tangent matrix) at all reduced quadrature points, allowing for a higher-order expansion to full integration points. A similar approach can be applied to tetrahedral elements as well. The potential advantages of the nonlocal character of the PN3D8 element for strain softening problems have not been investigated in this study. However, these generalizations are necessary for a wider implementation of the pseudo-nonlocal finite element formulation in practical applications involving computationally intensive material models.

Chapter 3:

Data-physics Driven Reduced Order Homogenization

3.1 Introduction

Multiscale modeling is concerned with the derivation of equations, parameters, and algorithms that describe system behavior at a product level by accounting for the physical processes taking place at finer scales. The rationale for multiscale methods is that there exists a spatial and/or temporal scale where a mathematical model is better understood than at a much coarser product-level scale. Given the fine-scale mathematical model, the coarse-scale equations can be rigorously derived by the process known as upscaling or homogenization rather than stated directly at a product level scale where understanding of the mathematical model is more limited. However, the computational cost of upscaling methods for nonlinear history-dependent problems is often detrimental to the overall performance of multiscale methods hindering their broader utilization in practice (see [6-16] for details on the first- and second-order upscaling methods). Significant advancements have been achieved through the implementation of the Lippmann-Schwinger reformulation of the representative volume problem (RVE) as an equivalent volume integral equation [20]. However, despite the efficient application of the fast Fourier transform (FFT) [53], the practical utilization of this approach has been relatively constrained so far.

Reducing the computational cost of multiscale methods can be achieved through various reduced order methods, which may be based on physics, data, or a combination of the two. The success of these reduced order multiscale methods is attributed to the fact that although their mathematical model, including governing equations, is defined at a fine scale of interest, the quantities of interest (QoI) typically exist at a coarser scale.

It is worth noting that model reduction techniques for multiscale continua models maintain the structure of the constitutive equations of micro-constituents or micro-phases while adjusting the values of constitutive model parameters to fit the observed behavior at the coarse scale and other available information, such as failure characteristics. This adjustment process, often referred to as parameter identification or inverse problem, is justified by the assumption that the in-situ material properties differ from the virgin material properties of the micro-constituents. This discrepancy can be attributed to factors like processing and other influences.

However, it is important to recognize that the calibrated properties of micro-constituents, which match the coarse-scale observations, differ from their virgin counterparts primarily due to errors introduced by the model reduction process, and to a lesser extent, processing factors. While the errors resulting from model reduction can be controlled by incorporating a hierarchy of reduced order models, the computational cost associated with achieving an adequately accurate reduced order multiscale model for engineering design can still be significant.

Among popular physics-based (or model-based) reduced order multiscale methods are the Voronoi cell method [17, 18], the mesh-free reproducing kernel particle method [21], methods of cells [22, 23], the wavelet-based reduced order method [24, 25], the reduced order homogenization methods [30-34] and the nonuniform transformation field methods [36, 37]. We also refer to [38, 39, 41] for recent review articles on multiscale methods with and without model reduction and their practical applications. For integrated reduced order multiscale methods applied to coupled process-product design cycle, we refer to [54-58].

With the advancements in machine learning, data-driven multiscale methods have emerged as a viable alternative to traditional physics-based multiscale modeling. These approaches aim to enhance or replace models based on representative volume elements (RVEs) with single-scale

phenomenological models by leveraging data-driven techniques. Among these approaches [26, 29, 59-71], machine learning techniques, particularly neural networks (NNs), have been successfully employed. One straightforward and commonly used approach is training a fully connected neural network to map coarse-scale strain to coarse-scale stress [59, 64, 65, 70] for path-independent problems. However, implementing this approach in high-dimensional spaces, such as those with a large set of constitutive law parameters, can pose computational challenges. In the context of hyper-elastic materials, a manifold-based reduced order model has been effectively applied [60]. This model utilizes neural networks to map coarse-scale loading parameters to a reduced space, addressing the computational complexity of high-dimensional problems. For path-independent materials effective potential has been identified in the parameter space with dimensions of up to ten [25]. In [77], physics-based constraints, such as objectivity, consistency, dynamic and material stability, have been enforced in the representation of nonlinear elasticity of woven fabrics by a regression artificial neural network (ANN). In recent article [78], an efficient genetic calibration of artificial neural networks has been developed and applied to linear elastic particle-enhanced composite material.

For path-dependent materials, recurrent neural networks (RNNs) based on gated recurrent units have been utilized to capture history- and microstructure-dependent plasticity behavior [66]. These RNNs require a large dataset size to sample various random loading paths and face challenges in extrapolation to predict unseen deformation paths. To overcome some of the limitations of RNNs, long short-term memory (LSTM) architectures have been employed [69]. These architectures have shown promise in alleviating issues such as gradient vanishing and accuracy degradation commonly encountered in recurrent neural networks.

Neural networks are generally prone to issues such as extrapolation and overfitting. Simply increasing the input parameter space as a solution is limited because it exponentially increases the required data points. To overcome these problems, the self-consistent cluster analysis (SCA) multiscale modeling approach [68] has been developed. SCA divides the representative volume element (RVE) problem into distinct clusters with similar mechanical responses, striking a balance between accuracy and efficiency. Through the use of precomputed "interaction tensors," SCA can update the residuals of the clusters, as well as the incremental strains and stresses within each cluster. Additionally, Karapiperis proposed an approach that mitigates the challenges associated with neural networks, offering a non-neural network, data-driven solution that transforms a physics-based constitutive law identification problem into a distance minimization problem [71]. This method selectively samples and identifies sample points that minimize the distance from material history points while adhering to specific physical constraints, effectively addressing issues related to extrapolation and overfitting.

The focus of the present study is on the development of the data-physics driven reduced order homogenization, dpROH hereafter, in an attempt to improve the accuracy of the physics-based reduced order homogenization [21-25] developed by the first author and his associates. The physics-based reduced order homogenization, or pROH hereafter, is a hierarchical multiscale model reduction approach that provides a mathematical framework for controlling model reduction error. Herein, we focus on a single member of the hierarchical sequence that provides the lowest computational cost, which makes it competitive to the phenomenological single-scale models in terms of the computational cost. Our primary objective is to improve the model reduction strategy of the multiscale model in addition to training it for the effective constitutive model parameters of the comprising microconstituents, rather than replacing the multiscale model by a neural network

equipped with hyperparameters. Retaining the multiscale structure takes advantage of the existing constitutive model structure of the microconstituents especially when dealing with history-dependent material models, such as plasticity. Note that an alternative strategy based on replacing the multiscale model by the NN would have, for instance, required to resolve an evolving failure surface of a heterogeneous material with a set of hyperparameters, a daunting feat on its own [79], among other challenges.

The section is organized as follows. In Section 3.2 we review the pROH approach, with the intent of detailing the formulation of the lowest cost member of the hierarchical sequence and identify its shortcomings, followed by exploring the utility of data driven methods to address these shortcomings and ultimately improve its performance. The structure of the data-physics driven reduced order homogenization (dpROH) is presented in Section 3.3. The dpROH consists of the offline and online stages. In the offline stage, an enhanced model reduction strategy based on the data-driven surrogate-based Bayesian inference (BI) modeling approach is conceived. In the online stage, dpROH (rather than the surrogate model employed in the BI process) is utilized for the component level predictions. Numerical examples comparing the pROH and various variants of the dpROH to the reference solution based on the first order computational homogenization (i.e., without model reduction) are given in Section 3.4. For the numerical studies we will take advantage of the recently developed pseudo-nonlocal finite element formulation, which reduces the computational cost of the coarse-scale finite element computations without sacrificing on the solution accuracy and stability. Conclusions and future research directions are given in Section 3.5. Details comprising the data-driven surrogate-based Bayesian inference (BI) framework are given in the Appendix A.

3.2 Identifying shortcomings of physics-based reduced order

homogenization

3.2.1 Review of physics-based reduced order homogenization

We consider fine-scale equations defined over in the representative volume element (RVE) domain

Θ

$$\begin{aligned}
 \sigma_{ij,y_j}^f &= 0 \\
 \varepsilon_{kl}^f(\mathbf{x}, \mathbf{y}) &= \varepsilon_{kl}^c(\mathbf{x}) + u_{(k,y_l)}^*(\mathbf{x}, \mathbf{y}) \\
 \varepsilon_{kl}^c(\mathbf{x}) &= u_{(k,x_l)}^c \\
 \varepsilon_{kl}^*(\mathbf{x}, \mathbf{y}) &= u_{(k,y_l)}^*(\mathbf{x}, \mathbf{y}) \\
 \sigma_{ij}^f(\mathbf{x}, \mathbf{y}) &= L_{ijkl}^f(\mathbf{y}) \left(\varepsilon_{kl}^f(\mathbf{x}, \mathbf{y}) - \mu_{kl}^f(\mathbf{x}, \mathbf{y}) \right) \\
 \mu_{kl}^f(\mathbf{x}, \mathbf{y}) &= \mathcal{H} \left(\sigma_{ij}^f(\mathbf{x}, \mathbf{y}), \varepsilon_{ij}^f(\mathbf{x}, \mathbf{y}), s^f(\mathbf{x}, \mathbf{y}) \right)
 \end{aligned} \tag{3.1}$$

where \mathbf{x} and \mathbf{y} denote the coarse- and fine- scale coordinate systems, respectively. The superscripts c, f, * denote the coarse-scale, the fine-scale, and fine-scale perturbation fields, respectively. All the fields are assumed to be periodic in \mathbf{y} . A comma denotes the partial derivative, and brackets appearing in the subscripts denote the symmetric derivative. $u, \varepsilon, \sigma, \mu, s, L$ are displacements, strains, stresses, eigenstrains (plastic strain herein), state variables, and linear elastic constitutive tensor, respectively. The last equation in (3.1) denotes history-dependent constitutive (plasticity herein) model. Indicical notation with Einstein summation convention over repeated indices is employed throughout. Small deformation theory and perfect interfaces are assumed herein.

To complete the definition of the boundary value problem (3.1), the perturbation u_k^* is subjected to periodic boundary conditions on the RVE boundary $\partial\Theta$ together with its normalization

condition $\int_{\Theta} u_k^* d\Theta = 0$. The latter can be replaced by constraining the vertices $\partial\Theta_{vert}$ of the RVE domain to eliminate its rigid body motion.

The macroscopic physical quantities are defined at each macroscopic (Gauss) point as the volume average of the corresponding quantities at the microscopic sample attached to that point. The relationship between the two scales is defined as

$$\begin{aligned}\sigma_{ij}^c(\mathbf{x}) &= \frac{1}{|\Theta|} \int_{\Theta} \sigma_{ij}^f(\mathbf{x}, \mathbf{y}) d\Theta \\ \varepsilon_{ij}^c(\mathbf{x}) &= \frac{1}{|\Theta|} \int_{\Theta} \varepsilon_{ij}^f(\mathbf{x}, \mathbf{y}) d\Theta \\ L_{ijmn}^c &= \frac{1}{|\Theta|} \int_{\Theta} L_{ijkl}(\mathbf{y}) E_{kl}^{mn}(\mathbf{y}) d\Theta\end{aligned}\tag{3.2}$$

where L_{ijmn}^c the coarse-scale linear elastic constitutive tensor and $E_{kl}^{mn}(\mathbf{y})$ the elastic strain influence function, which can be found from the relation $\varepsilon_{kl}^f(\mathbf{x}, \mathbf{y}) = E_{kl}^{mn}(\mathbf{y}) \varepsilon_{mn}^c(\mathbf{x})$ for linear elastic materials.

In the case of inelastic material behavior, but in the absence of interface discontinuities, the fine-scale strain $\varepsilon_{ij}^f(\mathbf{x}, \mathbf{y})$ is constructed to automatically satisfy the fine-scale equilibrium equation

$$\varepsilon_{ij}^f(\mathbf{x}, \mathbf{y}) = E_{ij}^{kl}(\mathbf{y}) \varepsilon_{kl}^c(\mathbf{x}) + \int_{\Theta} p_{ij}^{kl}(\mathbf{y}, \tilde{\mathbf{y}}) \mu_{kl}^f(\mathbf{x}, \tilde{\mathbf{y}}) d\tilde{\Theta}\tag{3.3}$$

where $p_{ij}^{kl}(\mathbf{y}, \tilde{\mathbf{y}})$ is the so-called eigenstrain transformation function, which can be found by inserting (3.3) into (3.1) and accounting for (3.2b). It is important to note that by virtue of equation (3.3), the governing equations are now redefined in terms of $\sigma_{ij}^f(\mathbf{x}, \mathbf{y})$, $\varepsilon_{ij}^f(\mathbf{x}, \mathbf{y})$ and $\mu_{kl}^f(\mathbf{x}, \mathbf{y})$ all of which are purely related by the fine-scale constitutive equation.

Model reduction is introduced and controlled via the discretization of eigenstrains

$$\mu_{ij}^f(\mathbf{x}, \mathbf{y}) = \sum_{\alpha=1}^M N^{(\alpha)}(\mathbf{y}) \mu_{ij}^{(\alpha)}(\mathbf{x})\tag{3.4}$$

Where $N^{(\alpha)}(\mathbf{y})$ are shape functions, typically chosen as piece-wise constant over M partitions, which yields

$$\begin{aligned}\varepsilon_{ij}^f(\mathbf{x}, \mathbf{y}) &= E_{ij}^{kl}(\mathbf{y}) \varepsilon_{kl}^c(\mathbf{x}) + \sum_{\alpha=1}^{\tilde{M}} P_{ij}^{kl(\alpha)}(\mathbf{y}) \mu_{kl}^{(\alpha)}(\mathbf{x}) \\ P_{ij}^{kl(\alpha)}(\mathbf{y}) &= \int_{\Theta^{(\alpha)}} p_{ij}^{kl}(\mathbf{y}, \tilde{\mathbf{y}}) d\tilde{\Theta}\end{aligned}\quad (3.5)$$

where $\Theta^{(\alpha)}$ denotes the domain of the partition α . The discrete eigenstrain transformation function, $P_{ij}^{kl(\alpha)}(\mathbf{y})$, is computed by constructing the weak form of (3.1) using C^0 continuous periodic test function $w^* \in C^0$ residing in the same space as $u^* \in C^0$ and inserting discretization (3.5) into (3.1). It is instructive to point out that the resulting RVE solution weakly satisfies equilibrium equation.

By controlling discretization of eigenstrains, naturally introduces model hierarchy, where the highest fidelity computational model constitutes to the one-partition-per-finite-element in the RVE domain. In this case the number of unknowns in the nonlinear RVE problem is equal to the number of elements in the RVE times the number of eigenstrain components, i.e., six. On the other hand, in the least expensive computational model, which is the focus of the current investigation, the number of unknowns is equal to the number of micro-phases times six. For instance, for the two-phase material (inclusion and matrix) the number of unknowns is 12, i.e., six for each phase, whereas if one of the phases remains elastic, the number of unknowns reduces to six. For the one partition per phase model considered herein, equation (3.3) is given by

$$\varepsilon_{ij}^{(\beta)}(\mathbf{x}) = E_{ij}^{kl(\beta)} \varepsilon_{kl}^c(\mathbf{x}) + \sum_{\alpha=1}^M P_{ij}^{kl(\beta\alpha)} \mu_{kl}^{(\alpha)}(\mathbf{x}) \quad (3.6)$$

Where

$$E_{ij}^{kl(\beta)} = \frac{1}{|\Theta^{(\beta)}|} \int_{\Theta^{(\beta)}} E_{ij}^{kl(\beta)} d\Theta; \quad P_{ij}^{kl(\beta\alpha)} = \frac{1}{|\Theta^{(\beta)}|} \int_{\Theta^{(\beta)}} P_{ij}^{kl(\alpha)} d\Theta \quad (3.7)$$

with Greek superscripts denote the partition (phases) count and M is the number of total partitions (phases).

Remark 1: The eigenstrain transformation tensor, $P_{ij}^{kl(\beta\alpha)}$, satisfies the following compatibility constraint obtained by averaging the phase strains (3.6) over the RVE domain

$$\sum_{\beta=1}^M P_{ij}^{kl(\beta\alpha)} \phi^{(\beta)} = 0 \quad (3.8)$$

Where $\phi^{(\beta)}$ is the volume fraction of phase β .

3.2.2 Locking of one-partition-per-phase model

Consider a two-phase material with a piecewise constant discretization of eigenstrains and one partition per phase. The undeformed finite element mesh in the RVE is illustrated in Figure 3.1a. The inclusion and matrix domains are denoted by $\Theta^{(2)}$ and $\Theta^{(1)}$, respectively. To illustrate the cause of locking, consider an RVE consisting of a perfectly plastic matrix and elastic fiber subjected to the matrix-dominated mode of deformation, i.e., the coarse-scale strain increment $\Delta \varepsilon_{kl}^c, kl \neq 33$ with x_3 denoting the fiber orientation. We denote the matrix and fiber phases by superscripts $\alpha = 1, 2$, respectively. In an elastic fiber embedded in a perfectly plastic matrix the resulting fine-scale stress increment $\Delta \sigma_{ij}^f(\mathbf{y})$ should vanish for arbitrary $\Delta \varepsilon_{mn}^c$

$$0 = \Delta \sigma_{ij}^f(\mathbf{y}) = L_{ijkl}(\mathbf{y}) E_{kl}^{mn}(\mathbf{y}) \Delta \varepsilon_{mn}^c + L_{ijkl}(\mathbf{y}) \left[P_{kl}^{mn(1)}(\mathbf{y}) - I_{klmn}^{(1)}(\mathbf{y}) \right] \Delta \mu_{mn}^{(1)} \quad (3.9)$$

Assuming elastic strains are negligible in comparison to eigenstrains we have

$$\Delta \varepsilon_{kl}^c = \frac{1}{|\Theta|} \int_{\Theta} \Delta \mu_{kl}^f d\Theta = \phi^{(1)} \Delta \mu_{kl}^{(1)}; \quad \phi^{(1)} = \text{const} \quad (3.10)$$

Figure 3.1b depicts the deformed configuration of the RVE. Since the eigenstrain in the matrix domain is assumed to be constant in the one-partition-per-phase model, the elastic inclusion phase is forced to evolve from the a round to an oval shape. Such a deformation of a stiff elastic inclusion requires considerable force, which the perfectly plastic matrix is unable to exert. This so-called inclusion-locking can be naturally alleviated by increasing the number of partitions per phase, ultimately dramatically increasing the computational cost of the model.

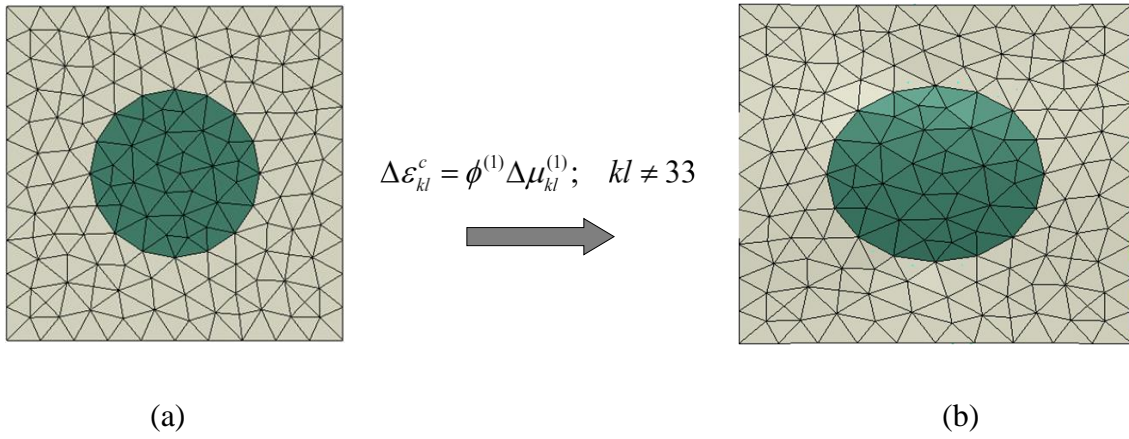


Figure 3.1. Inclusion locking in the matrix-dominated mode of deformation and uniform eigenstrain discretization with one partition per phase; fiber is oriented in x_3 direction

An alternative approach that has been adopted in practice is to redefine the discrete eigenstrain transformation function for the matrix-dominated mode of deformation, denoted as $\hat{P}_{kl}^{mn(1)}(\mathbf{y})$, to satisfy equation (3.9) rather than the discretized weak form of (3.1).

Inserting (3.10) into (3.9) yields

$$0 = \Delta \sigma_{ij}^f = L_{ijkl}(\mathbf{y}) \left[\hat{P}_{kl}^{mn(1)}(\mathbf{y}) - I_{klmn}^{(1)}(\mathbf{y}) + \phi^{(1)} E_{kl}^{mn}(\mathbf{y}) \right] \Delta \mu_{mn}^{(1)} \quad \forall \Delta \mu_{mn}^{(1)} \quad (3.11)$$

Due to arbitrariness of $\Delta \mu^{(1)}$ and positive-definiteness of L , equation (3.11) yields

$$\hat{P}_{kl}^{mn(1)}(\mathbf{y}) \equiv I_{klmn}^{(1)}(\mathbf{y}) - \phi^{(1)} E_{kl}^{mn}(\mathbf{y}) \quad (3.12)$$

For the one-partition-per-phase-model considered herein, the eigenstrain transformation tensor (ETT) for the matrix- $\hat{P}_{kl}^{mn(\alpha\beta)}$ and fiber- $P_{kl}^{mn(\alpha\beta)}$ dominated modes are obtained from equation (3.7).

3.3 Data-physics driven reduced order homogenization (dpROH)

The primary objective of our research is to develop a hybrid data-physics driven reduced-order homogenization (dpROH) approach that combines the benefits of the physics-based reduced order homogenization (pROH) approach, such as interpretability and extrapolation. While the various components comprising dpROH have been previously developed, the novelty of this approach lies in three key aspects:

- (1) Integration of various components into a computationally efficient data-driven surrogate-based Bayesian Inference (BI) engine: We focus on combining different components of dpROH and incorporating them into a data-driven surrogate model, which enables efficient and accurate inference through the Bayesian framework.
- (2) Identification of critical model reduction parameters in the matrix-dominated mode of deformation (denoted as θ^{ETT}), in addition to inferring the fine-scale constitutive model parameters (denoted as θ^{MCM}). This identification process is crucial for achieving accurate model reduction and overall performance improvement.
- (3) Devising an efficient solution strategy to infer the two sets of parameters.

In the following sections, we provide a detailed description of the data-driven surrogate-based Bayesian Inference (BI) framework and further elaborate on the structure of the data-enhanced eigenstrain transformation tensor in the matrix-dominated mode, which contributes to the advancement of the dpROH approach.

3.3.1 The data-driven surrogate-based Bayesian Inverse (BI) framework

In this study, we utilize Bayesian inference (BI) to estimate the microstructural parameters, denoted as $\theta^{ETT}, \theta^{MCM}$, as random variables, allowing us to determine their statistical distribution or mean values. The use of BI provides a framework for quantifying the impact of various sources of uncertainty, including observation error and model uncertainty. Unlike optimization-based methods for parameter identification, BI requires an efficient forward simulation engine, as the forward problem needs to be solved numerous times in a sequential manner. While the physics-based reduced-order homogenization (pROH) method is a highly efficient reduced-order multiscale solver, the computational time required for performing thousands of forward multiscale simulations, even with model reduction, can still be overwhelming. Hence, it is advantageous to employ pROH solely for training the surrogate model and then utilize the surrogate model for conducting a multitude of forward simulations within the Bayesian framework, resulting in computational efficiency.

For constructing our surrogate model, we will utilize the Gated Recurrent Unit (GRU) neural network. The GRU has demonstrated efficient performance in handling interpolation problems as well as path-dependent problems, which are relevant to the present study. One advantage of using the GRU-based surrogate is that the construction of the training dataset naturally lends itself to parallelization, allowing for efficient utilization of computational resources. Moreover, the construction of the training dataset requires significantly fewer forward simulations using the physics-based reduced-order homogenization (pROH) method compared to the number of forward simulations needed within the sequential Bayesian Inference (BI) framework.

Figure 3.2 illustrates the flowchart of the data-physics driven reduced order homogenization (dpROH) approach, comprising two stages: offline and online. The objective of the offline stage

is to construct probability density distribution functions (PDFs) for the eigenstrain transformation tensor and the microstructural constitutive model parameters, denoted as $P(\theta^{ETT})$ and $P(\theta^{MCM})$, respectively. Alternatively, in the case of deterministic component-level predictions, the mean values of $\bar{\theta}^{ETT}$ and $\bar{\theta}^{MCM}$ are computed. The offline stage begins with the execution of uniform field physical experiments, which are substituted with simulations utilizing a high-fidelity multiscale model based on first-order computational homogenization (FOCH), capable of resolving microstructural details. The selection of uniform field experiments allows for conducting surrogate training at the Representative Volume Element (RVE) level, significantly reducing the computational cost of surrogate training. The Gated Recurrent Unit (GRU) neural network-based surrogate (Box 2 in Figure 3.2) is trained by subjecting an RVE to uniform coarse-scale strain ε^c histories (Box 1 in Figure 3.2) and calculating the homogenized stress $\sigma^c(\varepsilon^c, \theta^{ETT}, \theta^{MCM})$ for various model parameters $\theta^{ETT}, \theta^{MCM}$. Subsequently, Bayesian Inference employing the GRU-based surrogate (Box 3 in Figure 3.2) is carried out to infer the PDFs of the model parameters. The online stage (Box 4 in Figure 3.2) aims to make predictions at the component level based on the PDFs of model parameters $P(\theta^{ETT})$ and $P(\theta^{MCM})$, or alternatively, their mean values $\bar{\theta}^{ETT}$ and $\bar{\theta}^{MCM}$. It is important to note that the surrogate model is not expected to provide accurate predictions outside the training set. Therefore, the online stage employs a two-scale solver based on the data-physics driven reduced order homogenization (dpROH) approach (as depicted in Figure 3.2). The predictions at the component level can be either probabilistic or deterministic, depending on whether the PDFs or mean values $\bar{\theta}^{ETT}$ and $\bar{\theta}^{MCM}$ are used. Herein, we focus on

deterministic component-level predictions by utilizing the mean values $\bar{\theta}^{ETT}$ and $\bar{\theta}^{MCM}$.

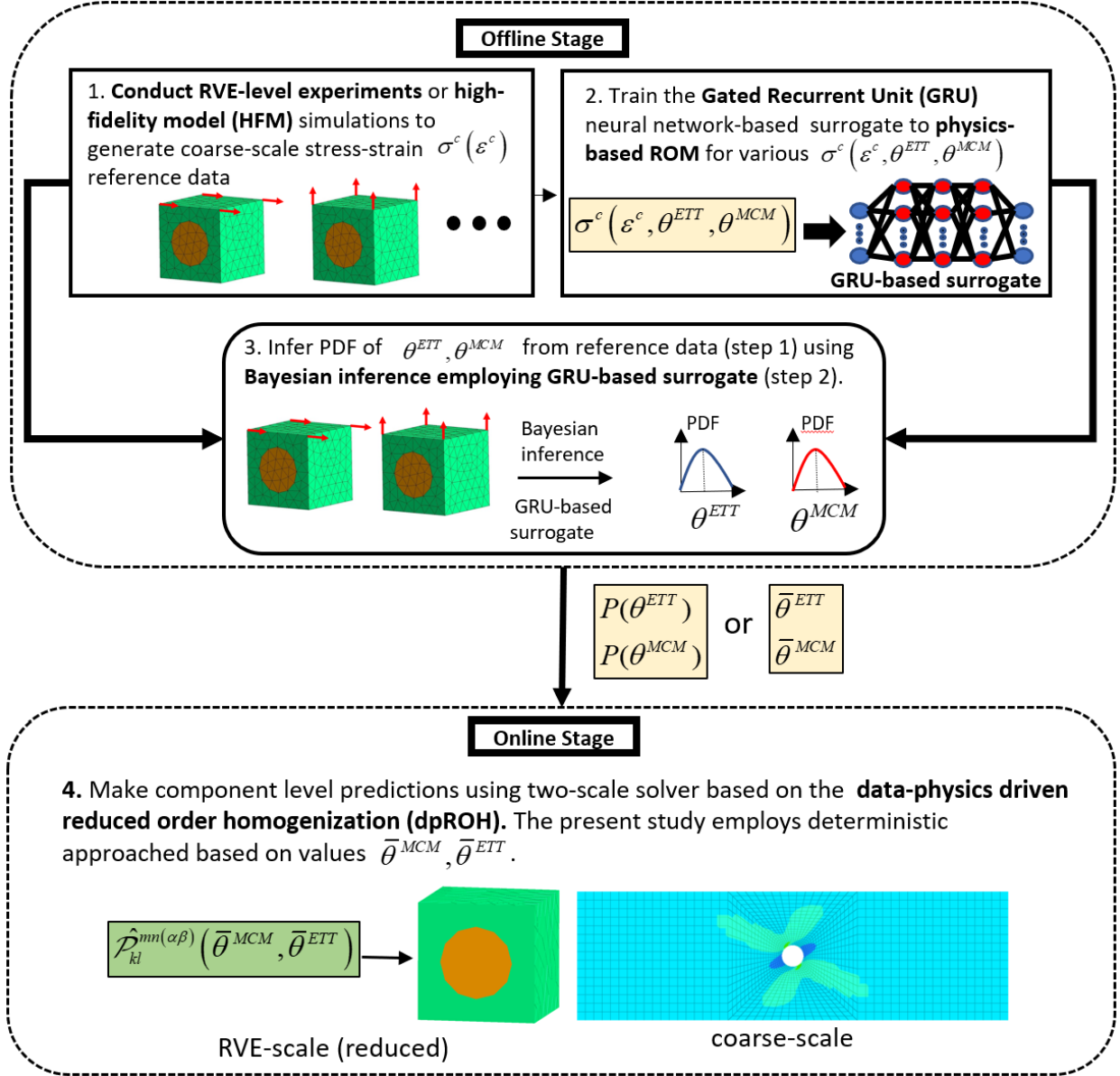


Figure 3.2. Flowchart of the data-physics driven reduced order homogenization

Details on the training experiments for the two material systems are given in Section 3.4. Components of the data-driven surrogate-based Bayesian inverse modeling approach including the Bayesian Inference and Gated Recurrent Unit (GRU) based surrogate model, are given in Appendix A for self-consistency of the dissertation.

3.3.2 Revised eigenstrain transformation tensor for the matrix dominated mode

As mentioned in Section 3.2 that while the eigenstrain transformation tensor for the matrix-dominated mode $\hat{P}_{kl}^{mn(\alpha\beta)}$ alleviates locking neither the compatibility constraint (3.10) nor the weak equilibrium are satisfied in the matrix-dominated mode of deformation. In seeking to enhance the physics-based model reduction scheme by taking advantage of the available data we will attempt to answer the following key questions:

- (i) Is there a better (or nearly optimal) eigenstrain transformation tensor in the matrix dominated mode, denoted hereafter as $\hat{\mathcal{P}}_{kl}^{mn(\alpha\beta)}$, than $\hat{P}_{kl}^{mn(\alpha\beta)}$ computed from (3.12)?
- (ii) Is it possible to compute $\hat{\mathcal{P}}_{kl}^{mn(\alpha\beta)}(\theta^{ETT}, \theta^{MCM})$ by modifying $\hat{P}_{kl}^{mn(\alpha\beta)}$ with a small set of eigenstrain transformation tensor parameters θ^{ETT} ?
- (iii) How strongly does the eigenstrain transformation tensor parameters θ^{ETT} depend on the microstructural constitutive model θ^{MCM} parameters representing the microstructural plasticity model parameters in the present study?
- (iv) Should the two sets, θ^{ETT} , θ^{MCM} , be computed simultaneously or can they be computed sequentially, and in which order, using the data-driven surrogate-based Bayesian Inference (BI) framework proposed herein?
- (v) Would the inferred set of parameters, θ^{MCM} , θ^{ETT} , result in superior component level predictions outside the training set by the two-scale solver (rather than the surrogate employed for forward simulations in BI) equipped with $\hat{\mathcal{P}}_{kl}^{mn(\alpha\beta)}$?

The eigenstrain transformation tensor in the matrix dominated mode, $\hat{\mathcal{P}}_{kl}^{mn(\alpha\beta)}$, possesses minor symmetries, i.e., $\hat{\mathcal{P}}_{kl}^{mn(\alpha\beta)} = \hat{\mathcal{P}}_{kl}^{nm(\alpha\beta)} = \hat{\mathcal{P}}_{lk}^{mn(\alpha\beta)}$, due to the symmetry of strain and eigenstrain denoted by Roman indices. In total it consists of $M^2 N^2$ terms where M is the number of matrix-

dominated modes and N is the number of phases or microconstituents. For instance, in the fibrous composite RVE (Figure 3.3a), $M=5$ and $N=2$, whereas in the woven composite RVE (Figure 3.3b), $M=4$ and $N=3$. As mentioned earlier, in the fibrous composite RVE, the two phases (denoted in Greek indices) are matrix ($\alpha = 1$) and fiber ($\alpha = 2$) with the matrix-dominated modes being 11, 22, 12, 13 and 23 (see the definition of the material coordinate system in Figure 3.3). In the woven composite RVE, the three phases are matrix ($\alpha = 1$) and two tows ($\alpha = 2, 3$) with the matrix dominated modes being 33, 12, 13 and 23. Accounting for symmetry of the RVE microstructure, the number of independent modes, M_s , can be further reduced, $M_s \leq M$. For the fibrous composite RVE, $M_s = 3$, corresponding to strain (eigenstrain) components 11 (or 22), 12, 13 (or 23). For the woven composite RVE, $M_s = 3$, corresponding to strain (eigenstrain) components 33, 12, 13 (or 23).

We consider phase interaction symmetries to further reduce the number of independent terms in $\hat{\mathcal{P}}_{kl}^{mn(\alpha\beta)}$. For the fibrous composite RVE, the following independent phase-to-phase interactions (corresponding to superscripts $\alpha\beta$ in $\hat{\mathcal{P}}_{kl}^{mn(\alpha\beta)}$) exist: 11, 12, 21, 22 where the second and first superscripts denote the phase of the induced eigenstrain (input) and the phase of the resulting strain (output), respectively. Note that the above four interactions coincide with N^2 for the two-phase material. For the woven composite RVE, we will take advantage of certain symmetries by assuming that the interaction of each of the two tows (phases 2 and 3) with the matrix phase, i.e., 12-13 and 21-31, are identical (in the corresponding orthogonal coordinate systems) and that the interactions of each tow with itself, i.e., 22-33 and between the tows, 23-32 are also identical. Given the above considerations the number of independent phase interactions are as follows: 11, 22, 12, 21, 23. Finally, we will take advantage of the diagonal dominance of $\hat{\mathcal{P}}_{kl}^{mn(\alpha\beta)}$ with respect

to indices kl and mn , which emanates from the fact that imposed eigenstrain mode mn by at large dominates the strain component mn . This is also reminiscent of the diagonal dominance of the linear elastic stiffness matrix. The selected terms in $\hat{\mathcal{P}}_{kl}^{mn(\alpha\beta)}$ will be obtained by rescaling the corresponding terms in $\hat{P}_{kl}^{mn(\alpha\beta)}$ as follows:

$$\hat{\mathcal{P}}_{ij}^{ij(\alpha\beta)} = \alpha_I \hat{P}_{ij}^{ij(\alpha\beta)} \quad \text{no sum on repeated indices} \quad (3.13)$$

where α_I is termed as the eigenstrain transformation tensor rescaling parameter, or simply rescaling parameter comprising the set $\theta^{ETT} = \{\alpha_I\}$. The rescaling parameter for the two microstructures is defined in Table 3.1.

We will consider two scenarios with respect to the rescaling parameters. In the first case the rescaling parameters depicted in Table 3.1 will be considered to be independent. In the second case we will impose the compatibility constraint (3.8), and consequently reduce the number of independent parameters. Table 3.2 depicts the independent rescaling parameters for the latter case; the remaining rescaling parameters are computed from the compatibility constraint (3.8).

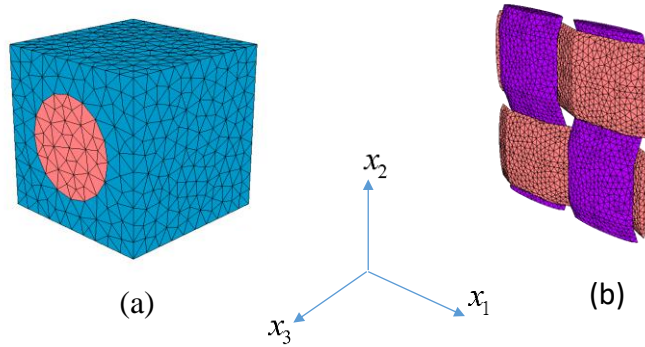


Figure 3.3. Representative volume elements and material coordinate system considered in the present study. (a) fibrous composite RVE, (b) woven composite RVE (only tows are shown)

Table 3.1. Definition of rescaling parameters

Fibrous composite RVE		Woven Composite RVE	
Rescaling	Transformation Tensor	Rescaling	Transformation Tensor

α_1	$\hat{P}_{11}^{11(11)}, \hat{P}_{22}^{22(11)}$	α_1	$\hat{P}_{23}^{23(11)}, \hat{P}_{13}^{13(11)}$
α_2	$\hat{P}_{23}^{23(11)}, \hat{P}_{13}^{13(11)}$	α_2	$\hat{P}_{12}^{12(11)}$
α_3	$\hat{P}_{12}^{12(11)}$	α_3	$\hat{P}_{23}^{23(21)}, \hat{P}_{13}^{13(31)}$
α_4	$\hat{P}_{11}^{11(21)}, \hat{P}_{22}^{22(21)}$	α_4	$\hat{P}_{23}^{23(31)}, \hat{P}_{13}^{13(21)}$
α_5	$\hat{P}_{23}^{23(21)}, \hat{P}_{13}^{13(21)}$	α_5	$\hat{P}_{12}^{12(21)}, \hat{P}_{12}^{12(31)}$
α_6	$\hat{P}_{12}^{12(21)}$		

Table 3.2. Definition of independent rescaling parameters; remaining parameters computed from (3.8)

Fibrous composite RVE		Woven Composite RVE	
Rescaling	Transformation Tensor	Rescaling	Transformation Tensor
α_1	$\hat{P}_{22}^{22(21)}$	α_1	$\hat{P}_{23}^{23(21)}$
α_2	$\hat{P}_{13}^{13(21)}$	α_2	$\hat{P}_{13}^{13(21)}$
α_3	$\hat{P}_{12}^{12(21)}$	α_3	$\hat{P}_{12}^{12(21)}$

3.4 Numerical examples

In this section, we study the performance of dpROH for small deformation two-scale problems.

We consider several variants of the dpROH to answer the questions raised in Section 3.3.2. The

variant v1 interchangeably denoted as $\text{dpROH}(\theta^{MCM})$, where constitutive model parameters are

inferred from four independent deformation tests (three matrix-dominated deformation test and

one fiber-dominated deformation test). This variant is essentially the physics-based reduced-order

homogenization with calibrated constitutive model material parameters. The v2 variant referred to

as $\text{dpROH}(\theta^{MCM} + \theta^{ETT})$, which infers simultaneously both constitutive model parameters and

eigenstrain transformation tensor rescaling parameters from the above four tests. The v3 variant

$\text{dpROH}(\theta^{MCM} \rightarrow \theta^{ETT})$ fixes the inferred constitutive model material parameters from the dpROH

(θ^{MCM}) variant followed by the inference of θ^{ETT} from three matrix-dominated tests. The v4

variant or $\text{dpROH}(\theta^{ETT} \rightarrow \theta^{MCM})$, is a sequential process similar to v3, but is carried out in reverse order. The remaining three variants (v5, v6, v7) referred to as $\text{dpROH}(\theta^{MCM} + \theta_{com}^{ETT})$, $\text{dpROH}(\theta^{MCM} \rightarrow \theta_{comp}^{ETT})$, and $\text{dpROH}(\theta_{comp}^{ETT} \rightarrow \theta^{MCM})$, respectively, adopt a similar inference strategy as v2, v3 and v4 with only difference that the compatibility constraint (3.8) as described in the previous section is enforced. The above two notations identifying specific dpROH variant will be used interchangeably.

3.4.1 Setting the bounds on model parameters

We consider a classical J2 plasticity theory with the yield stress Y_0 , and the isotropic hardening parameter δ , as the microstructural constitutive model parameters θ^{MCM} . For the fibrous composite material $\theta^{MCM} = [Y_0^{(1)}, \delta^{(1)}, Y_0^{(2)}, \delta^{(2)}]$ where the superscripts denote the two phases as described in the previous section. Herein, the distributions of model reduction and materials parameters are assumed to be uniform. The bounds of various parameters can be adjusted given the BI results. The bounds for the constitutive model parameters are given in Table 3.3. The units of all model parameters have been normalized. The bounds for the rescaling parameters α_l of the corresponding eigenstrain transformation tensor are given in Table 3.4. For the woven composite material, the corresponding bounds on θ^{MCM} and θ^{ETT} are given in Table 3.5 and Table 3.6, respectively.

Table 3.3. Bounds on θ^{MCM} for the fibrous composite RVE

θ^{MCM}	$Y_0^{(1)}$	$\delta^{(1)}$	$Y_0^{(2)}$	$\delta^{(2)}$
Bounds	[15~45]	[20~100]	[180~220]	[20~150]

Table 3.4. Bounds on rescaling parameters for the fibrous composite RVE

θ^{ETT}	α_I
Bounds	[0.5~2.0]

Table 3.5. Bounds on θ^{MCM} for the woven composite RVE

θ^{MCM}	$Y_0^{(1)}$	$\delta^{(1)}$	$Y_0^{(2)}, Y_0^{(3)}$	$\delta^{(2)}, \delta^{(3)}$
Bounds	[20~40]	[40~300]	[100~220]	[20~200]

Table 3.6. Bounds on rescaling parameters for the woven composite RVE

θ^{ETT}	α_I
Ranges	[0.5~1.5]

Once the initial distribution of model parameters is selected, the training data set is generated to train the neural network for the individual deformation modes at the RVE level. For each independent mode 5000 RVE simulations are conducted using pROH. All simulations are displacement driven. For details on the GRU Neural Networks see Appendix A2.

3.4.2 Fibrous composite

The fibrous composite RVE consisting of two phases is discretized with 1558 four-node tetrahedral elements. The fiber volume fraction is 24.56%. Both phases are modeled using J2 plasticity with isotropic hardening. The first-order computational homogenization (FOCH) is used as the reference solution. The material constants employed in the FOCH are summarized in Table 3.7. Four independent FOCH tests at the RVE level that mimic uniform field physical experiments are considered. These tests are fed into the data-driven surrogate-based Bayesian Inference (BI) engine to infer θ^{MCM} and θ^{ETT} as discussed in the previous section.

Table 3.7. Reference material properties of fibrous composite RVE

Material property	Matrix	Fiber
Young's Modulus	3800	190000
Poisson's ration	0.32	0.01
Yield strength	30	200
Ultimate strength	65	250
Exponent for the evolution law	45	120
Linear hardening law	0	0

3.4.2.1 Inference (identification) tests

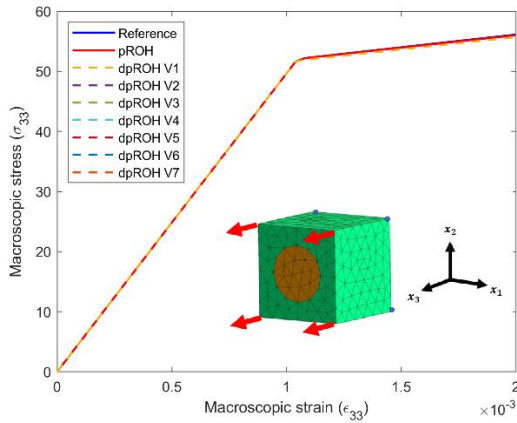
Figure 3.4 illustrates the four first-order computational homogenization (FOCH) simulations that serve as the reference solutions. Additionally, the results of pROH without calibration are presented for comparison. Figure 3.4a demonstrates that pROH accurately predicts fiber-dominated deformation (mode 33). However, for matrix-dominated deformation modes 22, 12, and 13 (Figures 3.4b, 3.4c, 3.4d), pROH exhibits a delayed inelastic behavior. In comparison, dpROH v1 (or $\text{dpROH}(\theta^{MCM})$), where only effective microstructural properties of plasticity are inferred, exhibits notable improvement in transverse tension and in-plane shear (Figures 3.4b, 3.4c). However, it appears too stiff in transverse shear (Figure 3.4d). Similar behavior is observed in all other dpROH variants. The mean values of model parameters for each dpROH variant, inferred through Bayesian Inference (BI), are summarized in Table 3.8. Figure 3.5 displays the probability density distribution obtained from BI inference for the constitutive model parameters corresponding to the $\text{dpROH}(\theta^{MCM})$. It should be noted that similar distributions obtained for other dpROH variants are not shown for brevity.

As expected, all dpROH variants perform equally well in reproducing the reference solution used for model parameter identification. Next, we aim to demonstrate that dpROH, with inferred model

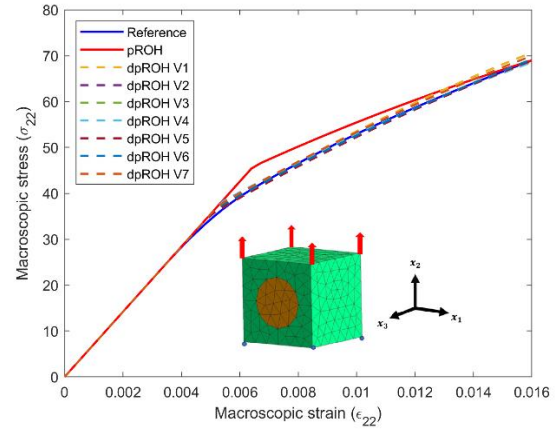
parameters, is not only capable of accurately reproducing the calibration and training datasets but also exhibits predictive capabilities outside the training dataset.

Table 3.8. Inferred mean values of model parameters ($\bar{\theta}^{ETT}$, $\bar{\theta}^{MCM}$) for various dpROH

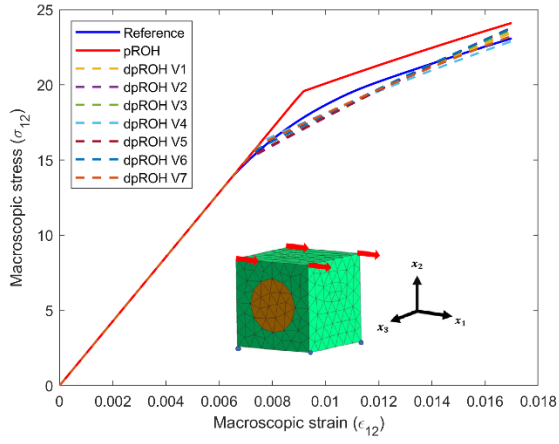
	dpROH v1	dpROH v2	dpROH v3	dpROH v4	dpROH v5	dpROH v6	dpROH v7
$Y_0^{(1)}$	23.901	22.95	23.901	24.9	22.774	23.901	24.488
$\delta^{(1)}$	66.899	78.415	66.899	65.225	107.788	66.899	73.69
$Y_0^{(2)}$	198.811	199.889	198.811	192.095	199.733	198.811	201.181
$\delta^{(2)}$	114.618	116.757	114.618	84.483	122.434	114.618	72.377
α_1	N/A	0.874	0.773	0.59	0.833	1.098	1.134
α_2	N/A	0.867	0.862	0.939	0.899	0.917	1.196
α_3	N/A	0.659	0.747	0.502	1.506	1.846	1.942
α_4	N/A	1.139	1.077	1.112	N/A	N/A	N/A
α_5	N/A	1.022	0.956	1.176	N/A	N/A	N/A
α_6	N/A	1.858	1.734	1.754	N/A	N/A	N/A



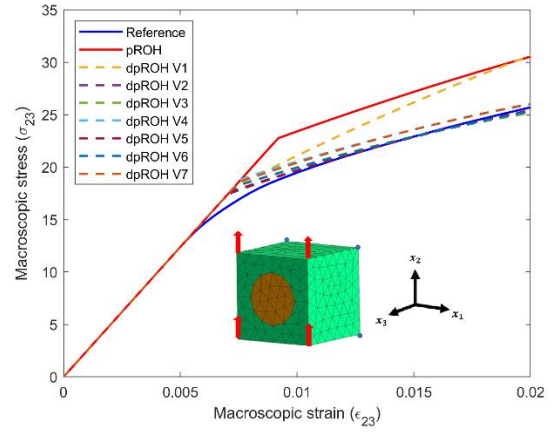
(a)



(b)

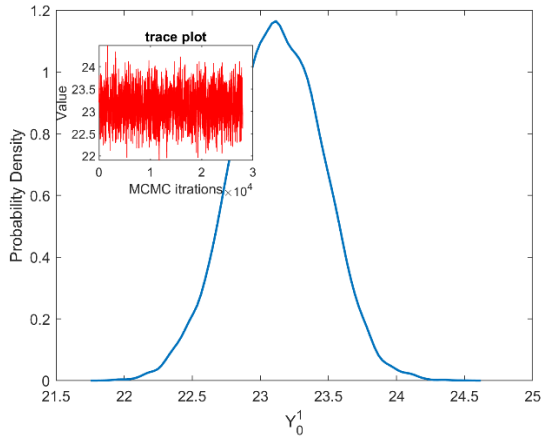


(c)

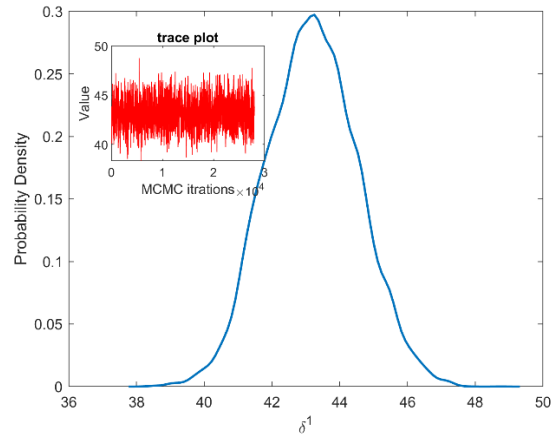


(d)

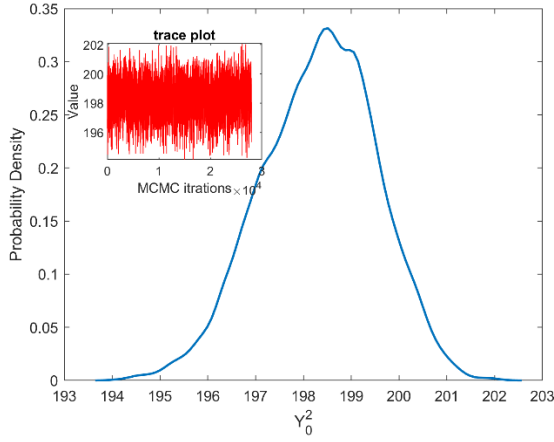
Figure 3.4. Comparison of ROH variants to the reference macroscopic stress-strain solution for (a) fiber dominated tension - 33 (b) transverse tension - 22 (c) in plane shear - 12 (d) transverse shear - 23.



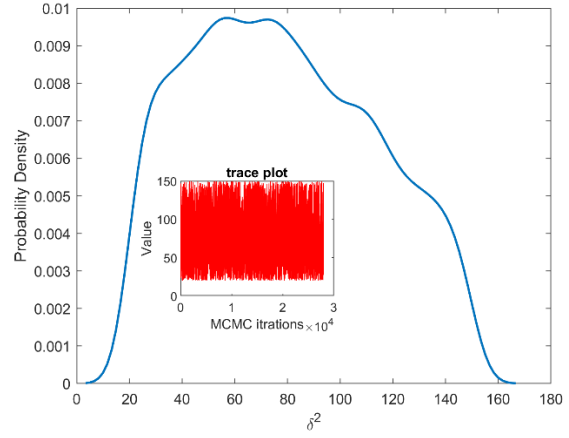
(a)



(b)



(c)



(d)

Figure 3.5. The probability density functions of four material parameters $[Y_0^{(1)}, \delta^{(1)}, Y_0^{(2)}, \delta^{(2)}]$ as obtained by Bayesian inference for $\text{dpROH}(\theta^{MCM})$; The trace plots are shown as subplots.

3.4.2.2 Validation for the mixed mode uniform field cyclic loading

In this example, we investigate an eight-node hexahedral macroscopic element representing a fibrous composite Representative Volume Element (RVE) that is subjected to a mixed-mode (12 and 23) cyclic loading condition. It's important to note that this specific mixed-mode loading scenario was not included in either the calibration or training datasets.

Figure 3.6 presents the force-displacement curves at a single node within the RVE, as well as the overall transverse shear stress-strain relationships. It is evident that both pROH and dpROH v1 fail to accurately reproduce the reference solution due to the softer inferred hardening slope. However, all other variants of dpROH exhibit reasonably accurate predictions.

These results suggest that while pROH and dpROH v1 struggle to capture the complex behavior of the mixed-mode loading condition, the other dpROH variants perform significantly better.

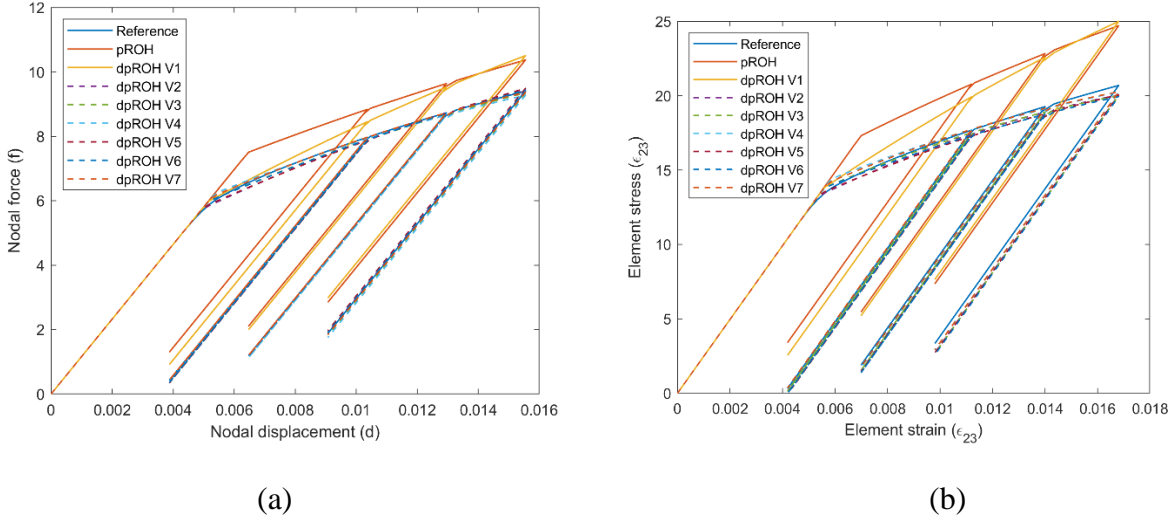


Figure 3.6. Mixed mode uniform field cyclic loading (a) Force-displacement relation (b) Transverse shear macroscopic stress-strain relation.

3.4.2.3 Validation on the open hole quasi-isotropic plate

For the non-uniform field validation, we consider an open hole quasi-isotropic plate subjected to axial tension, shear and three-point bending. The plate dimensions are as follows: thickness 1.088, width 24, length 96, radius of the hole 4. The laminate layup from the top to the bottom is: 0, -45, +45, 90, 90, +45, -45, 0. The plate consists of 5920 eight-node hexahedral macroscopic elements. For estimating solution quality, we track the error in the critical element (i.e., having the largest error) in the plate. The normalized accumulated error in the stress over the loading history is defined as

$$\text{Error}(\sigma_{ij}^{v_l}) = \sqrt{\frac{\int_t (\sigma_{ij}^{ref} - \sigma_{ij}^{v_l})^2 dt}{\int_t (\sigma_{ij}^{ref})^2 dt}} \quad (3.14)$$

Where σ denotes either the coarse-scale stress, or an overall phase (matrix or fiber) stress. In other words, we will report an error in both the homogenized and the overall phase stresses in the critical

element. σ_{ij}^{ref} , $\sigma_{ij}^{v_l}$ denote the stresses for the reference solution and for one of the dpROH variants, respectively.

The errors in the quasi-isotropic plate subjected to axial tension, shear and three-point bending are summarized in Tables 3.9, 3.10, 3.11 respectively. The von Mises stress distributions for the corresponding reference solution are shown in Figures 3.7, 3.8, 3.9.

Not surprisingly, the axial tension problem is fiber dominated so we see little difference in the accuracy of various methods. As the laminate undergoes significant matrix-dominated deformation in the three-point bending and the in-plane shear tests (Tables 3.10 and 3.11), the dpROH variants (v2-v7) that infer eigenstrain transformation tensor parameters offer improved accuracy not only in the coarse-scale stresses but also in the individual overall phase stresses. The latter is somewhat surprising since the inference was based on matching the coarse-scale behavior to mimic the data available from physical experiments that do not typically provide individual phase stresses.

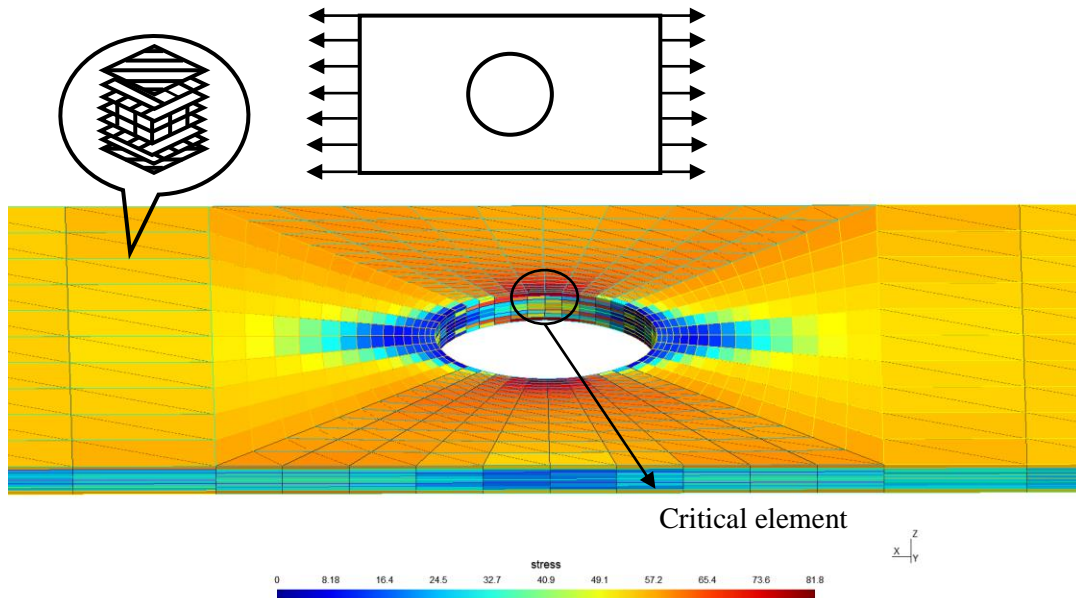


Figure 3.7. FOCH solution for the von Mises stress distribution in the quasi-isotropic plate (fibrous composite microstructure) subjected to axial tension. Boundary conditions, laminate orientations, and location of the critical element are shown.

Table 3.9. Critical element error. Fibrous composite. Axial tension test

Variant of ROH	Homogenized	Matrix	Fiber
pROH	1.8872	1.3673	2.1063
dpROH(θ^{MCM})	1.0181	0.5194	1.8394
dpROH($\theta^{MCM} + \theta^{ETT}$)	0.401	1.0118	0.783
dpROH($\theta^{MCM} \rightarrow \theta^{ETT}$)	1.268	1.6186	2.5003
dpROH($\theta^{ETT} \rightarrow \theta^{MCM}$)	0.7857	1.7099	0.9128
dpROH($\theta^{MCM} + \theta_{comp}^{ETT}$)	0.4193	1.1684	0.8795
dpROH($\theta^{MCM} \rightarrow \theta_{comp}^{ETT}$)	0.593	0.87	1.0058
dpROH($\theta_{comp}^{ETT} \rightarrow \theta^{MCM}$)	0.8352	1.0172	1.2942

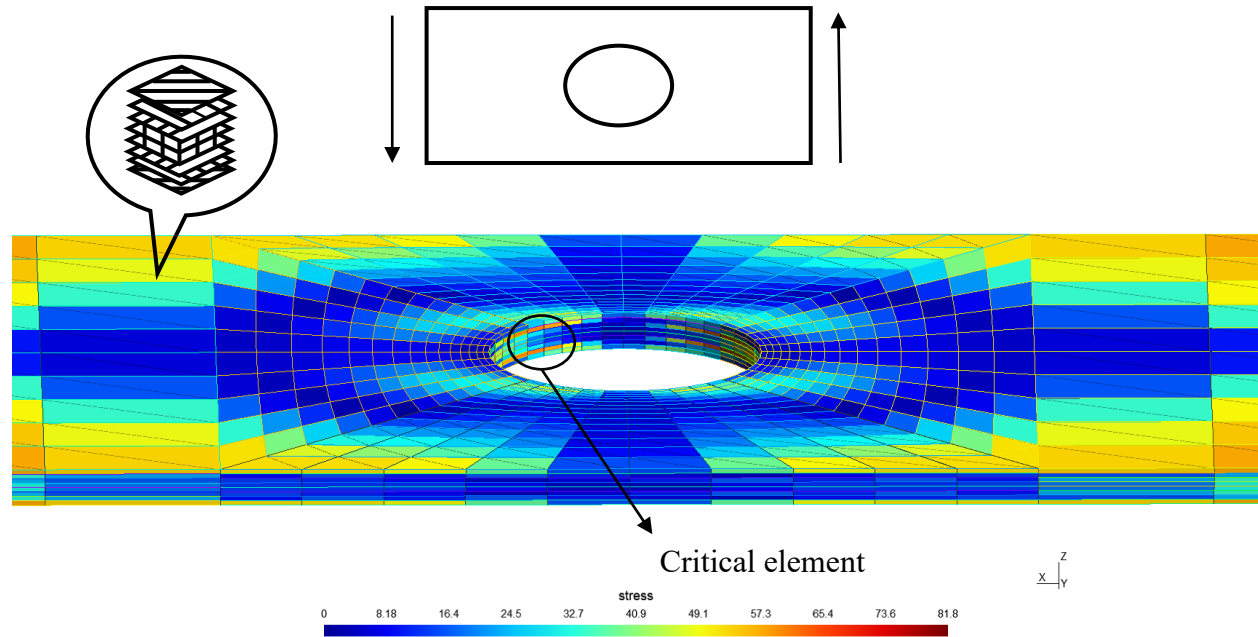


Figure 3.8. FOCH solution for the von Mises stress distribution in the quasi-isotropic plate (fibrous composite microstructure) subjected to in plane shear. Boundary conditions, laminate orientations, and location of the critical element are shown.

Table 3.10. Critical element error. Fibrous composite. In plane shear test

Variant of ROH	Homogenized	Matrix	Fiber
pROH	6.7922	12.8978	9.713
dpROH (θ^{MCM})	2.9245	9.5631	9.1664
dpROH ($\theta^{MCM} + \theta^{ETT}$)	1.9357	4.1203	2.9931
dpROH ($\theta^{MCM} \rightarrow \theta^{ETT}$)	2.5884	4.3076	4.112
dpROH ($\theta^{ETT} \rightarrow \theta^{MCM}$)	2.1742	5.6002	4.6239
dpROH ($\theta^{MCM} + \theta_{comp}^{ETT}$)	2.1041	5.3452	3.0753
dpROH ($\theta^{MCM} \rightarrow \theta_{comp}^{ETT}$)	2.3025	5.0509	3.4667
dpROH ($\theta_{comp}^{ETT} \rightarrow \theta^{MCM}$)	2.0372	5.071	3.8675

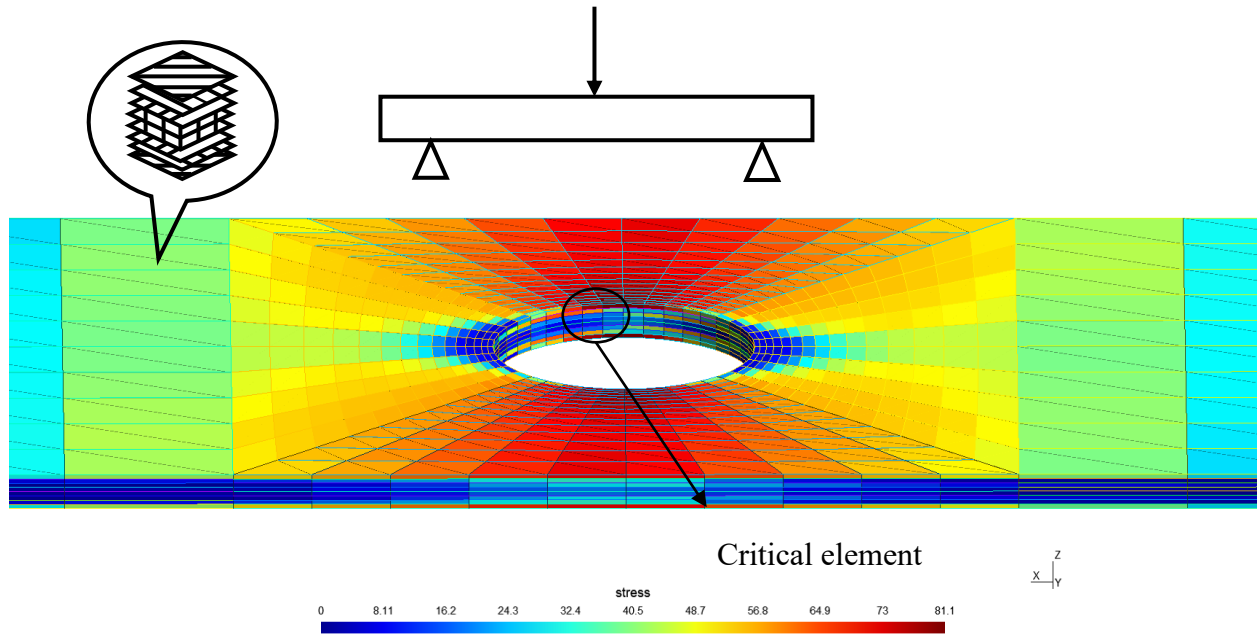


Figure 3.9. FOCH solution for the von Mises stress distribution in the quasi-isotropic plate (fibrous composite microstructure) subjected to three-point bending. Boundary conditions, laminate orientations, and location of the critical element are shown.

Table 3.11. Critical element error. Fibrous composite. Three-point bending test

Variant of ROH	Homogenized	Matrix	Fiber
pROH	10.4455	8.8976	5.4456
dpROH (θ^{MCM})	5.8643	3.8879	3.2607
dpROH ($\theta^{MCM} + \theta^{ETT}$)	2.5339	3.0924	1.7032
dpROH ($\theta^{MCM} \rightarrow \theta^{ETT}$)	3.3753	3.6466	2.2665
dpROH ($\theta^{ETT} \rightarrow \theta^{MCM}$)	3.9056	4.4637	2.2059
dpROH ($\theta^{MCM} + \theta_{phys}^{ETT}$)	2.7082	2.1027	1.6594
dpROH ($\theta^{MCM} \rightarrow \theta_{phys}^{ETT}$)	3.4616	2.9547	2.0178
dpROH ($\theta_{phys}^{ETT} \rightarrow \theta^{MCM}$)	4.5651	4.5891	2.5246

3.4.3 Woven composite

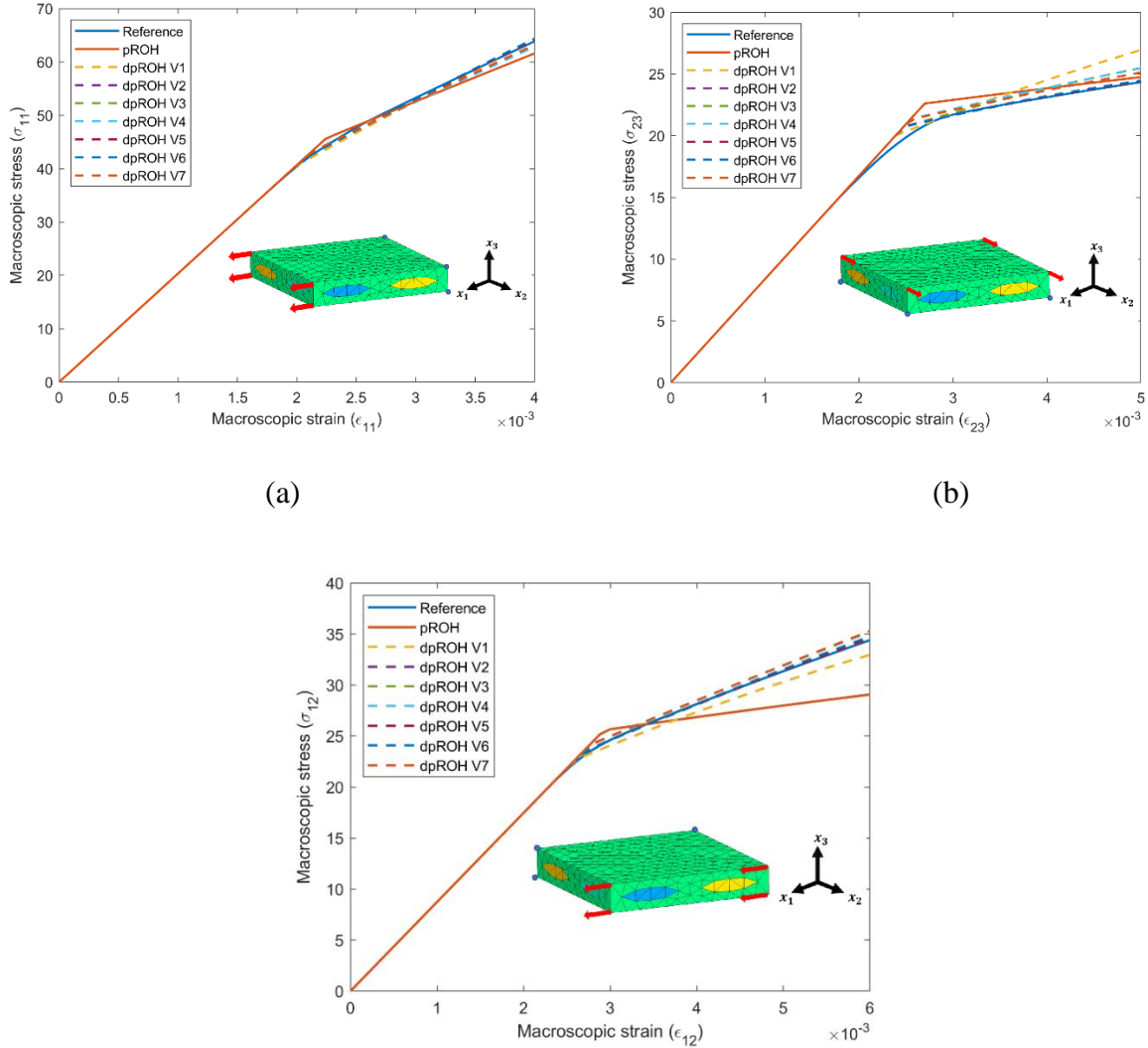
Herein, we consider an idealized woven composite material where tows are assumed to be isotropic, and consequently, the woven RVE is modeled as a two-scale material. The woven composite RVE is assumed to consists of three phases with material constants summarized in Table 3.12. The woven composite RVE is discretized with 1,748 four-node tetrahedral elements. The volume fraction of matrix is 61.88%, and of each tow 19.06%.

Table 3.12. Reference material properties of the woven composite RVE

Material property	Matrix	Tows
Young's Modulus	15000	30000
Poisson's ration	0.15	0.16
Yield strength	30	200
Ultimate strength	65	250
Exponent for the evolution law	45	120
linear hardening	0	0

3.4.3.1 Inference (identification) tests

For model identification, we consider three sets of experiments corresponding to the in-plane tension (mode 11), the transverse shear (mode 23) and the in-plane shear (mode 12). Figure 3.10 compares various ROH variant to the reference solution. Similar observations to those made for the fibrous composite RVE can be made here even though the differences between the methods are somewhat less pronounced. This is because the woven composite RVE is reinforced in both directions as opposed to just one direction for the fibrous composite RVE. Table 3.10 summarizes the mean values of model parameters for each dpROH variant inferred by BI.



(c)

Figure 3.10. Comparison of ROH variants to the reference macroscopic stress-strain solution for (a) in plane (tow dominated) tension - 11 (b) transverse shear – 23 (c) in plane shear – 12.

Table 3.13. Inferred mean values of model parameters ($\bar{\theta}^{ETT}$, $\bar{\theta}^{MCM}$) for various dpROH

	dpROH v1	dpROH v2	dpROH v3	dpROH v4	dpROH v5	dpROH v6	dpROH v7
$Y_0^{(1)}$	32.051	32.056	32.051	33.044	32.13	32.051	32.967
$\delta^{(1)}$	194.554	191.432	194.554	121.893	184.524	194.554	135.768
$Y_0^{(2)}, Y_0^{(3)}$	182.603	157.91	182.603	166.933	167.449	182.603	166.526
$\delta^{(2)}, \delta^{(3)}$	116.055	108.353	116.055	102.322	108.144	116.055	140.459
α_1	N/A	1.197	1.07	0.914	1.367	1.381	1.137
α_2	N/A	0.774	0.767	0.738	1.407	1.421	1.255
α_3	N/A	1.313	1.372	1.17	0.958	0.959	0.787
α_4	N/A	1.315	1.003	0.988	N/A	N/A	N/A
α_5	N/A	0.714	0.92	0.689	N/A	N/A	N/A

3.4.3.2 Validation for the mixed mode uniform field cyclic loading

We consider an eight-node hexahedral macroscopic element for woven composite RVE subjected to a mixed-mode (12 and 23) cyclic loading condition. The force-displacement relation at a single node as well as the overall transverse shear stress-strain relation are shown in Figure 3.13. Similar to the fibrous composite, pROH fails to reproduce the reference solution. The dpROH v1 performs relatively better than for the fibrous composite RVE because of the dominance of the two tows in the overall RVE behavior.

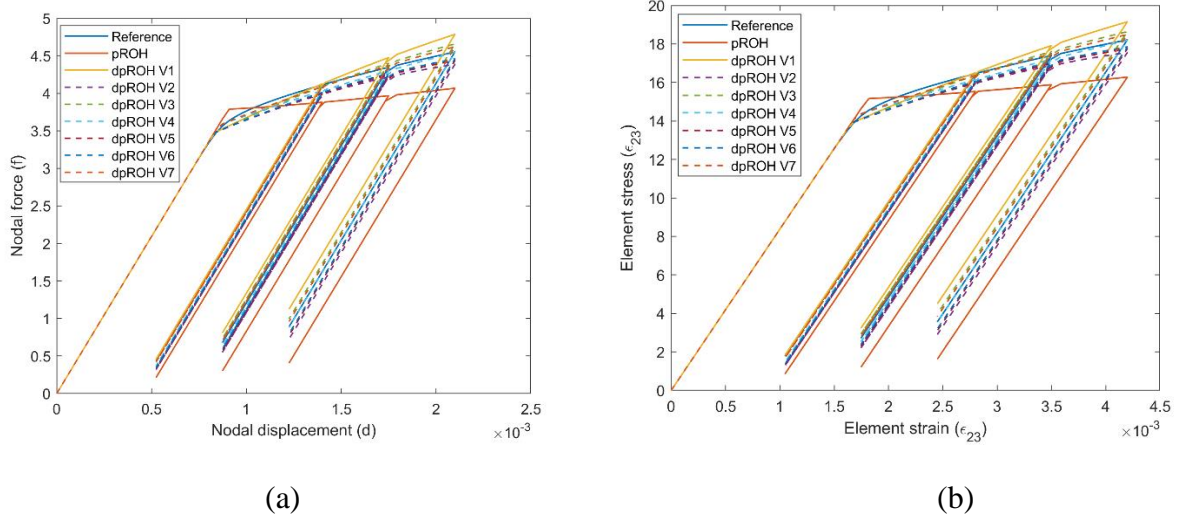


Figure 3.11. Mixed mode uniform field cyclic loading - (a) force-displacement relation, (b) macroscopic transverse shear stress-strain relation.

3.4.2.3 Validation on open hole quasi-isotropic plate

We now consider a quasi-isotropic plate with a hole subjected to an axial tension, shear and three-point bending. The plate dimensions are as follows: thickness 0.545, width 24, length 96, radius of the hole 4. For the three-point bending, we consider a shorter plate of length of 48 due to the reduced thickness. The laminate layup from the top to the bottom is: 0/90, -45/+45, -45/+45, 0/90. The plate consists of 2960 eight-node hexahedral macroscopic elements. The normalized accumulated errors in stress over the loading history as defined in the previous section for the three tests are summarized in Table 3.14, 3.15, 3.16.

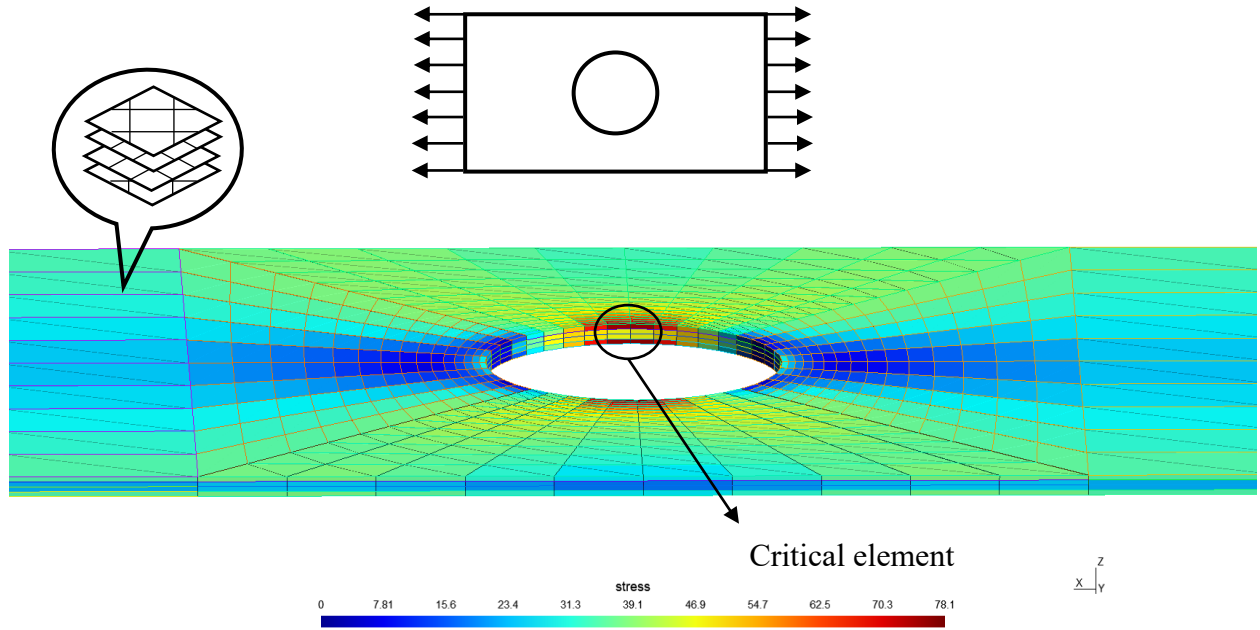


Figure 3.12. FOCH solution for the von the Mises stress distribution in the quasi-isotropic plate (woven composite microstructure) subjected to axial tension. Boundary conditions, laminate orientations, and location of the critical element are shown.

Table 3.14. Critical element error. Woven composite. Axial tension test

Variant of ROH	Homogenized	Matrix	Tow 1	Tow 2
pROH	5.3687	12.6461	9.0397	12.4688
dpROH(θ^{MCM})	1.2759	11.5805	7.5147	9.1913
dpROH($\theta^{MCM} + \theta^{ETT}$)	0.4017	9.6833	6.3841	7.4819
dpROH($\theta^{MCM} \rightarrow \theta^{ETT}$)	0.369	9.7472	6.3544	7.4425
dpROH($\theta^{ETT} \rightarrow \theta^{MCM}$)	0.4089	8.1056	5.9123	6.7341
dpROH($\theta^{MCM} + \theta_{comp}^{ETT}$)	0.5128	8.4886	5.8671	6.9272
dpROH($\theta^{MCM} \rightarrow \theta_{comp}^{ETT}$)	0.4611	9.6994	5.8112	6.8066
dpROH($\theta_{comp}^{ETT} \rightarrow \theta^{MCM}$)	0.294	6.5309	5.3225	6.123

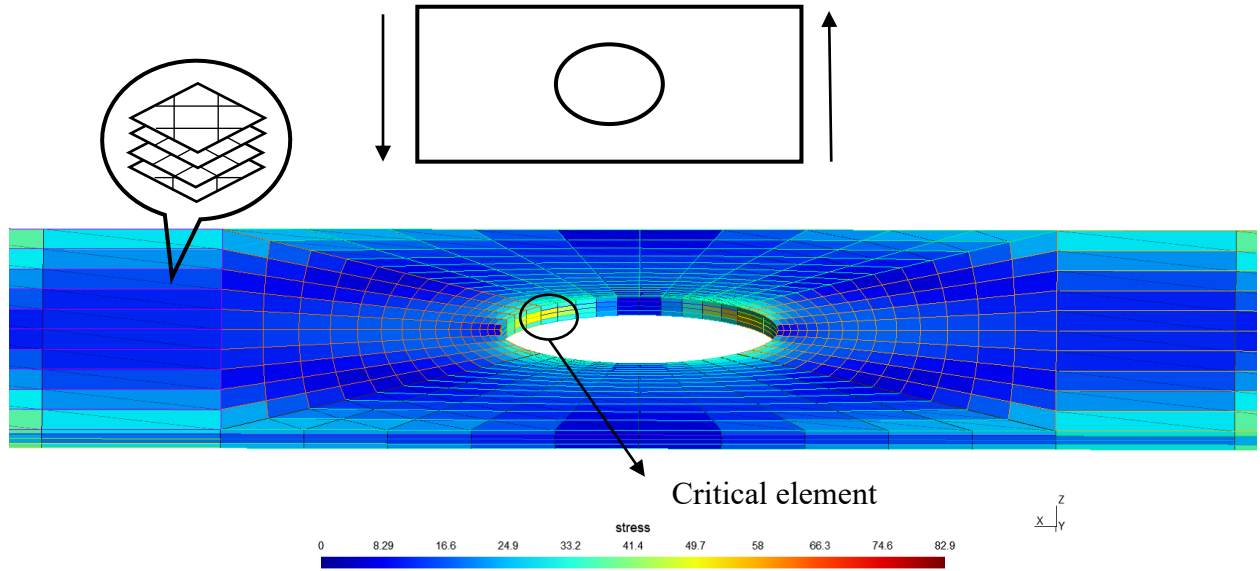


Figure 3.13. FOCH solution for the von Mises stress distribution in the quasi-isotropic plate (woven composite microstructure) subjected to in plane shear. Boundary conditions, laminate orientations, and location of the critical element are shown.

Table 3.15. Critical element error. Woven composite. In plane shear test

Variant of ROH	Homogenized	Matrix	Tow 1	Tow 2
pROH	6.4108	12.5179	9.8195	10.9877
dpROH(θ^{MCM})	1.8802	11.7765	7.4422	8.3889
dpROH($\theta^{MCM} + \theta^{ETT}$)	0.4506	8.4622	5.8738	6.5642
dpROH($\theta^{MCM} \rightarrow \theta^{ETT}$)	0.48	8.4512	5.857	6.5523
dpROH($\theta^{ETT} \rightarrow \theta^{MCM}$)	0.6429	6.1909	4.9181	5.5943
dpROH($\theta^{MCM} + \theta_{comp}^{ETT}$)	0.605	6.9911	5.3944	5.9083
dpROH($\theta^{MCM} \rightarrow \theta_{comp}^{ETT}$)	0.5365	7.3228	5.3238	5.8403
dpROH($\theta_{comp}^{ETT} \rightarrow \theta^{MCM}$)	0.3437	6.4955	4.5192	4.9691

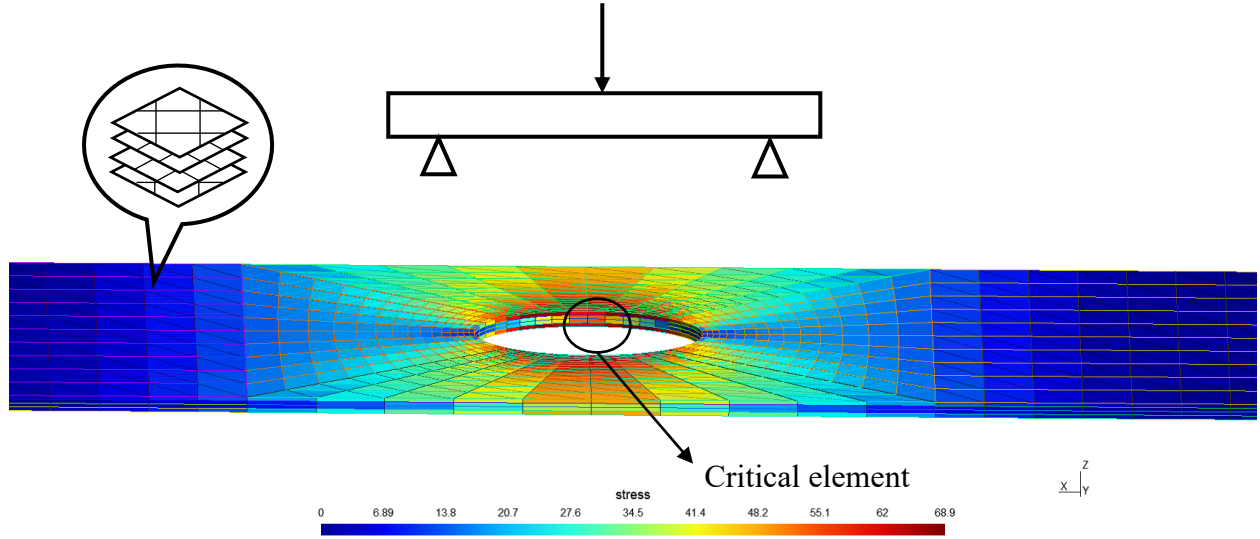


Figure 3.14. FOCH solution for the von Mises stress distribution in the quasi-isotropic plate (woven composite microstructure) subjected to three-point bending. Boundary conditions, laminate orientations, and location of the critical element are shown.

Table 3.16. Critical element error. Fibrous composite. Three-point bending test

Variant of ROH	Homogenized	Matrix	Tow 1	Tow 1
pROH	8.782	8.8859	9.6618	12.0625
dpROH(θ^{MCM})	2.2954	3.4368	4.8899	5.8071
dpROH($\theta^{MCM} + \theta^{ETT}$)	0.6063	2.353	4.2155	3.5777
dpROH($\theta^{MCM} \rightarrow \theta^{ETT}$)	0.5938	2.3027	4.226	3.4897
dpROH($\theta^{ETT} \rightarrow \theta^{MCM}$)	1.296	2.2496	4.0298	3.1626
dpROH($\theta^{MCM} + \theta_{comp}^{ETT}$)	0.8674	2.5639	4.3435	3.1957
dpROH($\theta^{MCM} \rightarrow \theta_{comp}^{ETT}$)	0.9572	2.606	4.2811	3.0249
dpROH($\theta_{comp}^{ETT} \rightarrow \theta^{MCM}$)	1.2851	2.4619	4.0821	2.7605

3.4.4 Computational time

Table 3.17 summarizes the computational time of the FOCH and various ROH variants for the plate with a hole under three-point bending. All calculations were performed using the Intel Xeon CPU E5-2699 v4 CPU. It can be seen that for all dpROH variants, most of the time is spent on offline computation. This is not surprising since the macroscopic problem is relatively small. In

case of say, one million degrees-of freedom problem, the CPU time of solving macroscopic problem would increase by a factor of roughly 100k ($1.8 < k < 2.5$ for sparse direct solvers) whereas the CPU time of the offline stage will remain constant and ultimately negligible to the computations at the online stage.

Table 3.17. Computational time for the FOCH and various ROH variants

Variant of ROH	Offline	Online
FOCH	N/A	22.89 h
pROH	N/A	0.171 h
$\text{dpROH}(\theta^{MCM})$	Dataset generation: 0.6 h RNN training: 0.83 h BI: 1.8 h	0.163 h
$\text{dpROH}(\theta^{MCM} + \theta^{ETT})$	Dataset generation: 0.6 h RNN training: 1.48 h BI: 4 h	0.149 h
$\text{dpROH}(\theta^{MCM} \rightarrow \theta^{ETT})$	Dataset generation: 0.6 h RNN training: 1.27 h BI: 2.56 h	0.202 h
$\text{dpROH}(\theta^{ETT} \rightarrow \theta^{MCM})$	Dataset generation: 0.6 h RNN training: 1.37 h BI: 2.42 h	0.197 h
$\text{dpROH}(\theta^{MCM} + \theta_{comp}^{ETT})$	Dataset generation: 0.6 h RNN training: 1.36 h BI: 2.69 h	0.156 h
$\text{dpROH}(\theta^{MCM} \rightarrow \theta_{comp}^{ETT})$	Dataset generation: 0.6 h RNN training: 1.13 h BI: 2.18 h	0.136 h
$\text{dpROH}(\theta_{comp}^{ETT} \rightarrow \theta^{MCM})$	Dataset generation: 0.6 h RNN training: 1.23 h BI: 2.07 h	0.158 h

3.5 Conclusion

A hybrid data-physics driven reduced-order homogenization (dpROH) approach that improves the accuracy of the physics-based reduced order homogenization (pROH) approach, but retains its unique characteristics, such as interpretability and extrapolation, has been developed. The dpROH

consist of the offline and online stages. In the offline stage, an enhanced model reduction strategy based on the Bayesian Inference (BI) that employs the Gated Recurrent Unit (GRU) neural network surrogate is developed. In the online stage, the dpROH (rather than the GRU surrogate employed in the BI process) is utilized for the component level predictions. Based on the numerical experiments comparing pROH and various variants of dpROH with the reference solution based on the first order computational homogenization (i.e., without model reduction) we make the following observations:

- The dpROH has been demonstrated to improve the accuracy of the physics-based model reduction for variety of test problems outside the training set.
- Among various dpROH variants sequential inference approaches incorporating compatibility constraint offer the lowest computational cost and comparable accuracy to the dpROH variants based on the simultaneous parameter training with and without compatibility constraint enforced.
- A weak coupling between the mean value of predicted constitutive model parameters of microphases and the eigenstrain transformation tensor parameters that governs model reduction have been observed. This indirect observation stems from the fact that the quality of predictions has been found to be little sensitive to how the two parameter sets, $\bar{\theta}^{ETT}$, $\bar{\theta}^{MCM}$, are inferred. This raises the possibility that an improved physics-based model reduction may exist.

Future work will focus on

- (i) development of improved physics-based model reduction guided by the observations found herein

- (ii) Study the dpROH in the context of various constitutive models of microphases, such as damage and combination of plasticity and damage
- (iii) Extension of the dpROH to more than two scales.

Chapter 4

Data-physics Driven Reduced Order Homogenization for Continuum Damage Mechanics at Multiple Scales

4.1 Introduction

Multiscale damage modeling is a concept used in materials science and engineering to understand the brittle behavior of heterogeneous materials at different scales. It involves studying the deformation and fracture of composite materials ranging from the microscopic to the macroscopic level. The multiscale approach is necessary because the properties of composite materials are influenced by various physical phenomena taking place at different scales. A multiscale damage model aims to incorporate the heterogeneity and microstructural features of its constituents, providing an accurate representation of their mechanical response and failure characteristics.

The application of multiscale damage modeling has been hindered by two primary challenges. The first arises from the nature of multiscale modeling itself. Computational homogenization-like multiscale methods demand significant computational resources. Due to the tremendous computational complexity in multiscale modeling, alternative approaches, such as various reduced order multiscale methods or data-driven methods have been devised. For a detailed description of these methods, including those that are based on physics, data, or a combination of both, the reader is referred to the review articles [39, 84] among many others.

Secondly, models that describe damage and strain softening in a continuous manner are prone to unstable numerical solutions due to the underlying ill-posed partial differential equation [85]. Consequently, finite element simulations based on such models often exhibit mesh sensitivity, whereby the damage zone is confined to a single element, leading to a lack of convergence in the

simulation as damage initiates. To address these issues, various regularization techniques have been proposed, such as nonlocal methods [86, 87], gradient-enhanced nonlocal methods [89, 90], viscous regularization methods [90], phase field methods [91], and adaptive mesh refinement [92]. While these methods have been mostly proven in the context of single-scale damage modeling, their viability has been questioned in the context of multiple scales [93]. As pointed out by Bazant [93], the two challenges are contradictory in nature, i.e., the higher resolution provided by multiscale methods may have an opposite effect to the regularization methods that attempt to smear out the fine-scale behavior.

There have been several noteworthy contributions in multiscale damage modeling. Oskay [31] extended a physics-based reduced order homogenization (pROH) to continuum damage mechanics at multiple length scales based on the transformation field analysis (TFA) [94]. By this approach, a characteristic length scale is introduced by controlling an approximation order of eigenstrains. Wu [95] combined the mean field homogenization with the gradient-enhanced approach to account for damage evolution in a two-phase fiber-reinforced composite. Ghosh [97, 98] introduced a characteristic length scale by combining an asymptotic homogenization method with micromechanical Voronoi cell finite element method (VCFEM). Other noteworthy contributions in homogenization-like multiscale damage methods can be found in [98, 99, 100] among many other contributions.

In the area of data-driven methods for continuum damage mechanics, Deng [101] and Logarzo [109] proposed a physics-informed data-driven deep learning model as an efficient surrogate to emulate an effective response of a heterogeneous elasto-plastic softening material. However, neural networks employed in these works are known to encounter limited predictive capacity, overfitting, and underfitting. Merely increasing the number of input parameters may not

necessarily resolve these issues, as it necessitates an exponential increase in the amount of available data points. Other data-driven multiscale approaches have been proposed [66, 69, 70], but few of them are applicable to simulate damage taking place at multiple length scales.

The present work attempts to meet the challenge posed by Bazant [93] by extending the data-physics driven reduced order homogenization (dpROH) [84] to multiscale damage modeling. The proposed method aims at alleviating the potential pitfalls of either data-driven or physics-based reduced order methods [30, 32, 33, 34]. The dpROH employs a surrogate-based Bayesian Inference engine to estimate the eigenstrain transformation tensor to reproduce a reference solution (physical experiment or direct numerical simulation (DNS) with an embedded characteristic length scale) at a coupon level. The proposed formulation has been validated at a subcomponent level against the DNS with an embedded characteristic length scale based on the nonlocal damage formulation [104].

The outline of this subsection is as follows. Section 4.2.1 provides a brief review of the physics-based reduced order homogenization (pROH) for the continuum damage model. The Bazant's nonlocal continuum damage approach and its multiple scale variant are described in Section 4.2.2. Details of the proposed dpROH for multiscale damage modeling are given in Section 4.3. Numerical studies on the accuracy and efficiency of dpROH are described in Section 4.4. Summary and conclusions are given in Section 4.5.

4.2 Methodology

In this section, we present the data-physics driven reduced order homogenization (dpROH) for continuum damage mechanics at two length scales starting with the review of the physics-driven

reduced order homogenization followed by Bazant's nonlocal damage approach and its multiscale variant.

4.2.1 Review of the physics driven Reduced Order Homogenization (pROH)

As a brief overview of the physics driven reduced order homogenization, we start by defining governing equations over a representative volume element (RVE) domain with isotropic damage model.

$$\sigma_{ij,y_j}^f = 0 \quad (4.1a)$$

$$\varepsilon_{kl}^f(\mathbf{x}, \mathbf{y}) = \varepsilon_{kl}^c(\mathbf{x}) + u_{(k,y_l)}^*(\mathbf{x}, \mathbf{y}) \quad (4.1b)$$

$$\varepsilon_{kl}^c(\mathbf{x}) = u_{(k,x_l)}^c \quad (4.1c)$$

$$\varepsilon_{kl}^*(\mathbf{x}, \mathbf{y}) = u_{(k,y_l)}^*(\mathbf{x}, \mathbf{y}) \quad (4.1d)$$

$$\sigma_{ij}^f(\mathbf{x}, \mathbf{y}) = L_{ijkl}^f(\mathbf{y}) \left(\varepsilon_{kl}^f(\mathbf{x}, \mathbf{y}) - \mu_{kl}^f(\mathbf{x}, \mathbf{y}) \right) \quad (4.1e)$$

$$\mu_{kl}^f(\mathbf{x}, \mathbf{y}) = \omega^f(\mathbf{x}, \mathbf{y}) \varepsilon_{kl}^f(\mathbf{x}, \mathbf{y}) \quad (4.1f)$$

The focus of this study is limited to quasi-brittle materials, where damage is assumed to be isotropic. A single scalar quantity, ω , is used to describe the damage initiation and evolution process. The undamaged state is represented by $\omega = 0$, while $\omega = 1$ represents complete damage. In the present study we adopt Mazar's damage model [107], in which the local damage function is expressed as:

$$\omega^f = \begin{cases} 1 - \frac{\kappa^0}{\kappa} (1 - \alpha + \alpha \exp(-\beta(\kappa - \kappa^0))) & \text{if } \kappa \geq \kappa^0 \\ 0 & \text{if } \kappa < \kappa^0 \end{cases} \quad (4.2)$$

Where κ is an internal state variable; κ^0 , α , β are material constants denoting damage threshold, final damaged state, and damage evolution rate. With the above definitions, the corresponding Kuhn-Tucker condition is expressed as:

$$f(\epsilon, \kappa) \leq 0, \quad \dot{\kappa} \geq 0, \quad f(\epsilon, \kappa) \dot{\kappa} = 0, \quad \text{where} \quad f(\epsilon, \kappa) = \epsilon^{eq} - \kappa \quad (4.3)$$

where ϵ^{eq} denotes the equivalent strain. In this work, we employ a modified Von Mises [107, 108] as an equivalent strain. It is expressed as:

$$\epsilon_{eq} = \frac{\gamma-1}{2\gamma(1-2\nu)} I_1 + \frac{1}{2\gamma} \sqrt{\left(\frac{\gamma-1}{2\gamma(1-2\nu)} I_1\right)^2 + \frac{12\gamma}{(1+\nu)^2} J_2} \quad (4.4)$$

$$I_1 = \epsilon_{11} + \epsilon_{22} + \epsilon_{33}$$

$$J_2 = \frac{1}{3} (\epsilon_{11}^2 + \epsilon_{22}^2 + \epsilon_{33}^2 - \epsilon_{11}\epsilon_{22} - \epsilon_{22}\epsilon_{33} - \epsilon_{33}\epsilon_{11} + 3(\epsilon_{12}^2 + \epsilon_{23}^2 + \epsilon_{13}^2))$$

with γ denoting the ratio of tensile and compressive strength, ν poisson's ratio and I_1 , J_2 strain invariants.

4.2.2 Nonlocal continuum damage mechanics model

We start with a brief overview of the classical nonlocal damage theory originated by Bazant [86], which produces a well-posed mathematical model.

The nonlocal integral-type model defines a weighted average of a damage variable in a spatial neighborhood Ω_c . The nonlocal damage variable $\hat{\omega}$ is defined as

$$\begin{aligned} \hat{\omega}(x^i) &= \frac{\int_{\Omega_c} \alpha(x^i, x) \omega(x) d\Omega_c}{\int_{\Omega_c} \alpha(x^i, x) d\Omega_c} \\ &\approx \sum_{j=1}^{N_{gp}} \frac{\alpha(x^i, x^j)}{\sum_{j=1}^{N_{gp}} \alpha(x^i, x^j)} w(x^j) \end{aligned} \quad (4.5)$$

The weight function, denoted by α , can take the form of either a bell-shaped or Gaussian function.

The variable x^i represents the coordinates of specific Gauss point being considered, while j represents its neighboring Gauss points located within a characteristic length l_c from the point i .

A typical bell-shaped weight function has the following form:

$$\alpha(x^i, x^j) = \frac{1}{(1 + (\frac{\|x^i - x^j\|}{l_c})^a)^b} \quad (4.6)$$

where $\| \cdot \|$ denotes the L_2 norm; a and b are material constants which control the shape of the weight function; l_c is a characteristic length that represents the size of the nonlocal region.

We now consider a nonlocal variant of the pROH. The discretized residual derived from Eq. (3.6), can be expressed in matrix form as follows:

$$\mathbf{r}^{(\beta)} = \Delta \epsilon^{(\beta)} - \sum_{\gamma=1}^M \mathbf{P}^{(\beta\gamma)} \Delta \boldsymbol{\mu}^{(\gamma)} - \mathbf{E}^{(\beta)} \Delta \epsilon^c \quad (4.7)$$

where nonlocal eigenstrain increment is defined

$$\Delta \hat{\boldsymbol{\mu}}^{(\alpha)} = \Delta \hat{\omega}^{(\alpha)} \boldsymbol{\epsilon}^{(\alpha)} \quad (4.8)$$

The nonlocal damage parameter in phase α , $\hat{\omega}^{(\alpha)}$, is computed by averaging the same phase damage parameters over the characteristic neighborhood Ω_c (4.5).

For stress update procedures and consistent tangent, we refer to [34].

4.3 dpROH framework for continuum damage mechanics

4.3.1 Reference and training dataset generation

The primary objective of this section is to utilize dpROH framework for modeling continuum damage mechanics of heterogeneous materials. The novelty of the present study compared to conventional multiscale damage methods is as follows:

- (i) It is mesh size independent at the model identification and component level stages
- (ii) Its model parameters can be inferred from a limited reference (experiment or direct numerical simulation (DNS)) data using Bayesian Inference
- (iii) It exhibits high computational efficiency compared to other nonlocal multiscale damage methods
- (iv) It produces interpretable material responses at both the macroscopic and microscopic scales.

The first stage of our research involves carrying out uniform field physical experiments. In the present study, instead of conducting physical experiments, a high-fidelity DNS with periodic boundary conditions is simulated to mimic physical experiments at the RVE level. This model is trained to resolve microstructural details to produce accurate data at the RVE level with no more than six monotonic loading tests, corresponding to six distinct strain or stress components. These components are denoted as the 11, 22, 33, 23, 13, and 12 deformation modes. The number of independent deformation modes may be further reduced based on the geometry of the RVE (see Figure 4.3 step 1).

Given the reference data, we can generate a training dataset using physics-based Reduced Order Homogenization (pROH). The process involves conducting numerous RVE simulations, using pROH, under different loading conditions, and by varying constitutive law parameters θ^d and

eigenstrain transformation tensor parameters θ^{ETT} . The purpose of inferring constitutive law parameters is to identify the difference between the manufacturer's specified and the actual properties. Meanwhile, the inference of the eigenstrain transformation tensor accounts for the approximation error in model reduction. The iterative process involves numerous simulations that collect history data (denoted to be a function of pseudo time t) of the coarse-scale strain $\epsilon^c(t)$ and stress $\sigma^c(t)$ at each load increment for various model parameters, (θ^d, θ^{ETT}) . This is schematically depicted in Fig. 4.1.

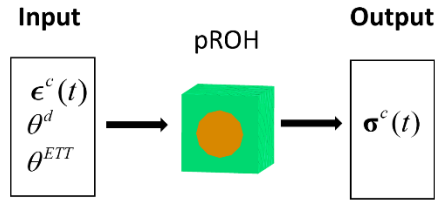


Figure 4.1. Dataset generation configuration with pROH

4.3.2 Surrogate-based Bayesian Inference on softening material behavior

The primary objective of the trained surrogate model is to expedite the Bayesian Inference (BI) process, which typically involves performing numerous forward simulations. However, performing high-dimensional parameter inference using DNS is computationally challenging. An alternative approach is to replace the forward simulations with a surrogate model. The number of simulations necessary to train a reliable surrogate model is typically less than the number of simulations required for the Monte Carlo Markov Chain (MCMC) process [85].

In the application of the BI, there are several viable options for developing surrogate models. Some popular choices include Gaussian Process Regression (GPR), Support Vector Regression (SVR), and Neural Networks. When dealing with the history-dependent data, Recurrent Neural Networks

(RNN) is a preferred choice, designed specifically for sequential data analysis. However, RNNs rely on the quality of the training dataset to achieve accurate surrogate models. When dealing with a three-dimensional RVEs, it is challenging to sample various deformation paths, particularly for irreversible softening deformation. The salient feature of the proposed approach is that it does not require sampling of all deformation paths, but rather infers the eigenstrain transformation tensor parameters through monotonic loading paths, which has been found to be sufficient for BI. This leads to a significant reduction in the sampling space and dataset size without sacrificing the accuracy of the trained RNN outside the monotonic loading space.

Using created training dataset, each simulation is denoted herein as $S_i = \{\epsilon_i^c(t), \theta_i^d, \theta^{ETT}, \sigma_i^c(t)\}$, where i represents simulation index, $i \in [1, n]$. The Gated Recurrent Unit (GRU) has been extensively utilized in the development of surrogate models for path-dependent materials. The key advantage of employing GRU lies in its reduced number of hyperparameters compared to other RNN structures. The architectural representation of the GRU employed in this study is depicted in Fig. 4.2 The inputs are the coarse-scale strain $\epsilon^c(t) = \{\epsilon_{11}^c, \epsilon_{22}^c, \epsilon_{33}^c, \epsilon_{23}^c, \epsilon_{13}^c, \epsilon_{12}^c\}$ combined with the model parameter θ^d and θ^{ETT} . The outputs are the corresponding stress $\sigma^c(t) = \{\sigma_{11}^c, \sigma_{22}^c, \sigma_{33}^c, \sigma_{23}^c, \sigma_{13}^c, \sigma_{12}^c\}$. For details on the GRU cell, we refer to [85]. Various approaches have been proposed to incorporate history dependent and independent data within the GRU architecture [67]. An effective technique involves extending the history-independent data and matching the dimensions of the pseudo time step size (load increments), which has been demonstrated to yield improved results. The implementation of such a GRU architecture using the Keras library [39] is provided in numerical example section. Utilizing the trained Gated Recurrent Unit (GRU), we have successfully acquired all components of the surrogate-based Bayesian Inference engine [85].

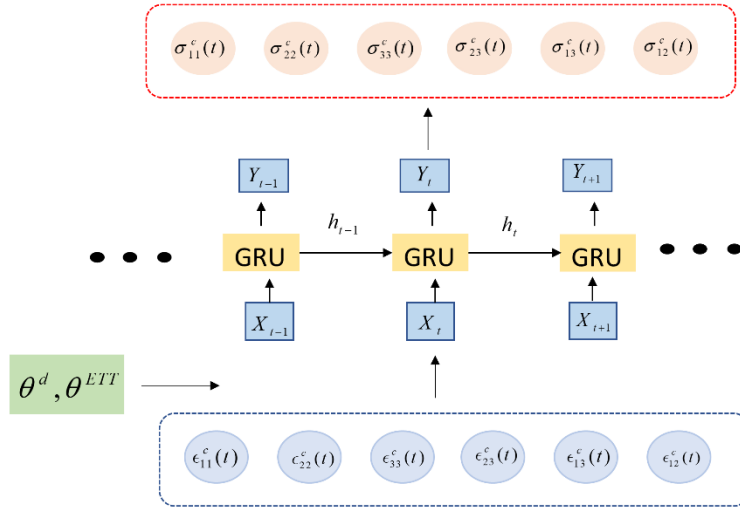


Figure 4.2 Architecture of the GRU in the dpROH. X_t and Y_t represent inputs and outputs at a pseudo time step t respectively

4.3.3 Framework summary

The multiscale damage framework based on the variant of the dpROH is detailed below:

Offline stage:

1. Perform DNS at the RVE level incorporating the nonlocal damage model to generate homogenized stress-strain reference data.

2. Train the neural network-based surrogate model using the Gated Recurrent Unit (GRU)

architecture utilizing the training dataset $\sum_{i=1}^n S_i = \{\epsilon_i^c(t), \theta_i^d, \theta^{ETT}, \sigma_i^c(t)\}$.

3. Apply the GRU-based Bayesian Inference (GRU-BI) method to the reference data obtained from Step 1, yielding either probability density functions ($P(\theta^d)$, $P(\theta^{ETT})$) or its deterministic mean values ($\bar{\theta}^d$, $\bar{\theta}^{ETT}$).

Online stage:

Utilize the dpROH-based two-scale solver to make predictions at the component level.

The dpROH flowchart is given in Fig. 4.3.

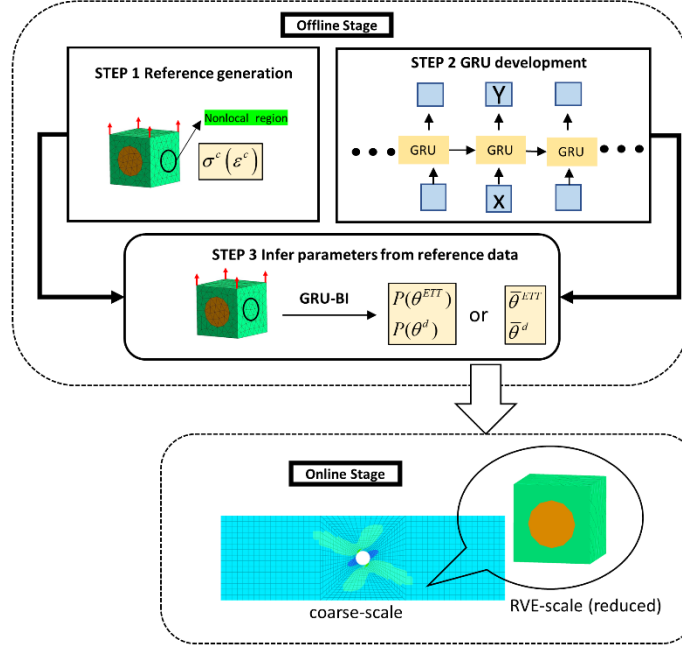


Figure 4.3. Flowchart of the dpROH for multiscale damage modeling

4.4 Numerical Examples

4.4.1 Reference solution based on nonlocal DNS model

We consider a fibrous composite RVE depicted in Fig. 4. The RVE, comprised two distinct phases has been discretized using 1558 eight-node hexahedral elements. The fiber volume fraction is 24.56%. The matrix is modeled using isotropic damage model, while the fiber is assumed to remain elastic. The material constants for the reference solution are summarized in Table 4.1.

Table 4.1. Reference material properties

	Matrix (Isotropic damage)	Inclusion or fiber (Elasticity)
Young's Modulus	2500 Mpa	125000 Mpa
Poisson's ration	0.32	0.01
k_0	0.0001	N/A
α	0.85	N/A
β	250	N/A

The reference solution is based on the nonlocal DNS. The characteristic length in Equation (12) is chosen as 0.48. Figure 5(a) depicts the reference DNS solution subjected to periodic boundary conditions resulting in material behavior that is independent of the mesh size. Having obtained the reference data, subsequent steps involve generating a corresponding training dataset. For each deformation mode, we perform 20,000 simulations employing pROH with 100 load increments. The range of damage parameters is given in Table 2. In the subsequent numerical examples, we denote the dpROH that solely considers the damage parameters as dpROH v1. A variant dpROH v2 employs both the constitutive model parameters as well as the eigenstrain transformation tensor parameters denoted as $\theta^{ETT} = \{\alpha_I\}$, which rescale specific terms in $P_{ij}^{kl(\beta\alpha)}$. Although the complete $P_{ij}^{kl(\beta\alpha)}$ comprises of 36 terms, its independent terms can be reduced to six (see Table 4.3) due to their symmetric and diagonal-dominated nature [85]. The range of rescaling parameters are specified as $\alpha_I = [0.8, 1.2]$.

Table 4.2. microstructural damage parameters range for fibrous RVE

θ^d	k_0	α	β
Ranges	[0.00007~0.00013]	[0.5~0.99]	[100~800]

Table 4.3. Independent terms $P_{ij}^{kl(\beta\alpha)}$ for fibrous RVE

Fibrous composite RVE	
Rescaling parameters	Transformation tensor components
α_1	$P_{11}^{11(11)}, P_{22}^{22(11)}$
α_2	$P_{23}^{23(11)}, P_{13}^{13(11)}$
α_3	$P_{12}^{12(11)}$
α_4	$P_{11}^{11(21)}, P_{22}^{22(21)}$
α_5	$P_{23}^{23(21)}, P_{13}^{13(21)}$
α_6	$P_{12}^{12(21)}$

The architecture of the surrogate neural network comprises of a single GRU layer with a rectified linear unit (ReLU) activation function, succeeded by two dense layers. The last layer is a "TimeDistributed" layer, enabling the application of the designated dense layer to each time step individually. The output activation function is linear. Notably, all layers within this network configuration consist of 64 units.

With the surrogate model, we now apply the GRU-BI to the three sets of DNS data to infer model parameters. The BI results are given in Fig. 4.5. The results of the dpROH v1 and dpROH v2 are compared to DNS in Fig 4.6. (b)(c)(d). The results obtained from pROH without calibration are included for comparison. For the matrix-dominated deformations (11, 23, 12), it is evident that pROH exhibits a noticeably stiffer post-damage behavior due to the approximation introduced in model reduction. However, these discrepancies can be rectified by employing dpROH. In this specific scenario, both dpROH v1 and dpROH v2 exhibit minor errors, primarily influenced by the substantial nonlocal behavior. Due to the large characteristic length l_c , the matrix phase achieves a higher degree of uniformity, resulting in minimal discrepancies between dpROH v1 and dpROH v2 in the present example. Nonetheless, dpROH v2 is slightly more accurate

reproducing the desired outcomes and showcasing improved accuracy at a subcomponent level described in subsequent sections.

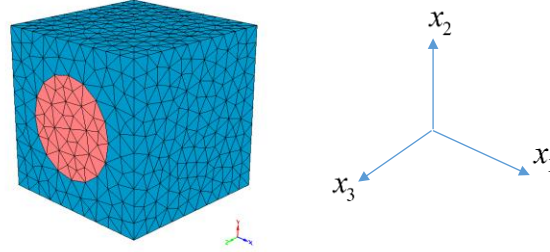


Figure 4.4. Fibrous RVE and material coordinate system considered in the present study.

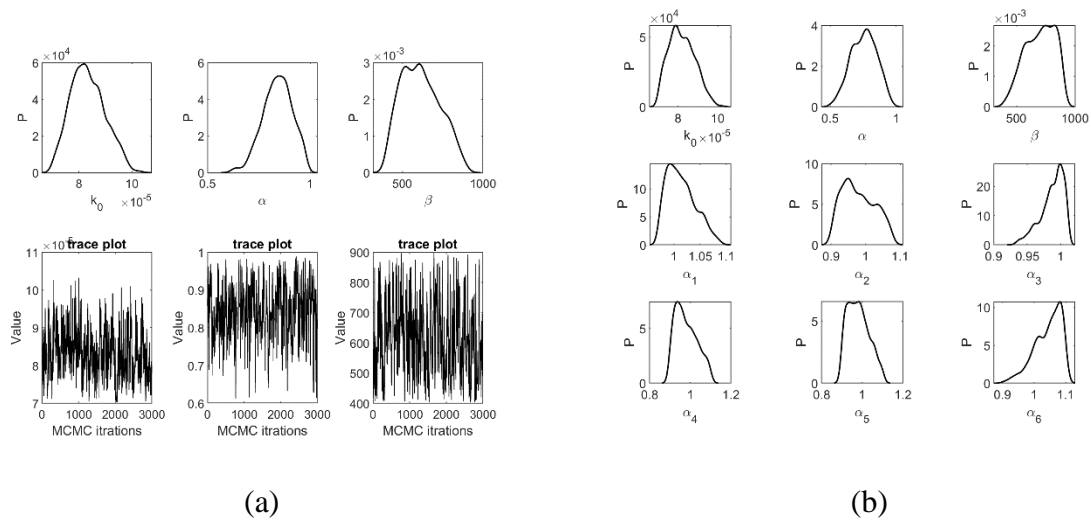
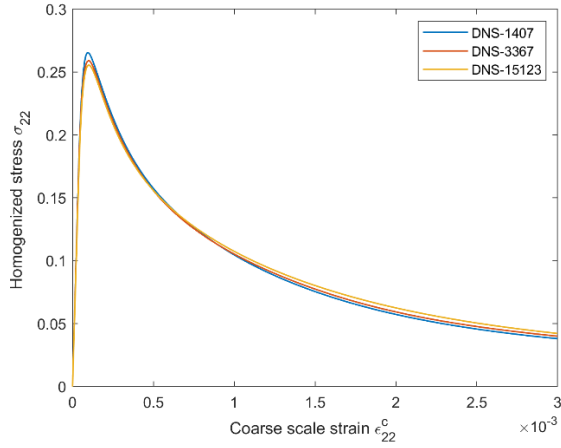
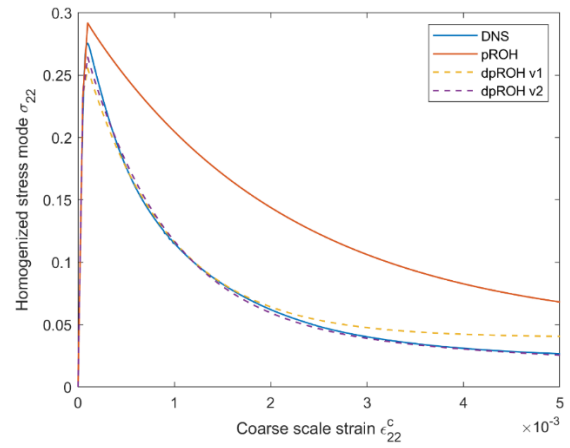


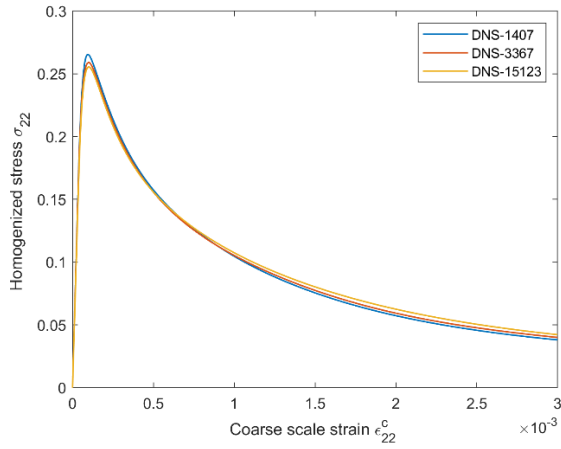
Figure 4.5. Bayesian Inference results (a) The first row represents the probability density functions of three damage parameters in dpROH v1. The second row refers to the corresponding MCMC trace plots. (b) probability density functions of θ^d and θ^{ETT} in dpROH v2.



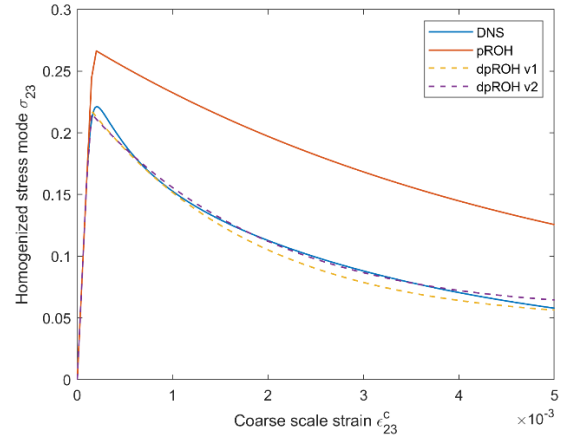
(a)



(b)



(c)



(d)

Figure 4.6. (a) mesh independent nonlocal DNS results, (b) transverse tension test mode 22, (c) simple shear mode 12 (d) simple shear 23. Results generated by pROH (red lines). Results generated by dpROH (dashed lines).

4.4.2 Validation for mixed mode cyclic loading

We consider a mixed mode cyclic loading test outside the training set. A single two-scale macroscopic element is subjected to mix-mode cyclic loading in modes 22 and 23, and the results are depicted in Fig. 4.7. It can be seen that both dpROH models are in good agreement with the DNS.

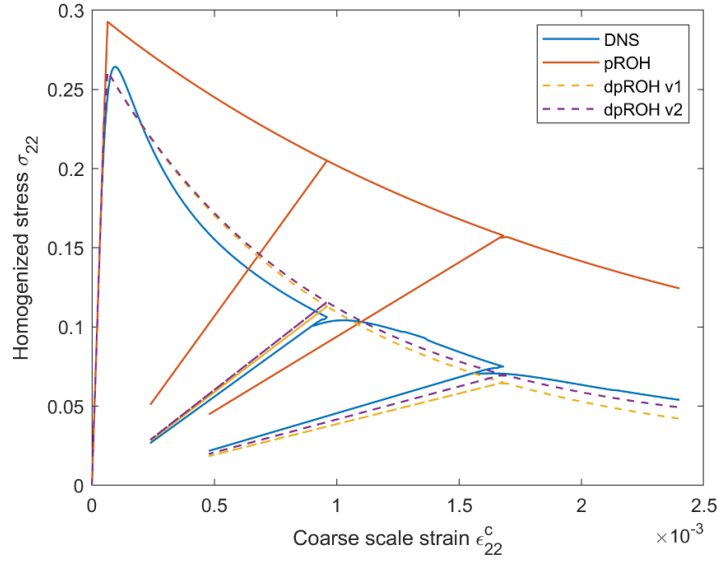


Figure 4.7. 22-component stress-strain of single element subjected to 22-23 mix-mode cyclic tensile loading

4.4.3 A perforated Plate validation problem

In this section, we evaluate the performance of dpROH in predicting subcomponent-level behavior. Specifically, we will conduct simulations on a plate with a hole subjected to tensile loadings. The dimensions of the plate are 18x18 mm, with a hole radius of 3 mm and a thickness of 1 mm. To discretize the plate with a hole, we utilize approximately 300 RVEs consisting of total 384,989 tetrahedral elements for the nonlocal DNS, which serves as a reference solution.

The results of the nonlocal DNS are compared to the dpROH v2 with either local or nonlocal damage formulations. We first compare the reference solution to the dpROH where the macro-mesh is coarse consisting of 300 elements and the damage model is local. The macroscopic element size essentially introduces a characteristic length, which is approximately equal to the RVE size in the DNS. We also consider a finer macroscopic mesh (616 macroscopic elements), but in this case nonlocal damage model as described in Section 2.2 is employed. The mesh configurations are shown in Fig. 4.8.

The force-displacement curves are presented in Fig. 4.9, demonstrate the performance of dpROH for the two meshes. It is observed that the dpROH with a coarse mesh, where the macroscopic element size is equal to the RVE size, yields satisfactory results. However, some discrepancies arise near the failure point due to mesh non-uniformity. This phenomenon is mitigated with a finer mesh employing nonlocal method.

This numerical example highlights the capability of dpROH to accurately predict the behavior of heterogeneous materials at the component level. Additionally, in terms of computation time, running the DNS requires approximately 40 hours of CPU time, whereas the combined offline and online stages for dpROH take 8 hours in total. It is worth noting that the current example consists only 324 RVEs for the DNS. In practical applications, the training and inference time of dpROH would be negligible compared to the computational time required for DNS.

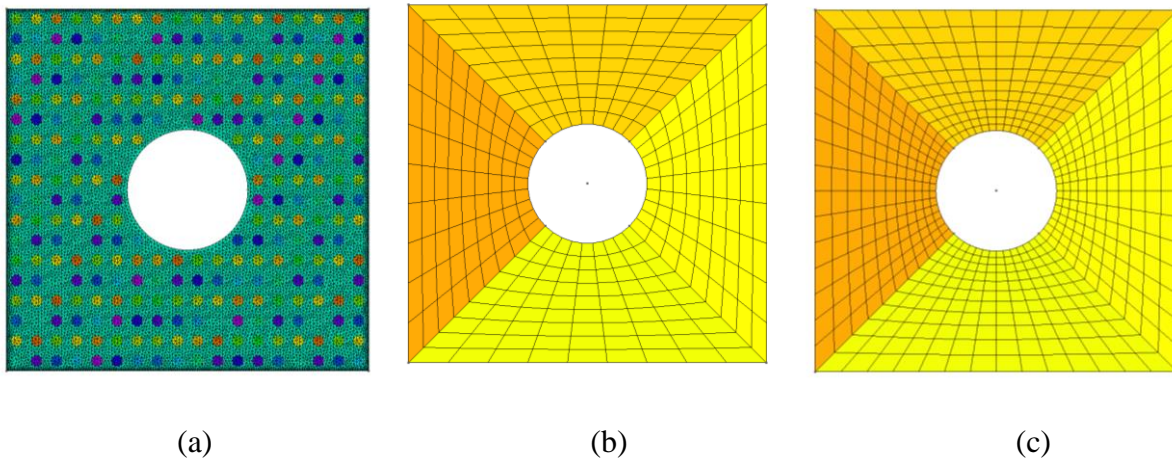


Figure 4.8. The finite element discretization of the perforated plate with fibrous microstructures. (a) Direct numerical simulation model consisting of 384,989 four-node tetrahedra elements. (b) dpROH model employing 324 eight-noded hexahedra elements for the macroscale domain (c) dpROH model with 616 eight-noded hexahedra elements for the macroscale domain.

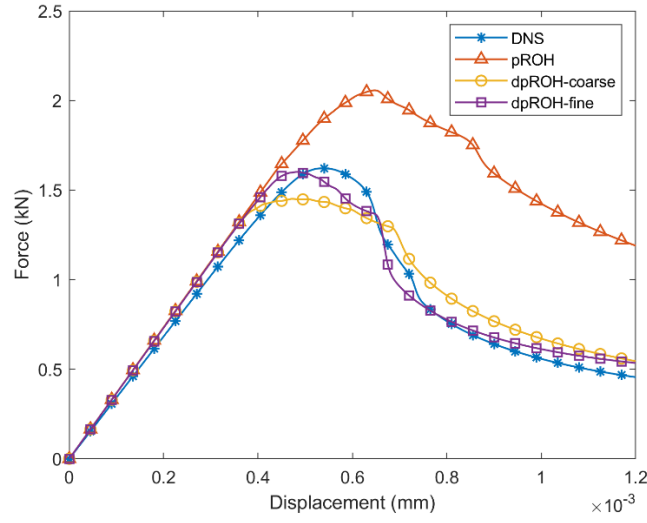


Figure 4.9. Force-displacement curves for the DNS, pROH, local dpROH (coarse mesh), nonlocal dpROH (finer mesh)

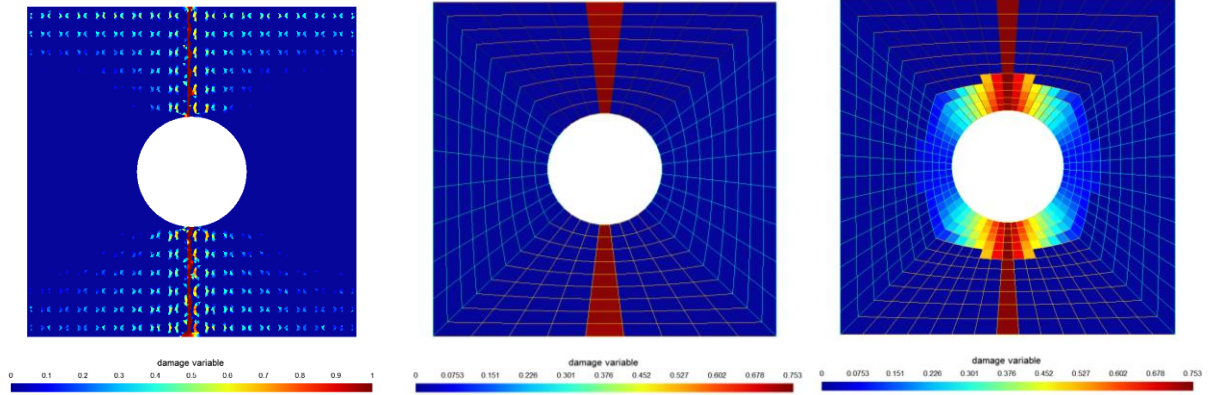


Figure 4.10. Damage plots for the DNS, local dpROH (coarse mesh), nonlocal dpROH (finer mesh)

In Fig. 4.10, we present the damage plots for the three variant. Note that the DNS damage plot presents data on an element-by-element basis, with the gaps representing fibers. Conversely, the damage variable in dpROH represents average values over the unit cell. It can be seen that our dpROH approach do predict correct damage evolution.

4.5 Conclusion

We developed a variant of the dpROH approach for continuum damage modeling at two scales. At the RVE level, the dpROH effectively reproduces phase damage evolution in comparison to the nonlocal DNS model. Likewise, at the component level, the nonlocal dpROH is in good agreement with the nonlocal DNS model. The model reduction is essential for computational efficiency of dpROH at the component level. Compared to the traditional DNS approach, dpROH offers notable advantages in terms of computational efficiency without compromising on accuracy. Overall, the dpROH method presented in this study demonstrates its effectiveness in accurately modeling heterogeneous materials at both the microscopic and macroscopic scales, offering a promising approach for multiscale damage analysis. The proposed method also offers a viable framework to enhance the interpretability when compared to other purely data-driven damage modeling methods.

Chapter 5

Conclusions

5.1 Contributions

We kick start this thesis by demonstrating the effectiveness of the pseudo-nonlocal finite element method within the context of linear hexahedral elements. Our findings reveal that this method achieves accuracy levels similar to those obtained with full integration, while significantly improving computational speed by approximately 8 times in multiscale material modeling. Through applications in FOCH, ROH, and dpROH, we observe that this method exhibits promising characteristics as an integration scheme for homogenization-like multiscale methods. Notably, its advantage over reduced integration methods lies in its elimination of the need for artificial stiffness, while still producing stiffer results that closely align with the outcomes of the full integration scheme.

Chapters 3 and 4 of this study provide empirical evidence for the effectiveness and versatility of data-physics driven reduced order homogenization through various numerical examples of heterogeneous material modeling. This data-enhanced model reduction technique utilizes limited data to extract a practical eigenstrain transformation tensor, which governs the evolution of eigenstrain within each material partition in RVE. The proposed framework significantly enhances the efficiency of simulating RVE equilibrium problems without compromising accuracy. The proposed method makes a significant contribution to the field of data-physics driven multiscale modeling by preserving the physical framework of model reduction while improving accuracy with data. It achieves this by avoiding the replacement of any components in the multiscale finite element algorithm with surrogate models. This preservation of the physical reduction model

framework ensures that the outcomes maintain their physical meaning when dealing with unseen deformation paths and macroscopic component geometries.

Furthermore, the method achieves the highest computational efficiency when focusing on resolving solutions at the microstructure partition level where we assume eigenstrain is a constant over a partition. By combining data inference to determine critical reduction parameters, the method strikes a balance between accuracy and efficiency, allowing for efficient simulations while maintaining the physical integrity of the results.

5.2 Future perspective

Considering two main topics, we list some future research directions as follows:

- The current implementation of the pseudo-nonlocal finite element method is limited to linear hexahedral elements. Further research is required to investigate its performance on higher order hexahedral elements. In this study, the focus was primarily on evaluating its computational efficiency and accuracy. However, future work should address its capability to solve locking problems associated with full integration elements or address any potential hourglass phenomena that may arise in reduced integration elements. These aspects remain important considerations for the development and improvement of the method in future investigations.
- The data-physics driven reduced order homogenization approach incorporates both material parameters and model parameters to enhance its performance. However, certain numerical examples have revealed a weakly coupled relationship between nonlinear material parameters and model reduction parameters. Specifically, the inferred nonlinear parameters predominantly account for the delayed eigen deformation, such as the yield

point in elasto-plasticity models or the failure point in continuum damage models. This delayed eigen deformation arises due to the assumption of constant eigenstrain over each material partition. Consequently, exploring alternative methods to solve the delayed eigen deformation may lead to the derivation of practical eigenstrain transformation tensors that are independent of material nonlinear parameters. This investigation could potentially provide valuable insights for future advancements in the field. Additionally, our research has explored the application of the data-physics driven reduced order homogenization approach in elasto-plasticity models and continuum damage models. However, the application of this approach to hybrid elasto-plasticity-damage models remains a challenge that requires further investigation.

References

1. Mackenzie-Helnwein P, Eberhardsteiner J, Mang HA. A multi-surface plasticity model for clear wood and its application to the finite element analysis of structural details. *Computational Mechanics*. 2003 May;31(1):204-18.
2. Karavelić E, Ibrahimbegovic A, Dolarević S. Multi-surface plasticity model for concrete with 3D hardening/softening failure modes for tension, compression and shear. *Computers & Structures*. 2019 Sep 1;221:74-90.
3. Reddi D, Areej VK, Keralavarma SM. Ductile failure simulations using a multi-surface coupled damage-plasticity model. *International Journal of Plasticity*. 2019 Jul 1;118:190-214.
4. Cuitino AM, Ortiz M. Computational modelling of single crystals. *Modelling and Simulation in Materials Science and Engineering*. 1993 Apr 1;1(3):225.
5. Yan H, Oskay C. Multi-yield surface modeling of viscoplastic materials. *International Journal for Multiscale Computational Engineering*. 2017;15(2).
6. Feyel F, Chaboche JL. FE2 multiscale approach for modelling the elastoviscoplastic behaviour of long fibre SiC/Ti composite materials. *Computer methods in applied mechanics and engineering*. 2000 Mar 17;183(3-4):309-30.
7. Sparks P, Oskay C. The method of failure paths for reduced-order computational homogenization. *International Journal for Multiscale Computational Engineering*. 2016;14(5).
8. Terada K, Hori M, Kyoya T, Kikuchi N. Simulation of the multi-scale convergence in computational homogenization approaches. *International Journal of Solids and Structures*. 2000 Apr 1;37(16):2285-311.
9. Ghosh S, Lee K, Moorthy S. Two scale analysis of heterogeneous elastic-plastic materials with asymptotic homogenization and Voronoi cell finite element model. *Computer methods in applied mechanics and engineering*. 1996 May 15;132(1-2):63-116.
10. Ghosh S, Dimiduk D, editors. *Computational methods for microstructure-property relationships*. New York: Springer; 2011.
11. Yuan Z, Fish J. Toward realization of computational homogenization in practice. *International Journal for Numerical Methods in Engineering*. 2008 Jan 15;73(3):361-80.
12. Mosby M, Matouš K. Computational homogenization at extreme scales. *Extreme Mechanics Letters*. 2016 Mar 1;6:68-74.
13. Ilic S, Hackl K, Gilbert R. Application of the multiscale FEM to the modeling of cancellous bone. *Biomechanics and modeling in mechanobiology*. 2010 Feb;9:87-102.

14. Dang TS, Wessels N, Nguyen NS, Hackl K, Meschke G. A coupled computational approach for the simulation of soil excavation and transport in earth-pressure balance shield machines. *International Journal for Multiscale Computational Engineering*. 2017;15(3).
15. Zohdi TI, Wriggers P. *An introduction to computational micromechanics*. Springer Science & Business Media; 2004 Nov 18.
16. Geers MG, Kouznetsova V, Brekelmans WA. Gradient-enhanced computational homogenization for the micro-macro scale transition. *Le Journal de Physique IV*. 2001 Sep 1;11(PR5):Pr5-145.
17. Ghosh S, Moorthy S. Elastic-plastic analysis of arbitrary heterogeneous materials with the Voronoi Cell finite element method[J]. *Computer Methods in Applied Mechanics and Engineering*, 1995, 121(1-4): 373-409.
18. Ghosh S. *Micromechanical analysis and multi-scale modeling using the Voronoi cell finite element method*[M]. CRC Press, 2011.
19. Moulinec H, Suquet P. A fast numerical method for computing the linear and nonlinear mechanical properties of composites[J]. *Comptes rendus de l'Académie des sciences. Série II. Mécanique, physique, chimie, astronomie*, 1994.
20. Moulinec H, Suquet P. A numerical method for computing the overall response of nonlinear composites with complex microstructure[J]. *Computer methods in applied mechanics and engineering*, 1998, 157(1-2): 69-94.
21. Chen J S, Wu C T, Yoon S, et al. A stabilized conforming nodal integration for Galerkin mesh-free methods[J]. *International journal for numerical methods in engineering*, 2001, 50(2): 435-466.
22. Paley M, Aboudi J. Micromechanical analysis of composites by the generalized cells model[J]. *Mechanics of materials*, 1992, 14(2): 127-139.
23. Aboudi J, Arnold S M, Bednarczyk B A. *Micromechanics of composite materials: a generalized multiscale analysis approach*[M]. Butterworth-Heinemann, 2013.
24. van Tuijl, R. A., Harnish, C., Matouš, K., Remmers, J. J., & Geers, M. G. (2019). Wavelet based reduced order models for microstructural analyses. *Computational Mechanics*, 63, 535-554.
25. Harnish C, Matous K, Livescu D. Adaptive wavelet algorithm for solving nonlinear initial–boundary value problems with error control[J]. *International Journal for Multiscale Computational Engineering*, 2018, 16(1).
26. Le B A, Yvonnet J, He Q C. Computational homogenization of nonlinear elastic materials using neural networks[J]. *International Journal for Numerical Methods in Engineering*, 2015, 104(12): 1061-1084.

27. Bhattacharjee S, Matouš K. A nonlinear manifold-based reduced order model for multiscale analysis of heterogeneous hyperelastic materials[J]. *Journal of Computational Physics*, 2016, 313: 635-653.
28. Wang Y, Cheung S W, Chung E T, et al. Deep multiscale model learning[J]. *Journal of Computational Physics*, 2020, 406: 109071.
29. Fish J, Yuan Z, Kumar R. Computational certification under limited experiments[J]. *International Journal for Numerical Methods in Engineering*, 2018, 114(2): 172-195.
30. Fish J, Shek K, Pandheeradi M, et al. Computational plasticity for composite structures based on mathematical homogenization: Theory and practice[J]. *Computer methods in applied mechanics and engineering*, 1997, 148(1-2): 53-73.
31. Oskay C, Fish J. Eigendeformation-based reduced order homogenization for failure analysis of heterogeneous materials[J]. *Computer Methods in Applied Mechanics and Engineering*, 2007, 196(7): 1216-1243.
32. Yuan Z, Fish J. Multiple scale eigendeformation-based reduced order homogenization[J]. *Computer Methods in Applied Mechanics and Engineering*, 2009, 198(21-26): 2016-2038.
33. Yuan Z, Fish J. Hierarchical model reduction at multiple scales[J]. *International journal for numerical methods in engineering*, 2009, 79(3): 314-339.
34. Fish J. *Practical multiscale modeling*[M]. John Wiley & Sons, 2013.
35. Yuan Z, Aitharaju V, Fish J. A coupled thermo-chemo-mechanical reduced-order multiscale model for predicting process-induced distortions, residual stresses, and strength[J]. *International Journal for Numerical Methods in Engineering*, 2020, 121(7): 1440-1455.
36. Michel J C, Suquet P. Nonuniform transformation field analysis[J]. *International journal of solids and structures*, 2003, 40(25): 6937-6955.
37. Michel J C, Suquet P. Computational analysis of nonlinear composite structures using the nonuniform transformation field analysis[J]. *Computer methods in applied mechanics and engineering*, 2004, 193(48-51): 5477-5502.
38. Matouš K, Geers M G D, Kouznetsova V G, et al. A review of predictive nonlinear theories for multiscale modeling of heterogeneous materials[J]. *Journal of Computational Physics*, 2017, 330: 192-220.
39. Fish J, Wagner G J, Keten S. Mesoscopic and multiscale modelling in materials[J]. *Nature materials*, 2021, 20(6): 774-786.

40. Schlick T, Portillo-Ledesma S, Myers C G, et al. Biomolecular modeling and simulation: a prospering multidisciplinary field[J]. Annual review of biophysics, 2021, 50: 267-301.
41. Schlick T, Portillo-Ledesma S, Blaszczyk M, et al. A MULTISCALE VISION–ILLUSTRATIVE APPLICATIONS FROM BIOLOGY TO ENGINEERING[J]. International journal for multiscale computational engineering, 2021, 19(2).
42. Bi J, Hanke F, Ji H, et al. Multiscale modeling for the science and engineering of materials[J]. International Journal for Multiscale Computational Engineering, 2021, 19(3).
43. Doghri I, Lemoine G, Martiny P, et al. Multiscaling-based integrated computational materials engineering: from academia to industry[J]. International Journal for Multiscale Computational Engineering, 2021, 19(4).
44. Wollschlager J, Yuan Z, McAuliffe C, et al. A Technical Overview of Altair Multiscale Designer[J]. International Journal for Multiscale Computational Engineering, 2021, 19(4).
45. Song N, Jackson M, Montgomery C, et al. Using Multiscale Modeling to Advance Industrial and Research Applications of Advanced Materials[J]. International Journal for Multiscale Computational Engineering, 2021, 19(4).
46. Pineda E J, Bednarczyk B A, Ricks T M, et al. Efficient multiscale recursive micromechanics of composites for engineering applications[J]. International Journal for Multiscale Computational Engineering, 2021, 19(4).
47. Rokoš O, Zeman J, Doškář M, et al. Reduced integration schemes in micromorphic computational homogenization of elastomeric mechanical metamaterials[J]. Advanced Modeling and Simulation in Engineering Sciences, 2020, 7: 1-17.
48. Belytschko T, Ong J S J, Liu W K, et al. Hourglass control in linear and nonlinear problems[J]. Computer Methods in Applied Mechanics and Engineering, 1984, 43(3): 251-276.
49. Liu W K, Ong J S J, Uras R A. Finite element stabilization matrices-a unification approach[J]. Computer Methods in Applied Mechanics and Engineering, 1985, 53(1): 13-46.
50. Fish J, Belytschko T. A first course in finite elements[M]. New York: Wiley, 2007.
51. Miehe C. Numerical computation of algorithmic (consistent) tangent moduli in large-strain computational inelasticity[J]. Computer methods in applied mechanics and engineering, 1996, 134(3-4): 223-240.
52. Kouznetsova V G. Computational homogenization for the multi-scale analysis of multi-phase materials[J]. 2004.

53. Dalcin L, Mortensen M, Keyes D E. Fast parallel multidimensional FFT using advanced MPI[J]. *Journal of Parallel and Distributed Computing*, 2019, 128: 137-150.
54. Zhu Q, Geubelle P H, Li M, et al. Dimensional accuracy of thermoset composites: simulation of process-induced residual stresses[J]. *Journal of composite materials*, 2001, 35(24): 2171-2205.
55. Cheung A, Yu Y, Pochiraju K. Three-dimensional finite element simulation of curing of polymer composites[J]. *Finite Elements in Analysis and Design*, 2004, 40(8): 895-912.
56. Prulière E, Férec J, Chinesta F, et al. An efficient reduced simulation of residual stresses in composite forming processes[J]. *International Journal of Material Forming*, 2010, 3(Suppl 2): 1339-1350.
57. Yuan Z, Aitharaju V, Fish J. A coupled thermo-chemo-mechanical reduced-order multiscale model for predicting process-induced distortions, residual stresses, and strength[J]. *International Journal for Numerical Methods in Engineering*, 2020, 121(7): 1440-1455.
58. Yuan Z, Felder S, Reese S, et al. A coupled thermo-chemo-mechanical reduced-order multiscale model for predicting residual stresses in fibre reinforced semi-crystalline polymer composites[J]. *International Journal for Multiscale Computational Engineering*, 2020, 18(5).
59. Bessa M A, Bostanabad R, Liu Z, et al. A framework for data-driven analysis of materials under uncertainty: Countering the curse of dimensionality[J]. *Computer Methods in Applied Mechanics and Engineering*, 2017, 320: 633-667.
60. Bhattacharjee S, Matouš K. A nonlinear manifold-based reduced order model for multiscale analysis of heterogeneous hyperelastic materials[J]. *Journal of Computational Physics*, 2016, 313: 635-653.
61. Wang Y, Cheung S W, Chung E T, et al. Deep multiscale model learning[J]. *Journal of Computational Physics*, 2020, 406: 109071.
62. Wu L, Zulueta K, Major Z, et al. Bayesian inference of non-linear multiscale model parameters accelerated by a deep neural network[J]. *Computer Methods in Applied Mechanics and Engineering*, 2020, 360: 112693.
63. Gorji M B, Mozaffar M, Heidenreich J N, et al. On the potential of recurrent neural networks for modeling path dependent plasticity[J]. *Journal of the Mechanics and Physics of Solids*, 2020, 143: 103972.
64. Unger J F, Könke C. Neural networks as material models within a multiscale approach[J]. *Computers & structures*, 2009, 87(19-20): 1177-1186.
65. Unger J F, Könke C. Coupling of scales in a multiscale simulation using neural networks[J]. *Computers & Structures*, 2008, 86(21-22): 1994-2003.

66. Mozaffar M, Bostanabad R, Chen W, et al. Deep learning predicts path-dependent plasticity[J]. *Proceedings of the National Academy of Sciences*, 2019, 116(52): 26414-26420.
67. Cho K, Van Merriënboer B, Gulcehre C, et al. Learning phrase representations using RNN encoder-decoder for statistical machine translation[J]. *arXiv preprint arXiv:1406.1078*, 2014.
68. Z. Liu, M.A. Bessa, W.K. Liu, "Self-consistent clustering analysis: an efficient multi-scale scheme for inelastic heterogeneous materials," *Computer Methods in Applied Mechanics and Engineering*, vol. 306, pp. 319-341, 2016.
69. Wang K, Sun W C. A multiscale multi-permeability poroplasticity model linked by recursive homogenizations and deep learning[J]. *Computer Methods in Applied Mechanics and Engineering*, 2018, 334: 337-380.
70. J. Ghaboussi, J.H. Garret Jr., X. Wu, "Knowledge-based modeling of material behavior with neural networks," *Journal of engineering mechanics*, vol. 117(1), pp. 132-153, 1991.
71. Karapiperis K, Stainier L, Ortiz M, et al. Data-driven multiscale modeling in mechanics[J]. *Journal of the Mechanics and Physics of Solids*, 2021, 147: 104239.
72. Fish J, Yu Y. A Pseudo-Nonlocal Finite Element for Efficient Solution of Computationally Demanding Material Models[J]. *International Journal for Multiscale Computational Engineering*, 2021, 19(2).
73. Simo J C, Hughes T J R. *Computational inelasticity*[M]. Springer Science & Business Media, 2006.
74. Rappel H, Beex LA, Hale JS, Noels L, Bordas SP. A tutorial on Bayesian inference to identify material parameters in solid mechanics. *Archives of Computational Methods in Engineering*. 2020 Apr;27:361-85.
75. Most T. Identification of the parameters of complex constitutive models: Least squares minimization vs. Bayesian updating. *Reliability and optimization of structural systems*. 2010 Jul 28;119.
76. Rappel H, Beex LA, Noels L, Bordas SP. Identifying elastoplastic parameters with Bayes' theorem considering output error, input error and model uncertainty. *Probabilistic Engineering Mechanics*. 2019 Jan 1;55:28-41.
77. As'ad F, Avery P, Farhat C. A mechanics-informed artificial neural network approach in data-driven constitutive modeling. *International Journal for Numerical Methods in Engineering*. 2022 Jun 30;123(12):2738-59.
78. Zohdi TI. A note on rapid genetic calibration of artificial neural networks. *Computational Mechanics*. 2022 Oct;70(4):819-27.

79. G. J. Dvorak. *Micromechanics of Composite Materials*, ISBN: 978-94-007-4101-0, 2013.
80. He C, Ge J, Qi D, Gao J, Chen Y, Liang J, Fang D. A multiscale elasto-plastic damage model for the nonlinear behavior of 3D braided composites. *Composites Science and Technology*. 2019 Feb 8;171:21-33.
81. Liu Y, Filonova V, Hu N, Yuan Z, Fish J, Yuan Z, Belytschko T. A regularized phenomenological multiscale damage model. *International Journal for Numerical Methods in Engineering*. 2014 Sep;99(12):867-87.
82. Fish J, Yu Q. Multiscale damage modelling for composite materials: theory and computational framework. *International Journal for Numerical Methods in Engineering*. 2001 Sep 10;52(1-2):161-91.
83. Kanouté P, Boso DP, Chaboche JL, Schrefler B. Multiscale methods for composites: a review. *Archives of Computational Methods in Engineering*. 2009 Mar;16:31-75.
84. Fish J, Yu Y. Data-physics driven reduced order homogenization. *International Journal for Numerical Methods in Engineering*. 2023 Apr 15;124(7):1620-45.
85. Bazant ZP, Belytschko TB, Chang TP. Continuum theory for strain-softening. *Journal of Engineering Mechanics*. 1984 Dec;110(12):1666-92.
86. Bažant ZP. Nonlocal damage theory based on micromechanics of crack interactions. *Journal of engineering mechanics*. 1994 Mar;120(3):593-617.
87. Jirásek M, Bažant ZP. Localization analysis of nonlocal model based on crack interactions. *Journal of engineering mechanics*. 1994 Jul;120(7):1521-42.
88. Peerlings RH, de Borst R, Brekelmans WM, de Vree J. Gradient enhanced damage for quasi-brittle materials. *International Journal for numerical methods in engineering*. 1996 Oct 15;39(19):3391-403.
89. Yin B, Zreid I, Lin G, Bhashyam G, Kaliske M. An anisotropic damage formulation for composite materials based on a gradient-enhanced approach: Formulation and implementation at small strain. *International Journal of Solids and Structures*. 2020 Oct 1;202:631-45.
90. Geers MG, Brekelmans WA, De Borst R. Viscous regularization of strain-localisation for damaging materials: viscous and rate-dependent constitutive models. In *DIANA Computational Mechanics '94: Proceedings of the First International Diana Conference on Computational Mechanics 1994* (pp. 127-138). Springer Netherlands.
91. Ambati M, Gerasimov T, De Lorenzis L. A review on phase-field models of brittle fracture and a new fast hybrid formulation. *Computational Mechanics*. 2015 Feb;55:383-405.

92. Vaz Jr M, Owen DR. Aspects of ductile fracture and adaptive mesh refinement in damaged elasto-plastic materials. *International Journal for Numerical Methods in Engineering*. 2001 Jan 10;50(1):29-54.
93. Bazant ZP. Can multiscale-multiphysics methods predict softening damage and structural failure?. *International Journal for Multiscale Computational Engineering*. 2010;8(1).
94. Dvorak GJ. Transformation field analysis of inelastic composite materials. *Proceedings of the Royal Society of London. Series A: Mathematical and Physical Sciences*. 1992 May 8;437(1900):311-27.
95. Wu L, Noels L, Adam L, Doghri I. A multiscale mean-field homogenization method for fiber-reinforced composites with gradient-enhanced damage models. *Computer Methods in Applied Mechanics and Engineering*. 2012 Aug 1;233:164-79.
96. Kwon YW, Allen DH, Talreja R. *Multiscale modeling and simulation of composite materials and structures*. New York: Springer; 2008.
97. Ghosh S, Bai J, Paquet D. Homogenization-based continuum plasticity-damage model for ductile failure of materials containing heterogeneities. *Journal of the Mechanics and Physics of Solids*. 2009 Jul 1;57(7):1017-44.
98. Jain JR, Ghosh S. Damage evolution in composites with a homogenization-based continuum damage mechanics model. *International Journal of Damage Mechanics*. 2009 Aug;18(6):533-68.
99. Tekog C, Pardo T. A micromechanics based damage model for composite materials. *International Journal of plasticity*. 2010 Apr 1;26(4):549-69.
100. Khoei AR, Saadat MA. A nonlocal computational homogenization of softening quasi-brittle materials. *International Journal for Numerical Methods in Engineering*. 2019 Aug 24;119(8):712-36.
101. Deng S. Deep Learning for Multiscale Damage Analysis via Physics-Informed Recurrent Neural Network. *arXiv preprint arXiv:2212.01880*. 2022 Dec 4.
102. Unger JF, Könke C. Coupling of scales in a multiscale simulation using neural networks. *Computers & Structures*. 2008 Nov 1;86(21-22):1994-2003.
103. Geers MG, Kouznetsova VG, Brekelmans WA. Multiscale first-order and second-order computational homogenization of microstructures towards continua. *International Journal for Multiscale Computational Engineering*. 2003;1(4).
104. Petracca M, Pelà L, Rossi R, Oller S, Camata G, Spacone E. Regularization of first order computational homogenization for multiscale analysis of masonry structures. *Computational mechanics*. 2016 Feb;57:257-76.

105. Fish J, Jiang T, Yuan Z. A staggered nonlocal multiscale model for a heterogeneous medium. *International journal for numerical methods in engineering*. 2012 Jul 13;91(2):142-57.
106. Mazars J, Pijaudier-Cabot G. Continuum damage theory—application to concrete. *Journal of engineering mechanics*. 1989 Feb;115(2):345-65.
107. De Vree JH, Brekelmans WA, van Gils M. Comparison of nonlocal approaches in continuum damage mechanics. *Computers & Structures*. 1995 May 17;55(4):581-8.
108. Chen Y, Mobasher ME, You T, Waisman H. Non-local continuum damage model for poro-viscoelastic porous media. *International Journal of Rock Mechanics and Mining Sciences*. 2022 Nov 1;159:105212.
109. Logarzo HJ, Capuano G, Rimoli JJ. Smart constitutive laws: Inelastic homogenization through machine learning. *Computer methods in applied mechanics and engineering*. 2021 Jan 1;373:113482.
110. Ketkar N, Ketkar N. Introduction to keras. *Deep learning with python: a hands-on introduction*. 2017:97-111.

Appendix A Components of the data-driven surrogate-based Bayesian Inverse modeling

A.1 Bayesian Inference

The Bayesian inference approach [75-77], is based on the Bayes' theorem which states that the posterior distribution of a random parameter vector $\boldsymbol{\theta}$ for given observations \mathbf{y}^{obs} , denoted as $\pi(\boldsymbol{\theta} | \mathbf{y}^{obs})$ is proportional to the prior distribution $\pi(\boldsymbol{\theta})$ multiplied by the likelihood function of observations (the PDF of the observed \mathbf{y}), $\pi(\mathbf{y}^{obs} | \boldsymbol{\theta})$. $\pi(\bullet | \bullet)$ denotes the conditional probability density function (PDF). The Bayes' theorem can be expressed as:

$$\pi(\boldsymbol{\theta} | \mathbf{y}^{obs}) = \frac{\pi(\boldsymbol{\theta})\pi(\mathbf{y}^{obs} | \boldsymbol{\theta})}{\pi(\mathbf{y}^{obs})} \quad (\text{A.1})$$

In the present study, \mathbf{y}^{obs} denotes the coarse-scale stress tensor; $\boldsymbol{\theta} = \{\theta^{ETT}, \theta^{MCM}\}$ the eigenstrain transformation tensor rescaling parameters and the microstructural constitutive parameters.

Using the law of total probabilities, $\pi(\mathbf{y}^{obs})$ and $\pi(\boldsymbol{\theta})$ can be related to the conditional probability $\pi(\mathbf{y}^{obs} | \boldsymbol{\theta})$ in eq. (A.1) as:

$$\pi(\mathbf{y}^{obs}) = \int_{\boldsymbol{\theta}} \pi(\boldsymbol{\theta})\pi(\mathbf{y}^{obs} | \boldsymbol{\theta})d\boldsymbol{\theta} \quad (\text{A.2})$$

which can be regarded as a normalization factor that ensures the integral of the posterior distribution $\pi(\mathbf{y}^{obs} | \boldsymbol{\theta})$ over $\boldsymbol{\theta}$ equals 1. Consequently, eq. (A.1) can be written as:

$$\pi(\boldsymbol{\theta} | \mathbf{y}^{obs}) \propto \pi(\boldsymbol{\theta})\pi(\mathbf{y}^{obs} | \boldsymbol{\theta}) \quad (\text{A.3})$$

The prior distribution $\pi(\boldsymbol{\theta})$ represents our belief of interested parameters. The contribution of the prior distribution to the posterior distribution decreases if the observed data increases. For N independent parameters, the prior distribution is given as:

$$\pi(\boldsymbol{\theta}) = \pi(\theta^1) \times \pi(\theta^2) \times \pi(\theta^3) \cdots \times \pi(\theta^N) \quad (\text{A.4})$$

In absence of experimental data the prior distribution can be assumed to be uniform.

To construct the likelihood function, we need to select the noise model to represent the difference between measured data, \mathbf{y}^{obs} , and the numerical model response, $\mathbf{f}(\mathbf{x}, \boldsymbol{\theta})$. The additive noise model can be expressed as

$$\mathbf{y}^{obs} = \mathbf{f}(\mathbf{x}, \boldsymbol{\theta}) + \boldsymbol{\Omega} \quad (\text{A.5})$$

Herein, $\boldsymbol{\Omega}$ denotes the noise vector. Assuming $\mathbf{f}(\mathbf{x}, \boldsymbol{\theta})$ and $\boldsymbol{\Omega}$ are mutually independent, the probability density of \mathbf{y}^{obs} for a given $\boldsymbol{\theta}$ is obtained by shifting the density of $\boldsymbol{\Omega}$ around $\mathbf{f}(\mathbf{x}, \boldsymbol{\theta})$.

Consequently, the likelihood function can be expressed as:

$$\pi(\mathbf{y}^{obs} | \boldsymbol{\theta}) = \pi_{\text{noise}}(\mathbf{y}^{obs} - \mathbf{f}(\mathbf{x}, \boldsymbol{\theta})) \quad (\text{A.6})$$

where $\pi_{\text{noise}}()$ denotes PDF noise. In the present study the observed data is multidimensional. We adopt multivariate normal distribution as the noise model. The structure of the likelihood function for a single sample is given as

$$\pi_{\text{noise}}(\mathbf{y}^{obs} - \mathbf{f}(\mathbf{x}, \boldsymbol{\theta})) = \frac{\exp(-\frac{1}{2}(\mathbf{y}^{obs} - \mathbf{f}(\mathbf{x}, \boldsymbol{\theta}))^T \boldsymbol{\Sigma}(\mathbf{y}^{obs} - \mathbf{f}(\mathbf{x}, \boldsymbol{\theta})))}{\sqrt{(2\pi)^k |\boldsymbol{\Sigma}|}} \quad (\text{A.7})$$

where $\boldsymbol{\Sigma}$ denotes the covariance matrix which can be computed from the observed data; k is the vector dimension; and $|\boldsymbol{\Sigma}|$ the determinant of the covariance matrix. The probability density function $\pi(\mathbf{y}^{obs} | \boldsymbol{\theta})$ provides the probability of the forward numerical simulation \mathbf{f} for certain model parameters $\boldsymbol{\theta}$. If the results of numerical model are far from observed data \mathbf{y}^{obs} , $\pi(\mathbf{y}^{obs} | \boldsymbol{\theta})$

will return a small probability, which means that the numerical model for the above model parameters is unlikely to occur.

For a high-dimensional parameter space it is challenging to analytically evaluate the integral in eq. (A.2). Therefore, Markov chain Monte Carlo (MCMC) is employed to evaluate the posterior by drawing samples from the posterior distribution. Consequently, based on these sample one can obtain statistical information, such as the expected value of the target distribution, without directly computing the posterior. Among the different MCMC algorithms, Metropolis-Hastings (MH) is very effective in the context of the "black box" model. The pseudocode of Metropolis-Hastings algorithm is given below.

Algorithm 1 Metropolis algorithm pseudocode

```

1: Assume a function  $f(x)$  proportional to the desired probability density function (A2)
2: Initialization: Generating a random sample points  $\theta_t$  and a conditional probability density function  $g(\theta_{t+1}|\theta_t)$  that provides the next candidate  $\theta_t$  given the current sample point  $\theta_t$ . Usually, gaussian distribution is a good choice for  $g(\theta_{t+1}|\theta_t)$ .
3: for each iteration do
4:   Generate the next candidate  $\theta'$  using  $g(\theta'|\theta_t)$ 
5:   Calculate the acceptance ratio  $\alpha = \frac{f(\theta_{t+1})}{f(\theta_t)}$ 
6:   Generate a random number  $u \in [0, 1]$ 
7:   if  $u \leq \alpha$  then
8:     accept the candidate  $\theta_{t+1} = \theta'$ 
9:   else if  $u > \alpha$  then
10:    reject the candidate  $\theta_{t+1} = \theta_t$ 
11:   end if
12: end for

```

Figure A.1: Metropolis-Hastings algorithm pseudocode

This algorithm will explore the sample space randomly with some rules. If α is larger than 1, we will always accept this sample. While it is smaller than 1, we may or may not accept it. Finally, the algorithm returns more samples in the high-density region of $f(x)$. Since $f(x)$ is proportional to our desired probability density function (A.2), the posterior distribution (A.2) is solved by MCMC.

A.2 The Gated Recurrent Unit (GRU) based surrogate model

A neural network (NN) is a network constructed by artificial neurons. Each neuron weights and operates on the input with bias terms. The result is passed to an activation function. The activation function can be considered as adding nonlinearity to the NN. The network consisting of multiple layers together with an appropriate activation function maps from an input to an output provided sufficient training process. A loss function is usually defined as the difference between the predicted and given outputs. In the present study, the loss function is defined as the mean squared error

$$\text{MSE} = \frac{1}{n} \sum_{i=1}^n (\mathbf{Y}_i^{\text{pred}} - \mathbf{Y}_i^{\text{true}})^2 \quad (\text{A.8})$$

where n is the number of samples; \mathbf{Y}^{pred} the predicted output; and \mathbf{Y}^{true} the true output. Note that the \mathbf{Y}^{pred} and \mathbf{Y}^{true} are normalized values through "MinMaxScale". The transformation is given by:

$$\mathbf{Y}_{\text{std}} = \frac{\mathbf{Y} - \mathbf{Y}_{\min}}{\mathbf{Y}_{\max} - \mathbf{Y}_{\min}} \quad (\text{A.9})$$

$$\mathbf{Y}_{\text{scaled}} = \mathbf{Y}_{\text{std}} (\text{max-min}) + \text{min} \quad (\text{A.10})$$

where \mathbf{Y} is the feature; \mathbf{Y}_{\min} and \mathbf{Y}_{\max} define the minimum and maximum values of the feature \mathbf{Y} . "max" and "min" are the bounds of the desired range. In the present study, we rescale all the features to the range of (0,1). The training process of the neural network consists of updating the weights of the model in attempt to reduce the loss function. A smaller value of the loss function means that the trained model performs better on the training and validation data. The purpose of the validation set is to provide an unbiased evaluation of a model fit to the training dataset while tuning model hyperparameters. A typical network structure is depicted in Figure A.2.

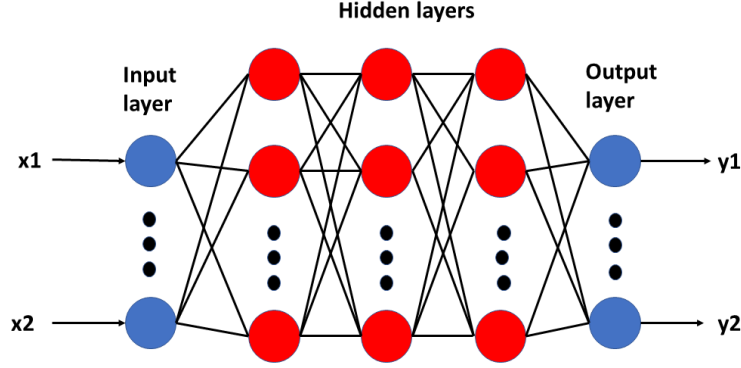


Figure A.2: Schematics of the fully connected neural network architecture

where x denotes the input; y the output; and each circle represents the neuron. The depth (number of hidden layers) of each neural network depends on the complexity of the data set. This type of neural network is called a fully connected neural network (FCNN). FCNN is appropriate for modeling the constitutive laws of elastic and hyper-elastic materials.

For the path-dependent models, such as plasticity or damage, where the output depends on the history of the input, so-called recurrent neural networks (RNN) are usually employed. Among the various RNNs, Gated Recurrent Units (GRUs) is known as a type of RNN capable of solving the vanishing gradient problem. Compared with the FCNN, GRUs have a special unit called gated unit. This unit can determine how much information from the past can be forgotten or be passed to the future. The classical GRU architecture is shown in the Figure A.2. There are four special units in the GRU. The first one is called update gate expressed as

$$\mathbf{z}_t = \sigma(\mathbf{W}^z \mathbf{x}_t + \mathbf{U}^z \mathbf{h}_{t-1}) \quad (\text{A.11})$$

It multiplies the input \mathbf{x} at time t by its weight \mathbf{W}^z while taking the weighted information $\mathbf{U}^z \mathbf{h}_{t-1}$ into account from the previous time step, $t-1$. Their sum is passed to the sigmoid activation function, where $\sigma(x) = \frac{1}{1 + \exp(-x)}$ scales the result to the range $[-1,1]$.

The reset gate \mathbf{r}_t , which determines how much of the past information can be forgotten, is defined as.

$$\mathbf{r}_t = \sigma(\mathbf{W}^r x_t + \mathbf{U}^r \mathbf{h}_{t-1}) \quad (\text{A.12})$$

With the above two special gates, two memory units can be computed. One is for the current unit, the other for the network defined as

$$\mathbf{h}'_t = \tanh(\mathbf{W} \mathbf{x}_t + \mathbf{r}_t \odot \mathbf{h}_{t-1}) \quad (\text{A.13})$$

$$\mathbf{h}_t = \mathbf{z}_t \odot \mathbf{h}_{t-1} + (1 - \mathbf{z}_t) \odot \mathbf{h}'_t \quad (\text{A.14})$$

“tanh” denotes the hyperbolic tangent which also scales information to the range $[-1,1]$. “ \odot ” denotes the Hadamard (element-wise) product. The neuron in the gated recurrent unit network is illustrated in Figure A.3.

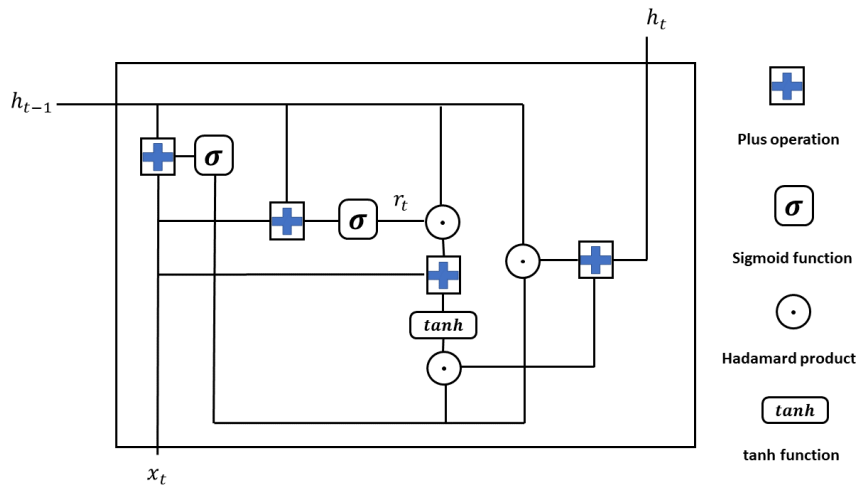


Figure A.3: Gated recurrent unit neuron definition

The loss function definition and the training process are similar to the FCNN. In our case, all GRU neural networks have two hidden layers of 64 neurons. the activation function of the GRU layers is a "relu" function, while the activation function of the final dense layer is linear. The training strategy will use the classical gradient-based method: stochastic gradient descent (SGD). The batch size is 128 and the training epochs is 250. we also recommend the faster training strategy Genetic Algorithm, which is more effective when the loss function is non-smooth and non-differentiable.